UNIVERSITY OF PÉCS

Doctoral School of Physics

Laser Physics, Nonlinear Optics, and Spectroscopy Program

Development of Extremely Strong Longitudinal Electric Field by Focusing of Radially Polarized THz Pulses

PhD Thesis

Zerihun Tadele Godana

Supervisor:

Prof. Dr. László Pálfalvi

University of Pécs

PÉCS, 2024

Dedication

This thesis is dedicated to the memory of my beloved and respected late mother, Werkaferahu Gessesse.

Abstract

The thesis discusses the issue of focusing a radially polarized laser beam with a parabolic mirror (or parabola-ring) with special attention to beams and pulses in the THz frequency range. The main goal of the thesis is to find an optimal focusing geometry that provides an extremely strong longitudinal electric field for particle acceleration applications. When using laser and THz pulses for particle acceleration, it is crucial to know accurately the characteristics of the electromagnetic fields of the focused beam/pulse, especially around the focus. The thesis uses the Stratton-Chu vector diffraction method to precisely determine the distribution of electromagnetic field strength under various focusing conditions. Analytical derivations were performed for different input beam profiles, including flat-top and Gaussian vector beams with (homogeneous transversal intensity distribution), not only for "simply connected" paraboloid mirror surfaces but also for paraboloid-ring cases, which, when complemented with an axicon pair, practically allow for the (post)acceleration of charged particles. Detailed analyses showed the dominance of the longitudinal electric field, which is remarkable from the perspective of particle acceleration. The thesis examined in detail the distribution of the longitudinal component of the electric field of the radially polarized, monochromatic Gaussian vector beam at the focus of the parabolic mirror. In addition to that, it investigated how beam divergence affects the longitudinal and radial distribution of the longitudinal electric field. The results showed that beam divergence shifts the focus and has a significant impact on the maximum achievable longitudinal electric field. The thesis concludes that the physical shift of the focus compared to the geometrical focus linearly depends on the divergence along the longitudinal direction. With optimized focusing, the ratio of the longitudinal electric field strength developed at the focus to the incoming radial electric field component exceeds 1000. The calculations also predicted that by optimizing the focusing of radially polarized THz pulses, the electric field component can reach magnitudes of 100 MV/cm, which is excellently suitable for particle acceleration. Numerical simulation results establish the possibility of subsequent acceleration of relativistic electrons using the focused longitudinal electric field of THz pulses. According to the simulations, assuming a 3 mJ THz pulse energy, a 1 ps pulse duration, and a 50 mm focal length of parabolic ring illuminated at 20° and 40°, electrons moving at nearly the speed of light could gain energy by 0.23/0.28 MeV (20°) and 0.36 MeV/0.63 MeV (40°) depending on whether their direction of motion is the same as/opposite to the direction of the electric field sweeping speed.

Table of Contents

List of Figures

List of Table

List of Abbreviations and Acronyms

2PA	Two-Photon Absorption
3PA	Three-Photon Absorption
AR	Antireflective
CG	Contact Grating
CM	Converging Conical Mirror
DM	Diverging Conical Mirror
fs	femtosecond
FWHM	Full Width at Half Maximum
NA	Numerical Aperture
NLES	Nonlinear Echelon Slab
NM	Nonlinear Material
OAP	Off-Axis Parabolic
OR	Optical Rectification
ps	picosecond
RES	Stair-Step Reflective Echelon
RNLS	Reflective Nonlinear Slab
SHWP	Segmented Half-Wave Plate
SNM	Segmented Nonlinear Material
STEAM	Segmented Terahertz Electron Accelerator and Manipulator
THz	Terahertz
TPF	Tilted-Pulse-Front
TPFP	Tilted-Pulse-Front Pumping
VPHG	Volume Phase Holographic Grating
$LiNbO_3$, LN	Lithium Niobate
$LiTaO_3$	Lithium Tantalate
cLN	Congruent Lithium Niobate
sLN	Stoichiometric Lithium Niobate
MgO:sLN	Stoichiometric Magnesium Oxide -doped Lithium Niobate
Cr:fosterite ($Cr:Mg_2SiO_4$)	Chromium-doped Forsterite
CdTe	Cadmium Telluride
GaAs	Gallium Arsenide
GaP	Gallium Phosphide
GaSe	Gallium Selenide

InP   Indium Phosphate

ZnSe   Zinc Selenide

ZnTe   Zinc Telluride

DAST   4-dimethylamino-N -methyl-4-stilbazolium tosylate

DSTMS   4-N, N-dimethylamino-4′-N′-methyl-stilbazolium 2,4,6-
trimethylbenzenesulfonate

OH1   2-[3-(4- hydroxystyryl)-5, 5-dimethylcyclohex-2-enylidene] malononitrile

HQM-TMS   2-(4-hydroxy-3-methoxystyryl)-1-methylquinolinium
2,4,6trimethylbenzenesulfonate)

BNA   N-benzyl-2-methyl-4-nitroaniline

1. Introduction

1.1. Outline of the Thesis

The thesis is structured into ten chapters. Chapter 1 provides background information on the study. Chapter 2 introduces a theoretical framework relevant to the thesis, explaining electromagnetic diffraction theory, including the Rayleigh−Sommerfeld scalar diffraction theory and the Stratton−Chu vector diffraction theory. It also covers the vector Gaussian beam with linear and radial polarization, which is important for understanding light behavior in optical systems. Chapter 3 outlines the scientific goals of the study. The content of Chapters 4, 5, and 6 in this thesis focuses on presenting *my original scientific results*. Chapter 4 focuses on the derivation of the electric field produced when a radially polarized, monochromatic, flat-top beam is focused by a parabolic mirror, utilizing the Stratton−Chu integral. It provides a detailed theoretical analysis of the electric field distribution, particularly the longitudinal and radial components, which is important for understanding particle acceleration applications. Chapter 5 extends the discussion by deriving general formulas that describe the electric and magnetic field characteristics of a focused, radially polarized Gaussian vector beam by a parabolic mirror with an arbitrary numerical aperture. Using the Stratton–Chu vector diffraction method, the chapter analyzes the field characteristics in the focal area, focusing specifically on the axial and radial distributions of the longitudinal electric field component for different incident beam divergences, which is significant for particle acceleration applications.

Chapter 6 discusses the generation of extremely strong accelerating electric fields. This is achieved by focusing radially polarized THz pulses with a parabolic mirror ring, which is suitable for vacuum electron acceleration. The chapter introduces a novel setup that includes a reflaxicon, a ring-like segment of an on-axis parabolic mirror, a segmented waveplate, and a segmented nonlinear material. It highlights the importance of focusing geometry and beam parameters in achieving the high field intensities necessary for effective particle acceleration. Chapter 7 presents the comparison of the efficiency of three-focusing geometry (Chapters 4, 5, and 6), based on field enhancement factors. Chapter 8 presents the general conclusions and future perspectives of the thesis. Chapter 9 contains

the thesis statements. Finally, a summary of the thesis in Hungarian is provided in Chapter 10.

1.2. Terahertz Radiation

Terahertz (THz) radiation has a frequency between 0.1 and 10 THz, which is in the electromagnetic spectrum between microwaves and infrared radiation. It has some characteristics in common with both of these regions (see Fig. 1.1). In the electromagnetic spectrum, radiation at 1 THz $= 10^{12}$ Hz has a period of 1 ps, a wavelength of 300 µm, a wave number of 33.3 cm^{-1}, an angular frequency of 6.28 THz, a photon energy of 4.14 meV, and an equivalent temperature of 48 K [1]. The technical establishment of THz wave generation and detection is comparatively less developed than in other frequency regions. In high-frequency electronics, the frequency of the THz wave is extremely high to be effectively managed using traditional semiconductor technology. In optics/photonics, the THz wave photon energy is much lower than visible and near-infrared light. Consequently, it is challenging to control and manipulate THz waves using current electronics and optics/photonics technologies. This difficulty is commonly known as the "THz gap." Nevertheless, with the introduction of ultrafast lasers in the late 1980s, researchers have gained access to the THz spectral region, resulting in a significant increase in investigations conducted at THz frequencies [2].
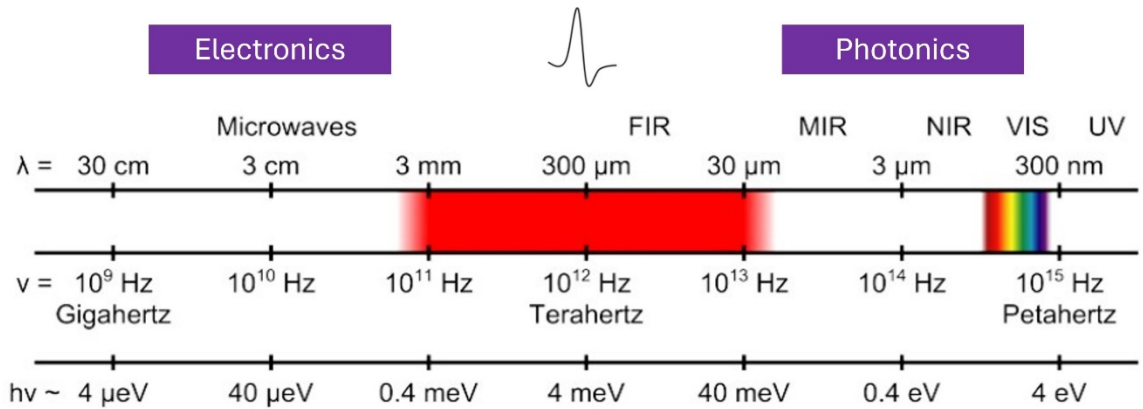
Figure 1.1. THz band in the electromagnetic spectrum.

In the early 1990s, femtosecond lasers were developed. Since then, the THz frequency is considered a crucial field of scientific research. The technology and performance of THz

sources, detectors, modulators, and other related components are experiencing significant growth, which is facilitating the progress of THz devices and applications. Recently, the THz electromagnetic band has been used for a variety of applications like biological imaging [3], nondestructive testing [4], security screening [5], process control [6], and even the next generation of wireless communication systems [7]. The main limitation in the field of THz science and technology, after its steady development in the past few decades, is the availability of high-power THz sources. The main interest of current investigations in this discipline is the development of high-powered pulsed THz generation for various applications. High-intensity lasers with short pulse durations that come into contact with a target produce strong and broadband THz pulses. Several methods for generating THz radiation sources exist, such as free-electron lasers which have restricted availability [8, 9], quantum-cascade lasers which have low peak fields [10, 11], photoconductive antennas [12-14], laser-induced plasma radiation [15-18], spintronic emitters [19-21] and optical rectification [22-24]. Optical rectification (OR) is one of the most well-known second-order nonlinear techniques to generate highly intense single- and few-cycle THz pulses using femtosecond laser pulses. The need for intense single-cycle THz pulses reaching energy levels in the millijoules scale and peak THz electric fields exceeding 10 MV/cm is significant in particle acceleration applications [25]. Among the various methods available OR has proven to be highly efficient in providing single-cycle THz pulses characterized by remarkably high energies and electric fields. The promising nonlinear crystals to generate single- and few-cycle THz pulses by the OR process are ferroelectric crystals like lithium niobate ($LiNbO_3$, LN) and lithium tantalate ($LiTaO_3$), organic crystals like DAST, DSTMS, OH1, etc., and inorganic semiconductor crystals like CdTe, GaSe, GaAs, ZnTe, GaP, etc [26].

1.3. THz Sources Development Via Optical Rectification

The generation of THz radiation by OR is only possible by pulsed laser beams. When a pulsed laser beam propagates through the nonlinear crystal, and then induced polarization inside the nonlinear crystal gives rise to the THz electric field (see Fig. 1.2). The induced second-order nonlinear electric polarization is related with the optical field by:

$$P_{NL}^{(2)}(\Omega) = \varepsilon_o \int_{\omega-\Delta\omega}^{\omega+\Delta\omega} \chi^{(2)}(\Omega:\omega+\Delta\omega,-\omega)E(\omega+\Delta\omega)E^*(\omega)d\omega \qquad (1.1)$$

where ε_o is vacuum permittivity, ω is the frequency of the incident pulsed light beam, Ω is the THz frequency and $\Delta\omega$ is the bandwidth of the incident pulsed light beam, $\Delta\omega \geq 1/\tau \approx 10^{12}$ Hz when the incident pulse duration is in picosecond range. $E(\omega+\Delta\omega)$ and $E^*(\omega)$ are the Fourier transforms of the electric field components of the incident pulsed beam. $\chi^{(2)}(\Omega:\omega+\Delta\omega,-\omega)$ refers to the second-order nonlinear susceptibility (or the nonlinear optical coefficient of the crystal) [1, 27].
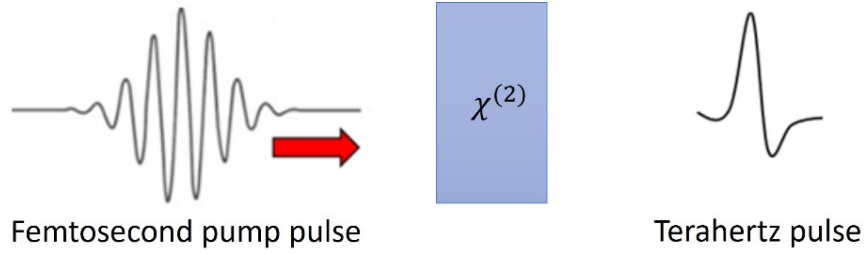
Figure 1.2. An illustration of the THz generation via OR.

In 1962, Bass *et al.* were the first to report DC OR. They used a ruby laser to send 100-ns pulses of radiation through potassium dihydrogen phosphate (KDP) and potassium deuterium phosphate (KD$_d$P) [28]. In 1971, Yang *et al.* demonstrated the generation of far-infrared radiation using picosecond light pulses in LiNbO$_3$, which contained THz frequencies and marked the first experimental evidence of optical THz generation [29]. The first demonstration of the generation of single-cycle THz pulses by OR in LiNbO$_3$ using a femtosecond laser was conducted by Auston *et al.* in the year 1984 [30].

1.3.1. Semiconductor THz sources

The generation of THz radiation from OR of femtosecond laser pulses has been observed in crystals with zincblende semiconductors, such as GaP, GaAs, ZnTe, CdTe, InP, ZnSe, etc., that have a cubic structure with $\bar{4}3$m point group symmetry. These crystals possess only one independent nonlinear optical coefficient, which is $r_{14} = r_{25} = r_{36}$ [1]. ZnTe is the most popular semiconductor crystal for generating THz radiation by OR. Energies up to 1.5 μJ are observed in single-cycle THz pulses with a 3 THz spectral range using OR

4

THz source in a large aperture ZnTe crystal [22]. The investigation of THz pulses generated by OR from a GaAs-based tilted pulse-front pumping (TPFP) at a wavelength of 1.8 μm, which leads to a 0.05% energy conversion efficiency, is close to those usually reported for the TPFP scheme in LiNbO₃ crystals at 800 nm, which also indicates the potential of the GaAs source towards high-field and broadband THz pulse generation [31]. A new method for generating high-energy THz pulses has been suggested using semiconductor materials. By pumping these materials with infrared wavelengths long enough to minimize both two- and three-photon absorption, as well as the associated free-carrier absorption at THz frequencies, researchers achieved significant results. THz pulses with an energy of 14 μJ were generated with an efficiency of up to 0.7% in ZnTe when pumped at a wavelength of 1.7 μm. It is possible to scale the THz pulse energy to the mJ level by increasing both the pump spot size and the pump pulse energy [32]. Fülöp *et al*. suggested compact, monolithic, and alignment-free THz sources, collinearly pumped at an infrared wavelength beyond the three-photon absorption (3PA) edge and utilizing a contact grating (CG) for tilting the pump-pulse front. Suppression of free-carrier absorption at THz frequencies in this way resulted in 0.3% THz generation efficiency, two orders of magnitude higher than reported previously from ZnTe [33].

The broadband THz generation was suggested from 0.1 to 6 THz with a phase grating etched on the surface GaP CG source and a GaP CG detector pumped at a wavelength of 1.03 μm [34]. Using rectangular CG profiles [35], it is possible to get diffraction efficiencies of more than 91% in GaP and 89% in GaAs by adding the right antireflective (AR) coating to the gratings. These techniques can also be used on semiconductor contact gratings, like ZnSe and CdTe [36]. Tibai *et al*. showed with numerical calculations that 45 μJ of THz energy and 17 MV/cm of a focused (by an off-axis parabolic (OAP) mirror) peak THz electric field can be achieved to make a single-cycle THz pulse using transmissive nonlinear echelon slab setup [37]. Recently, the CO_2 laser pumped GaAs OR THz source can be a high energy and extremely high plug-in efficiency device, which can be used for THz-driven particle accelerators [38]. At high laser power excitation, the generation of a reflected THz signal at normal incidence through OR in a ZnTe crystal was also reported [39].

1.3.2. Organic crystal THz sources

Recently, several non-centrosymmetric organic crystals have shown high efficiencies in THz generation via OR of ultrafast laser pulses. These crystals include DAST, DSTMS, OH1, HQM-TMS, and BNA [40-42]. Organic crystals have shown to be excellent THz sources due to their properties such as high optical to THz conversion efficiency due to a high nonlinear optical coefficient, low THz wave absorption, and simple experimental setup due to collinear phase matching. However, they have poor thermal properties and low damage thresholds, so high input intensities can damage them easily. Among these organic crystals, DAST is one of the most widely used organic crystals for THz wave generation. This is mostly because it has an extremely high optical non-linear coefficient ($d_{11} = 290 \pm 55$ pm/V at $\lambda = 1.5$ μm), low absorption of optical and THz waves [43, 44]. The phase-locked THz pulses with electric field amplitudes exceeding 1 MV/cm, magnetic field strengths beyond 0.3 T and pulse energy ~20 μJ at a central frequency of 2.1 THz are efficiently generated by OR in DAST crystal, pumped by an intense infrared source delivering up to 950 μJ on target [45]. Vicario *et al.* investigated the generation of THz waves in organic crystals DSTMS, DAST, and OH1 by OR [46]. This was achieved by directly pumping the crystals with a femtosecond Cr:fosterite laser pulse, with a central wavelength of 1.25 μm and a repetition rate of 10 Hz. Their experimental setup allowed for the production of tightly focused pulses with energy levels in the range of a few hundred μJ. Consequently, this resulted in electric and magnetic fields of 18 MV/cm and 6 T, respectively. Notably, the organic crystal OH1 exhibited a maximum conversion efficiency of up to 3.2%, that corresponds to energy per pulse up to 270 μJ [46].

Optical rectification in the DSTMS crystal pumped by the Cr:Mg$_2$SiO$_4$ laser produced high-THz pulse energy of 0.9 mJ transients between 0.1 and 5 THz with an extremely large field strength of 42 MV/cm (experimentally) and 80 MV/cm (theoretically). This pump source provides high pulse energy and an excellent beam profile for efficient THz generation in the partitioned, large-size DSTMS crystal [47]. Additionally, the organic crystal DSTMS was capable of generating ultra-broadband THz pulses that covered an exceptionally wide frequency range, spanning from 0.5 to 26 THz. These pulses were generated through difference-frequency generation within the spectrum of ultrashort Ti:

sapphire laser pulses [48]. A study has been conducted in recent years on organic crystals for high repetition rate regimes. For example, HMQ-TMS [49] and BNA [50] have shown the first promising results, which exhibit an average THz power of approximately 1.38 mW and 0.95 mW, respectively, when stimulated at a rate exceeding 10 MHz. Furthermore, a more recent demonstration displayed the high-power operation of BNA, accompanied by high fields at 540 kHz, resulting in an average THz power of 5.6 mW [51]. These results highlight the promise of organic crystal THz sources in the realm of high-field science. However, the utilization of TPFP in organic crystals has not been considered yet. This is due to two inherent characteristics of organic crystals: exceptionally large nonlinear coefficients and the fact that they can only be grown in the form of thin plates [52].

1.3.3. Lithium niobate THz sources

Lithium niobate is currently a highly popular nonlinear crystal for intense THz sources. Its properties are significant for THz generation by OR. LN has a highly effective nonlinear coefficient, $d_{eff} = d_{33} = 168$ pm/V to a pump wavelength of 800 nm. This value is larger than the typical range of semiconductors, 25 to 80 pm/V, but is smaller than that of organic crystals [26, 53]. LN is available in two distinct forms: congruent (cLN) and stoichiometric (sLN). The latter has been proven to yield slightly higher efficiencies in terms of THz generation. Both types can be conveniently produced in large sizes, reaching dimensions of several centimeters. Specifically, cLN can be grown larger than sLN. To mitigate the occurrence of photorefractive damage, the strong photorefractive effect can be effectively reduced through the process of doping with MgO. Notably, the optimal concentration of MgO doping was determined to be approximately 0.7% for sLN and 6% for cLN [54, 55]. However, due to the large different refractive indices of the group optical pump pulses $n_{opt}^{gr} = 2.206$ [56] and the THz pulse $n_{THz} = 5$ in LN [57], which make phase matching more difficult, cause the THz generation efficiency to remain low; alternative techniques for phase matching are necessary. The technique known as tilted-pulse-front pumping (TPFP), which is a method for phase matching in THz generation using OR, presents new opportunities for generating high-energy THz pulses. The pioneering work of Hebling *et al*. in 2002 introduced this technique. In this technique, an incident pump pulse propagating has a pulse front that is tilted with respect to its

propagation direction. The generated THz is normal to the tilted pulse front of the propagating pump pulse (see Fig. 1.3. a). The velocity matching condition is described as [58]:

$$v_{opt}^{gr} \cos \gamma = v_{THz}^{p} \qquad (1.2)$$

where v_{opt}^{gr} and v_{THz}^{p} are the velocity of the group optical pump pulses and the phase of THz pulses generated, respectively, and γ is the tilted-pulse-front (TPF) angle which is ~63° for LN. The TPFP scheme can also be explained using wavevectors as noncollinear vector phase matching (see Fig. 1.3. b). The angle of the TPF is inherently connected to the angular dispersion of the pulse and can be conveniently employed for a pulse through the use of a diffraction grating and imaging system. The angle of the TPF is associated with angular dispersion based on the following relation [58]:

$$tan \, \gamma = -\frac{n_{opt}}{n_{opt}^{gr}} \omega \frac{d\theta}{d\omega} \qquad (1.3)$$

where $d\theta/d\omega$ is the angular dispersion introduced by the grating.
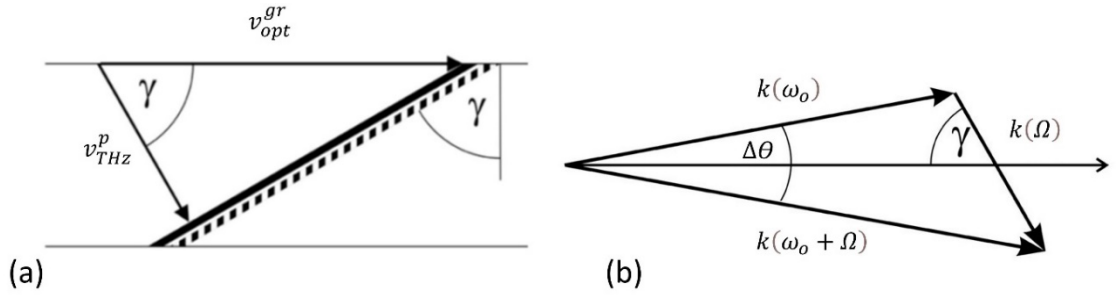
Figure 1.3. (a) Schematic of velocity matching using TPFP. (b) Illustration of TPFP phase-matching (wavevector conservation) for THz generation [59].

The conventional THz excitation scheme with a TPFP consists of an optical grating, an imaging element, and a nonlinear material (NM) (see Fig. 1.4) [23, 59, 60]. Conventional TPFP setups using LN prisms have successfully demonstrated the generation of THz pulses having an energy exceeding 0.4 mJ and an efficiency of 0.77% within the low-frequency domain of the THz spectrum, around 0.2 THz [54]. However, the large wedge angle (tilt angle) and resulting angular dispersion of the pump beam in the prism-shaped LN crystal can severely limit the amount of THz energy that can be generated. As a result, there exist

clear limitations when it comes to further increasing THz energy. These limitations can be categorized as follows: (i) imaging errors occurring at a large spot size and angular dispersion, (ii) the prism-shaped LN crystal with a large wedge angle, $\gamma = 63°$, (iii) limited interaction length due to angular dispersion. In principle, limitations (i) and (ii) can be significantly reduced by using a hybrid type TPFP setup, which is the combination of the conventional setup containing imaging optics and the contact grating [61-64]. However, the efficient generation of THz pulses has not yet been achieved due to technical difficulties caused by the required large tilt angle.
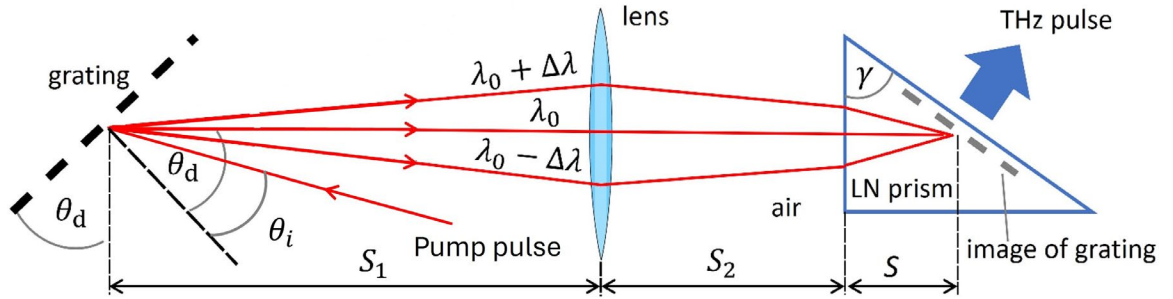
Figure 1.4. Schematic description of the conventional TPFP THz source setup [23].

In order to address limitation (iii), various modified versions of the TPFP THz generation schemes were introduced. In 2016, Ofori-Okai *et.al.* presented a setup that utilized a stair-step reflective echelon (RES) structure instead of a reflective optical grating. In this setup, the pump beam is reflected on a RES, resulting in the formation of a discrete TPF. This segmented intensity front then generates the THz pulse inside the NM [65]. The conversion efficiency achieved was 0.33% at a cryogenic temperature, and a THz pulse energy of 3.1 µJ with a peak field of 0.5 MV/cm was demonstrated. This was achieved with a repetition rate of 1 kHz, a pulse duration of 70 fs, and a pulse energy of 0.95 mJ [65]. More recently, an experimental study reported a conversion efficiency of 1.3% at room temperature. This setup was capable of generating an average power of 74 mW and a focus of 0.4 MV/cm in the LN. The pump pulse duration used was 280 fs, in combination with an RES mirror and an off-axis ellipsoidal mirror [66]. In 2017, Avetisyan *et.al.* proposed a scheme known as the multistep phase mask scheme. This scheme involves splitting a single input beam into multiple smaller "beamlets" with varying time delays. The advantage of this scheme over the grating method is that it reduces the negative impact of angular dispersion and eliminates the need for imaging optics [67]. A new hybrid-type TPFP setup,

a so-called nonlinear echelon slab (NLES) was proposed [68], which is a combination of the conventional TPFP scheme, containing diffraction optics and imaging, and a plane-parallel LN slab with an echelon-like profile created on its entrance surface. The plane-parallel property is the most significant advantage of this setup as it plays a crucial role in efficiently producing a high-quality, symmetric THz beam [68]. Nugraha *et al*. demonstrated the corresponding experiment in 2019 (see Fig. 1.5. a). They were able to generate a single cycle pulse with a specific 2.5 mJ pump pulse energy, 200 fs pulse duration, and 1030 nm central wavelength, resulting 1 μJ pulse energy and 0.3 THz central frequency with 5×10^{-4} % efficiency [69].
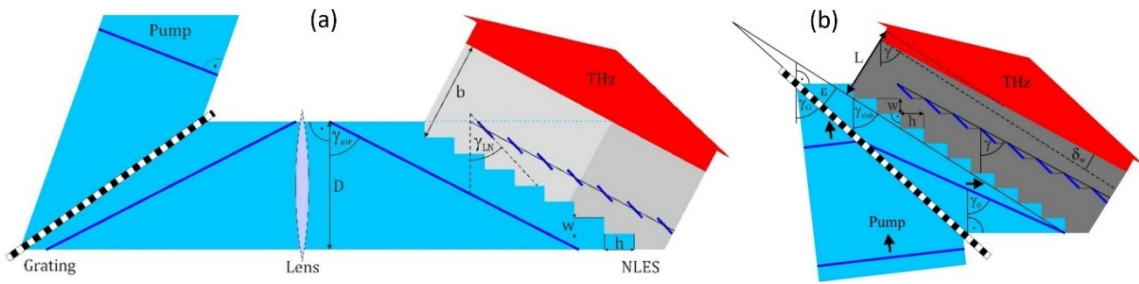
Figure 1.5. (a) Schematic of hybrid NLES THz source setup with imaging [69]. (b) Schematic of hybrid NLES THz source setup without imaging [70].

To further enhance performance, it is recommended to remove the lens behind the grating (compact, imaging-free TPFP) by using wedged shape NLES with 8-10° (see Fig. 1.5. b) [70]. A key feature of the setup is that for about 68° pre-tilt angle and 8.62° LN wedge angle, a uniform THz waveform can be achieved across the entire beam cross section, allowing for a variety of applications and perfect focusing [70]. The transmission grating can decrease this wedge angle even more, provided that it is not used in the exact Littrow configuration [71]. These new hybrid configurations hold great promise in terms of generating a more uniform THz beam profile, which in turn can lead to improved focus and the achievement of a higher peak field [72]. Recently, the corresponding experiment was demonstrated with a small wedge angle ($< 8°$) by Krizsan, G. *et al*. in 2023. Single-cycle pulses of more than 40 μJ energy and 0.28 THz central frequency have been generated by 100 mJ, 400 fs pump pulses with 4.1×10^{-4} efficiency and excellent beam quality [73]. Tóth *et al*. in 2019 proposed a remarkably simple, compact and energy scalable TPFP THz pulse source setup, so called reflective nonlinear slab (RNLS). In this

new setup imaging optics and a pre-tilt for the pump beam are not required. High THz energy with excellent THz beam properties is expected to generate a 50 MV/cm focused field with 10.8 mJ THz pulse energy with 1.25% efficiency, using 870 mJ pump pulse energy, a 1030 nm central wavelength, and a 1 ps pulse duration for a 7 cm diameter LN crystal [74].

Recently, there have been reports of a remarkable high-energy THz pulse 1.4 mJ with a peak electric field of 6.3 MV/cm and a conversion efficiency of 0.7% from LN using the TPFP technique [75]. In the same year, it was achieved that high-field THz pulse train generation from congruent LN with the TPFP technique resulted in a peak electric field strength exceeding ∼1.8 MV/cm and an optical to THz conversion efficiency of 0.55% at 0.26 THz with a pump energy of 20 mJ [76]. Furthermore, a theoretical and experimental demonstration of a new THz pulse source in transmission geometry, based on OR in LN using the TPFP technique, has been made. This involves introducing pulse-front tilt through a volume phase holographic grating (VPHG) that is efficiently used at perpendicular incidence in transmission. The THz pulses are then produced in a LN plane parallel NLES, arranged parallel to the grating [77]. Most recently, it has been reported that single-cycle extreme THz pulse energy of 13.9 mJ, focused peak electric field strength of 7.5 MV/cm, and energy conversion efficiency of 1.2% from 800 nm to THz can be achieved using cryogenically cooled LN crystals with the TPFP technique [78]. These newly developed sources for generating THz pulses, based on TPFP in LN, have the potential to significantly advance the progress of THz-driven electron and proton acceleration. Additionally, they may also pave the way for a new generation of THz pulses in the low THz frequency range of 0.1 to 1 THz. These pulses would possess extremely high energy in the tens of millijoules and electric field strengths in the order of a hundred MV/cm. However, the current limitation lies in the inability to focusing of high-energy THz pulses to the diffraction limit.

1.4. High Numerical Aperture Focusing with Parabolic Mirrors

When radially polarized beams are tightly focused with a high numerical aperture (NA) optical system, such as a parabolic mirror or an aplanatic lens, it results in a smaller focal

spot and a strong longitudinal electric field component and provides a finite field amplitude in the vicinity of the focus than linearly polarized beams [79-82]. On the other hand, the azimuthally polarized field creates a strong magnetic field on the optical axis, with the electric field being purely transverse and zero at the center [83]. The size of a focal spot decreases with an increase in aperture angle and a decrease in wavelength [81]. Nevertheless, the maximal aperture angle is constrained within a single lens focusing system. The principle of 4π focusing has been proposed to enhance the NA of a focusing system [84, 85]. The paraboloid mirror possesses the capability to focus light within a 4π solid angle [86-88]. The investigation of 4π focusing of radially polarized beams has been undertaken due to their interesting characteristics. Bokor and Davidson have demonstrated that it is possible to produce a sharply defined focal spot exhibiting nearly perfect spherical symmetry and exceptionally low sidelobes through the 4π focusing of radially polarized beams [89]. Chen and Zhan have suggested that a spherical focal spot may be generated in a 4π configuration utilizing radially polarized beams with spatial amplitude modulation [90]. The same research group has explored the 4π focusing capabilities of radially polarized vortex beams that incorporate amplitude modulation [91]. Furthermore, multiple on-axis spherical spots can be produced within a 4π focusing system employing radially polarized beams with amplitude modulation [92], and the position of the focal spot has the potential to shift along the axis [93]. Additionally, it is feasible to generate a focal spot characterized by a dark core and nearly perfect spherical symmetry within a 4π focusing system when illuminated by radially polarized first-order Laguerre−Gaussian beams [94]. It has been demonstrated through both experimental and theoretical methods that parabolic mirrors possess the capability to focus a radially polarized beam into a significantly tighter focal spot compared to aplanatic lenses [95, 96].

1.5. Electric Field Distribution Characteristics in the Focal Area

In order to accurately determine the electric and magnetic field distributions for all polarization components under the condition of tight focusing, it is necessary to employ the vector diffraction theory. The rigorous vector diffraction theory of the tight focusing problem began with Ignatowski's solution of Maxwell's equations under certain boundary conditions in cylindrical coordinates [97, 98]. On the other hand, Richards and Wolf [99]

presented an alternative theoretical approach. They precisely defined strongly focused beams in relation to the field distribution of the collimated input beam at the entry pupil of the focusing apparatus. Focusing of radially polarized beams with a high-NA parabolic mirror has been extensively explored in previous studies [80, 87, 100, 101] that based on the Richards−Wolf theory [99]. The primary driver behind this studies were the advancements in microscopy [88, 96]. Various methods exist for the assessment of tightly focused beams, which are based on the Stratton−Chu formulation [102] of Green's theorem. This formulation incorporates the electric and magnetic fields by substituting values derived from Maxwell's equations. The Stratton−Chu vector diffraction theory typically offers more accurate results than the Richards−Wolf theory, particularly in situations involving long wavelengths. Based on the Stratton−Chu vector diffraction theory, focusing of linearly polarized monochromatic electromagnetic plane waves by a paraboloid [103, 104] is well elaborated. Furthermore, this theory is combined with the coherent superposition of monochromatic fields to address the focusing of ultrashort broadband THz pulses [105-107]. In 2019, Zegn and Chen proposed a precise analytical technique for characterizing the vector electromagnetic fields produced by an on- and off-axis parabolic mirror for circular and square incident beams, based on the Stratton−Chu integral [108]. In 2021, the same research group demonstrated an optimization process for the OAP mirror geometry in order to maximize the intensity of the focus, based on an accurate understanding of the tightly focusing properties of OAPs, by employing the Stratton−Chu vector diffraction integrals and physical optics approximations. They were able to derive the optimal configuration scale rule, which allows for the attainment of the highest peak intensity [109]. Recently, the derivation for the electric field, when a radially polarized monochromatic, flat-top [110] beam is focused by an on-axis parabolic mirror has been presented, based on the Stratton−Chu integrals [111]. It has been shown that using monochromatic plane waves and on-axis focusing geometry with a large NA result in the generation of a strong longitudinal electric field at the focal point. More details of focusing of radially polarized monochromatic electromagnetic plane waves will be discussed in Chapter 4. The Richards−Wolf diffraction model has been used to examine the focusing of radially polarized Gaussian beams of low and large numerical aperture, showing the predominant longitudinally polarized component at high NA and high radius [112, 113].

However, a radially polarized beam with uniform cross-sectional amplitude is inconsistent with Maxwell's equations. For example, it is immediately apparent that it contradicts Gauss's Law. Starting from the paraxial wave equation concerning the vector potential in Lorentz gauge, Kirk T. McDonalds has found an *Axicon Gaussian Vector Beam* solution having axial and radial electric, and azimuthal magnetic field components [114]. Rigorously, the requirement for the applicability of the Stratton−Chu integrals is that the beam going to be focused has to be consistent with Maxwell's equations. In this thesis the focusing properties of radially polarized Gaussian vector beams based on the Stratton−Chu vector diffraction theory and their potential applications will be discussed in Cheaper 5. Up until now, most of the research on radially polarized beams has been focused on the visible and infrared spectrum, with limited results in the THz regime.

1.6. Generation of Longitudinally Polarized THz Radiation

By tightly focusing radially polarized THz radiation, longitudinal polarized THz electric fields can be generated, and these fields have significant applications in electron acceleration [115, 116], fluorescent imaging [117], laser machining [118], optical tweezers [119], microscopy [120], etc. In recent years, numerous research teams have made considerable progress in developing a range of techniques for generating strong longitudinally polarized THz electric fields. These methods are velocity-mismatched OR [121], segmented nonlinear crystals [122, 123], an air plasma filament [124], photoconductive antennas with radial electrode geometries [125, 126], and spintronic emitters [19]. Compared to optical frequencies, the successful generation of THz radiation with longitudinal polarization is a recent development. It is quite common to achieve THz pulses with transverse field amplitudes exceeding MV/cm [23, 59, 127]. Minami *et al*. in 2013 reported a field amplitude of 0.001 MV/cm by tightly focusing the THz radiation generated from an air plasma filament induced by a 4.5 mJ femtosecond optical laser pulse [124].

In a demonstration, a matched pair of polarity inverted MgO:sLN crystals were used as an OR source, resulting in the generation of strong on-axis THz radiation with single-cycle duration and electric field amplitudes exceeding 0.011 MV/cm [123]. Another study

utilized amplified laser pulses to excite a large-area spintronic source, producing an electric field of 0.3 MV/cm at the focus of the THz beam [19]. Under similar conditions, a field strength of 1.2 MV/cm was reported using a TPFP scheme in LN crystals [127]. However, it is possible to generate radially polarized THz fields with record-breaking field strength exceeding 1.5 MV/cm through the interaction of lasers with thin metallic foils, resulting in quasi-single-cycle and longitudinally polarized THz output [128]. In a more recent development, the emission from spintronic emitters can be controlled by a magnetic field, allowing for the production of a longitudinal THz electric field with a peak value of 0.0177 MV/cm [129]. Spintronic THz emitters possess unique properties [130], and there are alternative methods to generate strong longitudinally polarized fields.

1.7. Terahertz Pulse Driven Charged Particle Acceleration

THz pulses possessing an extremely high field strength are well-suited for the acceleration of charged particles due to their appropriate wavelength and temporal period. Numerous approaches have been proposed and demonstrated in the literature for the acceleration of particles using laser-driven techniques [131, 132]. Furthermore, there have been reports of the direct acceleration of a freely moving electron in an infinite vacuum along the axis by means of a tightly focused, ultra-intense radially polarized laser beam [133-136]. After, the development of efficient THz generation techniques [137] has made it possible to consider THz pulse-driven particle acceleration as a realistic option, which has encouraged research efforts to explore the use of THz radiation in enhancing electron energy and beam characteristics in high-brightness electron sources [138, 139] and proton post-accelerators [140]. Currently, the utilization of THz pulse-driven particle acceleration in both vacuum [141] and waveguide structures [142] has emerged as a highly active and promising area of study.

The utilization of 20 mJ, 0.6 THz-centered coherent THz pulses within optimized metallic dielectric-loaded cylindrical waveguides was reported as a means to achieve compact electron acceleration and bunch compression [138]. The initial experiment demonstrated the use of an optically generated single cycle THz pulse, having an energy of 1.2 mJ centered at 0.45 THz, for the purpose of linear electron acceleration in the dielectric-loaded

circular THz waveguide. By utilizing 10 µJ THz pulses within a 3 mm interaction length, an acceleration of 7 keV and 25 fC input electron bunch was attained [143]. A successfully fabricated and demonstrated compact THz-driven electron gun, which incorporates a flat copper photocathode, has been reported. The performance of this THz gun has effectively accelerated a 50 fC electron bunch, aligning with the predictions made by particle tracking simulation [144]. A proton accelerator that uses evanescent fields and is driven by high-field and high-energy THz pulses with a single cycle has been reported [140]. Furthermore, the acceleration of a proton beam, driven by an intense THz laser field originating from a near critical density hydrogen plasma, has also been reported [145].

The tightly focused nature of the THz pulses may serve as one of the potential solutions for achieving efficient particle acceleration through the use of THz pulse. The phenomenon of accelerating individual electrons and groups of electrons to relativistic energies by employing counter-propagating THz pulses that are focused has been reported. According to the proposed configuration, the acceleration of electron groups from a state of rest up to 150 keV is projected to occur by employing single-cycle THz pulses possessing an energy of 1 mJ and a central frequency ranging from 0.1 to 3.0 THz [146]. Turnár *et al.* in 2024, conducted further investigation on the previously mentioned setup [146], in which counter-propagating THz pulses were employed to directly accelerate electrons originating from a gas jet, with the process of ionization being conducted by employing an intense and ultrashort optical laser pulse [147]. In 2018, Zhang *et al.* successfully demonstrated the functionality of a novel segmented THz electron accelerator and manipulator (STEAM), a remarkably compact device designed for the purpose of acceleration and manipulation of electron bunches. This STEAM device possesses the ability to dynamically transition between various modes, including acceleration, streaking, focusing, and compressing. Furthermore, it has the capacity to support multiple picocoulombs of charge and boasts intrinsic synchronization. By utilizing merely a few microjoules of single-cycle THz radiation, they were able to exhibit peak acceleration gradients of 70 MV/m, record THz acceleration of > 30 keV [148]. Moreover, in 2019, they demonstrated a two-stage STEAM configuration for the purpose of controlling the energy, energy spread, and emittance of the electron beam. Through the implementation of this setup, they managed to attain a peak acceleration field of 200 MV/m, resulting in a record-breaking THz acceleration of greater

than 70 keV from an injected 55 keV electron beam, thereby leading to an acceleration of electrons of up to approximately 125 keV [149].

It was reported that relativistic electron beams can be accelerated by using a dielectric-lined waveguide driven by narrowband, frequency-tunable, polarization-tailored THz pulses [150]. According to Turnár *et al*. in 2021, 8 fC electron bunches with an energy of up to 340 keV, an energy spread of only 2.0%, and a compressed on-target duration of 200 fs was calculated using single-cycle low-frequency THz pulses with a total energy of less than 4.5 mJ [151]. Another study suggested the acceleration of electron bunches from a state of rest to 8 keV, using single-cycle THz pulses with an energy level of μJ. This acceleration was achieved through the implementation of a horn-shaped metallic waveguide structure [142]. Recently, the generation of 13.9 mJ THz radiation in cryogenically cooled LN was reported. This breakthrough marks a significant advancement, as it raises the energy of crystal-based THz sources from sub-millijoules to over 10 mJ [78]. These sources have the potential to enhance electron energy gain once their radiation energies can be fully utilized. In 2023, Xieqiu *et al*. demonstrated efficient electron manipulation through the utilization of THz surface waves and hollow tube waveguides. Their work focuses on the intense THz source that is based on coherent amplification of the surface wave by free electrons, considering its radial polarization, conversion efficiency (approximately 1%), and high THz energy availability [152].

For decades, research on particle acceleration using focused single-cycle THz pulses created by the OR of ultrashort laser pulses has been investigated. Among them, the direct acceleration of electrons in a vacuum by a tightly focused, ultra-intense radially polarized beam has received particular attention [133-136]. The shape of the electric field of the low-frequency THz pulses at the focus must be carefully taken into consideration in the case of direct electron acceleration [141, 151]. Furthermore, the choice of the paraboloid mirror shape, be it annular or of arbitrary opening, has the potential impact on the sharpness and dimensions of the focal spot. Hence, a paraboloid having one contour is not the optimal focusing element if the objective is to achieve the maximal field component in the *z* direction for a fixed amount of input energy/beam power. Thus, in this thesis, which introduces the proper optical arrangement, including a reflaxicon and a ring-like segment

of an on-axis parabolic mirror as the focusing element, and to analyze the electric field distribution around the focus for a typical geometry. Although the outcome is driven by applications in particle acceleration, it should be noted that the derived formulas apply to electromagnetic waves with arbitrary wavelengths, as illustrated by the example of focusing THz beams. In this thesis the generation of extremely strong accelerating electric field by focusing radially polarized THz pulses with a paraboloid ring that is suitable for vacuum electron acceleration will be discussed in Chapter 6.

2. Theoretical Description

2.1. Scalar Diffraction Theory

Electromagnetic diffraction theory can be classified into scalar diffraction and vector diffraction based on different approximation conditions [153]. Scalar diffraction theory focuses on the scalar amplitude of one transverse component of either the electric or magnetic field, with certain simplifications and approximations. This theory can provide accurate results when the diffracting aperture and observing distance are both much larger than the wavelength, which is particularly relevant for optical systems with a low-NA. However, for high-NA optical systems, where polarization effects are significant near the focal spot, vector diffraction theory must be employed to trace the light field [81, 154]. To study the focusing of short pulses of electromagnetic waves, it is convenient to begin with a scalar diffraction theory. In this section, the approximation of a scalar diffraction theory, specifically the Fresnel−Kirchhoff and Rayleigh−Sommerfeld diffraction formulas, derived from the scalar wave equation and Green's theorem are examined. The diffraction field is dependent on both the shape of the aperture and the characteristics of the incident waves. These incident waves typically encompass plane waves, spherical waves, and several types of beams.

2.1.1. Fresnel−Kirchhoff Diffraction Theory

Extensive discussions of Fresnel−Kirchhoff Diffraction theory are found in many textbooks on theoretical optics. Here, we provide a brief outline without much rigor. A suitable starting point is the scalar Helmholtz equation,

$$\nabla^2 U + k^2 U = 0 \tag{2.1}$$

where U is a scalar complex function which represents an electromagnetic component.

Kirchhoff in applying Green's theorem and in choosing a free space Green's function a unit-amplitude spherical wave expanding about a point P_0:

$$G = \frac{\exp(ik|\mathbf{r} - \mathbf{r_0}|)}{|\mathbf{r} - \mathbf{r_0}|} \tag{2.2}$$

where $k = 2\pi/\lambda$ is wavenumber, λ is the wavelength of the incident, $\mathbf{r_0}$ and $\mathbf{r}$ are the vectors pointing on the closed surface S and the observation point P_0, respectively. In the integration, $\mathbf{r}$ is a variable and $\mathbf{r_0}$ is a constant (see Fig. 2.1).
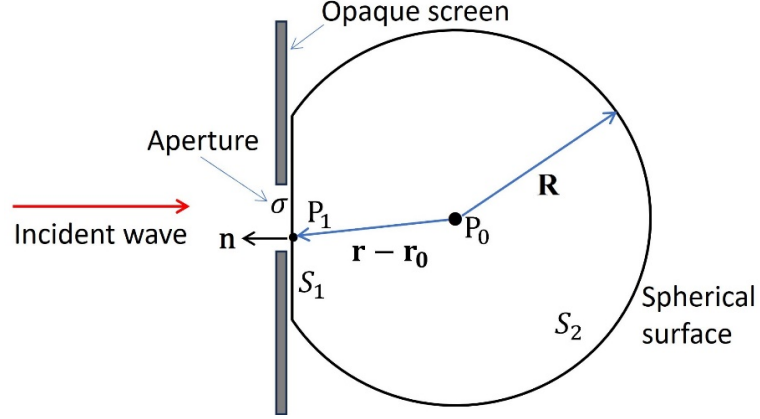
Figure 2.1. Kirchhoff formulation of diffraction by a plane opaque screen.

Note here that Green's function is defined for the complete space, and not in a half one only. Moreover, one can prove that the function U, because it satisfies the Helmholtz equation, also satisfies the Sommerfeld's radiation condition:

$$\lim_{R \to \infty} R \left(\frac{\partial U}{\partial n} - ikU \right) = 0 \qquad (2.3)$$

which implies that the integral in Eq. (2.14) over S_2 will vanish when R becomes arbitrary larger. Next, we conduct integration on the surface S_1. The values of U and its derivative $\partial U/\partial n$ are never know exactly, and consequently Kirchhoff made the following assumptions [155, 156]:

1. Across the aperture σ, the field U and its derivative $\partial U/\partial n$ are the same as they would be in the absence of a screen.
2. Over the portion of S_1 that lies in the geometrical shadow of the screen, $U = 0$ and $\partial U/\partial n = 0$.

These assumptions are called Kirchhoff's boundary conditions. By applying these conditions, we find the field U at the point P_0 in front of the aperture:

$$U(P_0) = \frac{1}{4\pi} \iint_\sigma \frac{\exp(ik|\mathbf{r_1} - \mathbf{r_0}|)}{|\mathbf{r_1} - \mathbf{r_0}|} \left[\frac{\partial U}{\partial n} + ik \cos(\mathbf{n}, \mathbf{r_1} - \mathbf{r_0}) \right] dA \qquad (2.4)$$

This formula is referred to as Fresnel−Kirchhoff diffraction formula. The combination of Kirchhoff's two boundary conditions implies that the field is zero in all areas behind the aperture, which contradicts the established physical situation. Another indication of these inconsistencies is the failure of the Fresnel−Kirchhoff diffraction formula to reproduce the assumed boundary conditions as the observation point nears the screen or aperture [155, 156].
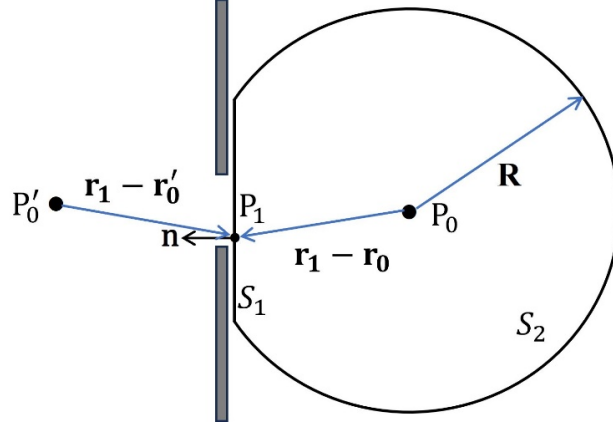
Figure 2.2. Rayleigh−Sommerfeld formulation of diffraction by a point-source illumination of a plane screen.

2.1.2. Rayleigh−Sommerfeld Diffraction Theory

The inconsistency of Kirchhoff's boundary conditions was removed by Sommerfeld by choosing an alternative Green's function. The Green's function in this case is given by

$$G'(P_1) = G'(P_0) - G'(P_0') = \frac{\exp(ik|\mathbf{r_1} - \mathbf{r_0}|)}{|\mathbf{r_1} - \mathbf{r_0}|} - \frac{\exp(ik|\mathbf{r_1} - \mathbf{r_0'}|)}{|\mathbf{r_1} - \mathbf{r_0'}|} \qquad (2.5)$$

where P_0' is the mirror image of P_0 on the opposite side of the screen (see Fig. 2.2).

Using the new Green function, we obtain the following:

$$U_I(P_0) = -\frac{1}{2\pi} \iint_\sigma U(P_1) \frac{\partial G(P_1)}{\partial n} dA \qquad (2.6)$$

This result is known as the first Rayleigh−Sommerfeld solution.

The corresponding normal derivative of G' is

$$\frac{\partial G'(P_1)}{\partial n} = 2\cos(\mathbf{n}, \mathbf{r_1} - \mathbf{r_0}) \left(ik - \frac{1}{|\mathbf{r_1} - \mathbf{r_0}|} \right) \frac{\exp(ik|\mathbf{r_1} - \mathbf{r_0}|)}{|\mathbf{r_1} - \mathbf{r_0}|} \qquad (2.7)$$

Substituting into the first Rayleigh–Sommerfeld solution and enforcing the Kirchhoff boundary conditions, we obtain the exact form of the first Rayleigh–Sommerfeld solution:

$$U_I(\mathrm{P}_0) = \frac{1}{i\lambda} \iint_\sigma U(\mathrm{P}_1) \frac{\exp(ik|\mathbf{r_1} - \mathbf{r_0}|)}{|\mathbf{r_1} - \mathbf{r_0}|} \cos(\mathbf{n}, \mathbf{r_1} - \mathbf{r_0}) \, \mathrm{d}A \tag{2.8}$$

This result is known as the Rayleigh–Sommerfeld diffraction integral. The Sommerfeld formulation resolves the inconsistencies in Kirchhoff's theory. These diffraction formalisms are not applicable for commercially available high-NA lenses or curved mirrors that are commonly used in various optical applications. Moreover, the scalar nature of these diffraction formalisms fails to account for the interdependence of the different components of the electromagnetic fields. To accurately describe the propagation of light in cases where the usual thin lens and paraxial approximations are not valid, a more rigorous approach is required that incorporates the full-vector nature of electromagnetic radiation [155, 156].

2.2. Stratton-Chu Vector Diffraction Theory

Various forms of vector diffraction theories can be obtained through the utilization of a vector analogues of Green's theorem, which serves as the mathematical foundation for scalar diffraction theory. Specifically, Stratton and Chu [102] have developed a precise method for solving diffraction and focusing problems by reformulating them as boundary value problems. Within this specific section, we will discuss the rigorous derivation of the Stratton–Chu integral formulae to obtain the vector wave equations for the electric and magnetic fields.

The starting point in the derivation is to establish vector analogues of Green's first identity and of Green's theorem (or second Green's identity). By applying the divergence theorem to the vector quantity $\mathbf{P} \times \nabla \times \mathbf{Q}$, where $\mathbf{P}$ and $\mathbf{Q}$ are two vector fields within the closed volume V and on the surface S (see Fig. 2.3):

$$\iiint_V [\nabla \cdot (\mathbf{P} \times \nabla \times \mathbf{Q})] \mathrm{d}V = \iint_S (\mathbf{P} \times \nabla \times \mathbf{Q}) \cdot \mathbf{n} \mathrm{d}A \tag{2.9}$$

Remembering the general vector identity:

$$\nabla \cdot (\mathbf{v} \times \mathbf{w}) = \mathbf{w} \cdot (\nabla \times \mathbf{v}) - \mathbf{v} \cdot (\nabla \times \mathbf{w}) \tag{2.10}$$

22

Which is valid for any pair of vectors **v** and **w**, we can expand the integrand in the preceding volume integral and we obtain the vector analogues of Green's theorem:

$$\iiint_V [\mathbf{Q} \cdot \nabla \times (\nabla \times \mathbf{P}) - \mathbf{P} \cdot \nabla \times (\nabla \times \mathbf{Q})] \mathrm{d}V$$

$$= \iint_S [\mathbf{P} \times (\nabla \times \mathbf{Q}) - \mathbf{Q} \times (\nabla \times \mathbf{P})] \cdot \mathbf{n} \mathrm{d}A \quad (2.11)$$

which is the vector analog of Green's second identity. These two integral theorems will be the basis of further derivation [102, 157].

By setting $\mathbf{P} = \mathbf{E}$ and $\mathbf{Q} = G\mathbf{a}$, where $\mathbf{E}$ is the electric field, G is the scalar Green's function (see Eq. (2.2)). Implementing the preceding substitutions for **P** and **Q** in the vector Green's theorem and using the divergence theorem again, it is possible to obtain a surface integral expression for the electric and magnetic fields [158]:

$$\iint_S [i\omega\mu(\mathbf{n} \times \mathbf{H})G + (\mathbf{n} \times \mathbf{E}) \times \nabla G + (\mathbf{n} \cdot \mathbf{E})\nabla G] \mathrm{d}A = 0 \quad (2.12)$$

This result, also referred to as the Stratton−Chu integral theorem [102, 157].
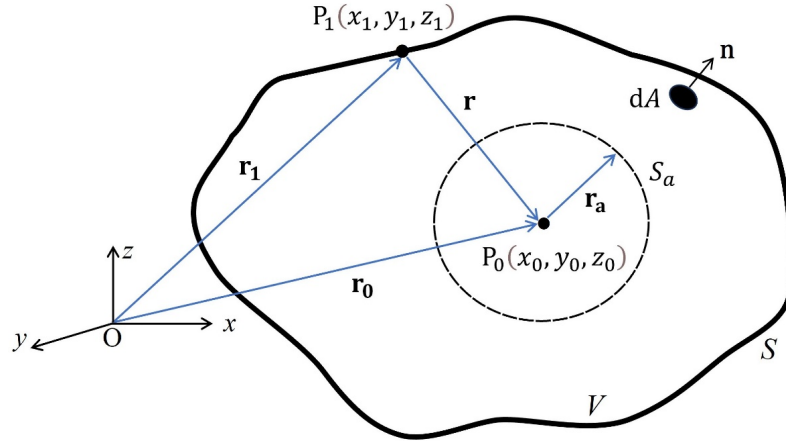
Figure 2.3. Geometry for the Stratton−Chu problem illustrating the closed integration surface with the fixed observation point P_0, the boundary (integration) point P_1 running on the surface S, and a small spherical surface surrounding P_0.

The integration over surface S_a (see Fig. 2.3) can easily be performed retracing the same step that led to the Helmholtz and Kirchhoff integral theorem, leading to a contribution $4\pi\mathbf{E}(P_0)$ when $\epsilon \to 0$. Putting together all the correct expressions for the contributions to

the surface integral in Eq. (2.12), it is possible to obtain an integral expression for the electric field that is given within its interior or on its boundary S:

$$\mathbf{E}(\mathrm{P_0}) = \frac{1}{4\pi} \iint_S [i\omega\mu(\mathbf{n} \times \mathbf{H})G + (\mathbf{n} \times \mathbf{E}) \times \nabla G + (\mathbf{n} \cdot \mathbf{E})\nabla G]\mathrm{d}A. \qquad (2.13)$$

An appropriate interchange of vectors, $\mathbf{E} \to \mu\mathbf{H}$ and $\mathbf{H} \to -\epsilon\mathbf{E}$ yields for the magnetic field $\mathbf{H}$:

$$\mathbf{H}(\mathrm{P_0}) = \frac{1}{4\pi} \iint_S [i\omega\epsilon(\mathbf{E} \times \mathbf{n})G + (\mathbf{n} \times \mathbf{H}) \times \nabla G + (\mathbf{n} \cdot \mathbf{H})\nabla G]\mathrm{d}A. \qquad (2.14)$$

Equations (2.13) and (2.14) are usually referred to as the Stratton−Chu integral formula for electric and magnetic field, respectively, at all points of a volume V with its closed boundary S. The result of these equations holds only if the vector $\mathbf{E}$ and $\mathbf{H}$, and their first derivative are continuous at all points of S. These equations are equivalent to those obtained by Ignatovsky for a closed surface [102].
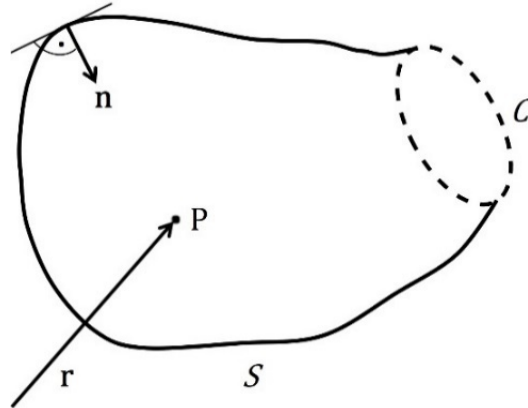
Figure 2.4. P is the observation point at the position r. S is an open surface bounded by a contour, C. n is the inward normal of S.

In many practical cases, the surface being considered is not a continuous (closed) surface; instead, it is bound by a contour C, as shown in Fig. 2.4. In such cases, the surface integral corresponds to a discontinuous (open) surface S and an additional term which describes the effect of contour C. The general expression for the Stratton-Chu integral for the electric $\mathbf{E}$ and magnetic $\mathbf{H}$ fields read as:

$$\mathbf{E}(\mathrm{P_0}) = \frac{1}{4\pi} \iint_S [i\omega\mu(\mathbf{n} \times \mathbf{H})G + (\mathbf{n} \times \mathbf{E}) \times \nabla G + (\mathbf{n} \cdot \mathbf{E})\nabla G]\mathrm{d}A$$

$$+ \frac{1}{4\pi i\omega\epsilon} \oiint_C \nabla G(\mathbf{H} \cdot \mathrm{d}\mathbf{s}), \tag{2.15}$$

$$\mathbf{H}(\mathrm{P_0}) = \frac{1}{4\pi} \iint_S [i\omega\epsilon(\mathbf{E} \times \mathbf{n})G + (\mathbf{n} \times \mathbf{H}) \times \nabla G + (\mathbf{n} \cdot \mathbf{H})\nabla G]\mathrm{d}A$$

$$- \frac{1}{4\pi i\omega\mu} \oiint_C \nabla G(\mathbf{E} \cdot \mathrm{d}\mathbf{s}). \tag{2.16}$$

These formulae must be used for the general case of an aperture with an arbitrary shape bounded by a contour C and an arbitrary wavelength. The detailed derivation found in [102].

2.3. Vectorial Gaussian Beams

Gaussian beam expressions provide a comprehensive description of laser beams. The scalar theory of Gaussian beams serves as an approximation to describe narrow beams of light. A vectorial analysis is required to describe the electromagnetic fields in the focal region with a small spot size. The accurate description of the Gaussian vector beam can be directly derived from Maxwell's equations [159]. Within this section, the paraxial wave equation and its lowest-order linearly and radially polarized solutions are discussed. In 2000, Kirk T. McDonald derived solutions to Maxwell's equation for Gaussian laser beams that can be simplified to the vector Helmholtz equation for the vector potential $\mathbf{A}$ under the conditions of Lorentz gauge [114].

The paraxial wave equation for the spatial envelope function ψ can be written as

$$\nabla^2\psi + 2ik\frac{\partial\psi}{\partial z} = 0. \tag{2.17}$$

where $k = \omega/c$ is a wave number propagating in vacuum along the z-axis.

The function ψ should be expressed in terms of three geometric parameters of a focused beam, the diffraction angle θ_0, the waist w_0, and the depth of focus (Rayleigh range) z_0, which are related by,

$$\theta_0 = \frac{w_0}{z_0} = \frac{2}{kw_0} \qquad and \qquad z_0 = \frac{kw_0^2}{2} = \frac{2}{k\theta_0^2}. \tag{2.18}$$

Introducing scaled coordinates,

$$\xi = \frac{x}{w_0}, \qquad \upsilon = \frac{y}{w_0}, \qquad \zeta^2 = \frac{\rho^2}{w_0^2} = \xi^2 + \upsilon^2, \quad and \quad \varsigma = \frac{z}{z_0}, \tag{2.19}$$

where $\rho^2 = x^2 + y^2$.

Changing variables and using relations in Eqs. (2.18) and (2.19), Eq. (2.17) take the form

$$\nabla_\rho^2 \psi + 4i \frac{\partial \psi}{\partial \varsigma} + \theta_0^2 \frac{\partial^2 \psi}{\partial \varsigma^2} = 0, \tag{2.20}$$

where

$$\nabla_\rho^2 \psi = \frac{\partial^2 \psi}{\partial \xi^2} + \frac{\partial^2 \psi}{\partial \upsilon^2} = \frac{1}{\zeta} \frac{\partial}{\partial \zeta}\left(\zeta \frac{\partial \psi}{\partial \zeta}\right) \tag{2.21}$$

since ψ is independent of the azimuthal ϕ.

The form of Eq. (2.20) suggests that the series expansion [114],

$$\psi = \psi_0 + \theta_0^2 \psi_2 + \theta_0^4 \psi_4 + \cdots \tag{2.22}$$

in terms of the small parameters θ_0^2. Inserting Eq. (2.22) into Eq. (2.20) and collecting terms of order θ_0^0 and θ_0^2, we find

$$\nabla_\rho^2 \psi_0 + 4i \frac{\partial \psi_0}{\partial \varsigma} = 0, \tag{2.23}$$

and

$$\nabla_\rho^2 \psi_2 + 4i \frac{\partial \psi_2}{\partial \varsigma} = -\frac{\partial^2 \psi_2}{\partial \varsigma^2}. \tag{2.24}$$

Equation (2.23) is called the paraxial wave equation, and its commonly accepted fundamental solution of the paraxial equation is the Gaussian beam, which has the form:

$$\psi_0 = f(z)\exp(-f(z)\zeta^2), \tag{2.25}$$

where

$$f(z) = \frac{1}{1 + i\varsigma} = \frac{1}{1 + i\,z/z_0} = \frac{1 + i\,z/z_0}{1 + z^2/z_0^2} = \frac{\exp[-i\tan^{-1}(z/z_0)]}{\sqrt{1 + (z/z_0)^2}}, \tag{2.26}$$

Using Eq. (2.26) into (2.25), the lowest-order wave function ψ_0 is given by

$$\psi_0 = \frac{\exp[-i\tan^{-1}(z/z_0)]}{\sqrt{1 + z^2/z_0^2}} \exp\left[\frac{-\rho^2}{w^2(z)}\right] \exp\left[\frac{ikz\rho^2}{2(z^2 + z_0^2)}\right]. \tag{2.27}$$

where

$$w(z) = w_0\sqrt{1 + z^2/z_0^2} \tag{2.28}$$

is the characteristic transverse size of the beam at position z. The factor $\exp[-i\tan^{-1}(z/z_0)]$ in ψ_0 is the so-called Gouy phase shift, which changes from 0 to $\pi/2$ as z varies from 0 to ∞, with the most rapid change near the z_0 [114].

Considering that the vector potential $\mathbf{A}$ satisfies the free-space wave equation,

$$\nabla^2\mathbf{A} = \frac{1}{c^2}\frac{\partial^2\mathbf{A}}{\partial t^2}. \tag{2.29}$$

The solution in which the vector potential $\mathbf{A}$ is described by a single Cartesian component A_j that propagates in the $+z$ direction with the form,

$$A_j(r,t) = \psi(\rho, z)\exp(i\varphi), \tag{2.30}$$

in the absence of temporal pulse shape, where the phase φ is given by

$$\varphi = kz - \omega t. \tag{2.31}$$

For linearly polarized Gaussian beam, the x component of the vector potential only non-zero and has the form using the scalar wave function ψ_0 becomes,

$$A_x = \frac{E_0}{ik}\psi_0\exp(i\varphi), \qquad A_y = A_z = 0, \tag{2.32}$$

The corresponding electric $\mathbf{E}$ and magnetic $\mathbf{H}$ fields components of linearly polarized Gaussian vector beam is given by [114],

$$E_x(\rho, z) = E_0 f(z)\exp\left(-f(z)\frac{\rho^2}{w_0^2} - ikz\right),$$
$$E_y = 0, \tag{2.33}$$
$$E_z(\rho, z) = -i\theta_0 f\left(\frac{x}{w_0}\right)E_x,$$

and

$$H_x = 0,$$
$$H_y(\rho, z) = E_x(\rho, z), \tag{2.34}$$
$$H_z(\rho, z) = -i\theta_0 f\left(\frac{y}{w_0}\right)E_x.$$

Also, for radially polarized Gaussian beam, the z component of the vector potential only non-zero and has the form using the scalar wave function ψ_0 becomes,

$$A_x = A_y = 0, \qquad A_z = \frac{E_0}{k\theta_0}\psi_0\exp(i\varphi), \qquad (2.35)$$

The corresponding electric $\mathbf{E}$ and magnetic $\mathbf{H}$ fields components of radially polarized Gaussian vector beam in terms of cylindrical coordinate system (ρ, ϕ, z) are given by [114],

$$E_\rho(\rho, z) = E_0 \frac{\rho}{w_0}[f(z)]^2 \exp\left(-f(z)\frac{\rho^2}{w_0^2} - ikz\right),$$

$$E_\phi = 0, \qquad (2.36)$$

$$E_z(\rho, z) = i\theta_0 E_0[f(z)]^2\left(1 - f(z)\frac{\rho^2}{w_0^2}\right)\exp\left(-f(z)\frac{\rho^2}{w_0^2} - ikz\right),$$

and

$$H_\rho = 0,$$

$$H_\phi(\rho, z) = E_\rho(\rho, z), \qquad (2.37)$$

$$H_z = 0,$$

apart from the $\exp(-i\omega t)$ factor. In Eqs. (2.33), (2.34), (2.36) and (2.37), the terms proportional to the second and higher order powers of θ_0 are neglected. Furthermore, the transverse electric field is radially polarized and vanishes on the axis. The longitudinal electric field is nonzero on the axis. Near the focus, $E_z \approx i\theta_0 E_0$ and the peak radial field is $E_0/\sqrt{2}e = 0.43E_0$ [114].

A comparison is made between radially and linearly polarized Gaussian beams based on the radial distribution of the amplitude of their transversal electric field components $|E_\rho|$ and $|E_x|$, respectively (see Fig. 2.5). The $|E_\rho|$ of a radially (see Eq. (2.36)) and the $|E_x|$ of a linearly polarized (see Eq.(2.33)) Gaussian beam are plotted in Fig. 2.5 versus ρ/w. $|E_\rho|$ was normalized to 1. The power of the two beams was assumed to be equal as a normalizing condition for $|E_x|$. Note that while w is regarded as the characteristic size of the linearly polarized beam (where $|E_x|$ reaches $1/e$ of its maxima), $w/\sqrt{2}$ is the characteristic size of the radially polarized beam, where $|E_\rho|$ reaches its maxima. At $\rho/w = 1/\sqrt{2}$ both electric

28

field amplitude equals $1/\sqrt{e}$. Owing to the characteristics of the transversal distribution of $\left|E_\rho\right|$ shown in the Fig. 2.5, such beams are called *Doughnut Beams*. Note that the curves shown in Fig. 2.5 are independent of the *z* position. Therefore, *w* was used in the Fig. 2.5 without any argument above.
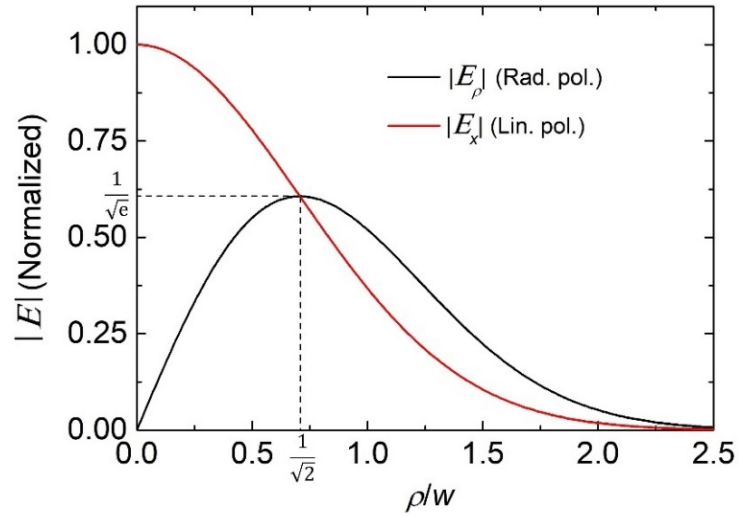
Figure 2.5. The $\left|E_\rho\right|$ ($\left|E_x\right|$) amplitude of the transversal electric field component of a radially (black line) and a linearly polarized (red line) Gaussian beam [160].

3. Scientific Goals

The main goal of the thesis was to investigate theoretically the generation of extremely strong longitudinal electric field by focusing radially polarized monochromatic laser beams and THz pulses using a paraboloid mirror or its segment with perfect reflectance. This involved analyzing the axial and radial distributions of the longitudinal electric field and the pulse characteristics in the focal region, aiming to attain high field intensities suitable for particle acceleration applications.

The specific objectives of the thesis were:
- To derive general formulae for the electric field produced by focusing of radially polarized, monochromatic, flat-top beam using a parabolic mirror. This involves a rigorous theoretical analysis using the Stratton−Chu vector diffraction theory to examine the distribution of the electric field, especially the characteristics of the longitudinal and radial electric field components for particle acceleration applications.
- To develop general formulae for the electric and magnetic field characteristics of a focused radially polarized Gaussian vector beam by a parabolic mirror, based on the Stratton−Chu vector diffraction method. This objective focuses on different numerical apertures and incident beam divergences to determine axial and radial distributions of the longitudinal electric field component, essential for particle acceleration.
- To validate and compare the derivation of the electric field distribution formulae, which are based on the Stratton−Chu vector diffraction theory, with a theory based on Rayleigh–Sommerfeld and Richards−Wolf models in the focal region, specifically for a case involving large NA and short wavelength regimes.
- To generate extremely strong accelerating electric fields by focusing of radially polarized THz pulses with a parabolic mirror ring. The objective here is to create a novel setup using a reflaxicon and a ring-like segment of a parabolic mirror to achieve high field intensities suitable for vacuum electron acceleration. The calculation of electric field distribution in the focal region was performed by the Stratton–Chu vector diffraction method.

- To determine an energy gain on the order of MeV by an electron moving at nearly the speed of light from the study of the acceleration using a simple model and expecting the energy gain to depend on the relative motion direction (same and opposite) of the electron and the sweeping velocity of the field maxima.

4. Focusing of Radially Polarized Electromagnetic Waves by a Parabolic Mirror

4.1. Introduction

A high-NA parabolic mirror with a radially polarized beam is well-suited for achieving a small focal spot size and a strong longitudinal electric field [81, 82], which opens up possibilities for application in particle acceleration [115, 116]. In particle acceleration development, it is crucial to precisely know the characteristics of the electromagnetic field of a focused beam in the focal region. Different vector diffraction methods are necessary to accurately determine all polarization components' electric and magnetic field distributions during tight focusing. The Stratton−Chu vector diffraction method [102] provides more accurate results [108] than the Richards-Wolf method [99], particularly in situations involving long wavelengths. Focusing of linearly polarized, monochromatic electromagnetic plane waves [103, 104], and pulses [105] by a paraboloid is already elaborated based on the Stratton−Chu diffraction theory. A more comprehensive investigation recently reported into applying the vector field focusing properties of electromagnetic fields by a parabolic mirror, based on the Stratton−Chu integral formalism [161-163]. The existing literature does not provide a detailed theoretical and analytical study of the vector field focusing properties of radially polarized beams by on- and off-axis parabolic mirrors based on the Stratton−Chu integral representation. This chapter presents a rigorous derivation of the electric field obtained when a parabolic mirror focuses a radially polarized, monochromatic, flat-top beam. The formulae are deduced from the Stratton−Chu integral, which is well-known in vector diffraction theory. For focusing, a perfectly reflecting large NA on-axis parabolic mirror is supposed to have practical importance. After validation, the electric field for various focusing conditions is determined using these formulae. This chapter explains the first sub-study of the thesis, which is based on *my original scientific results* [111].

4.2. General Formulae of the Parabolic Mirror

In this section, I have compiled the fundamental equations relating to the paraboloid without providing their derivations. Considering an ideal on-axis parabolic mirror with its focus, F, at the origin, O, of a Cartesian coordinate system, with z being the symmetrical axis of the paraboloid, as illustrated in Fig. 4.1. The equation of the paraboloid is given by [103]:

$$z_s = \frac{x_s^2 + y_s^2}{4f_L} - f_L, \tag{4.1}$$

where x_s, y_s and z_s are the coordinates of an arbitrary point S of the paraboloid and f_L is the focal length of the parabolic mirror. Let $r_s = (x_s^2 + y_s^2 + z_s^2)^{1/2}$ is the distance of any arbitrary point, S (x_s, y_s, z_s) lying on the paraboloid surface, S measured from F. Hence it follows from Eq. (4.1) that

$$r_s = z_s + 2f_L. \tag{4.2}$$

Using the spherical coordinate system $(r_s \sin\theta_s \cos\emptyset_s, r_s \sin\theta_s \sin\emptyset_s, r_s \cos\theta_s)$, Eq. (4.2) becomes

$$r_s(\theta_s) = \frac{2f_L}{1 - \cos\theta_s}. \tag{4.3}$$
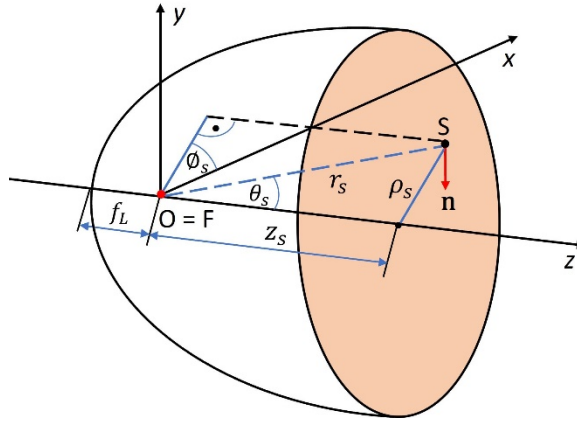
Figure 4.1. Schematic diagram of the parabolic mirror with notations [111].

In a cylindrical coordinate system with z axis, and origin, O the radial and axial coordinates of S are

$$\rho_s(\theta_s) = r_s(\theta_s) \sin\theta_s, \tag{4.4}$$

$$z_s(\theta_s) = r_s(\theta_s) - 2f_L. \tag{4.5}$$

The surface element of the paraboloid dA is given by:

$$dA = \frac{r_s{}^2}{n_z} \sin \theta_s \, d\theta_s d\emptyset_s, \tag{4.6}$$

and the small, azimuthally directed vector line element on the circumference of the paraboloid belonging to θ_s is

$$d\mathbf{s} = 2f_L \cot\left(\frac{\theta_s}{2}\right)\left(- \sin \emptyset_s \, \mathbf{e}_x + \cos \emptyset_s \, \mathbf{e}_y\right) d\emptyset_s. \tag{4.7}$$

The unit vector $\mathbf{n}$ pointing inward normal to the surface of the paraboloid is written as [108]:

$$\mathbf{n}(x_s, y_s) = \frac{-\frac{1}{2f_L}\left(x_s \mathbf{e}_x + y_s \mathbf{e}_y\right) + \mathbf{e}_z}{\sqrt{1 + \frac{x_s{}^2 + y_s{}^2}{4f_L^2}}}, \tag{4.8}$$

where $\mathbf{e}_x$, $\mathbf{e}_y$ and $\mathbf{e}_z$ are the unit vectors pointing into the x, y and z directions, respectively.

Using the spherical coordinate system $(r_s \sin \theta_s \cos \emptyset_s , r_s \sin \theta_s \sin \emptyset_s , r_s \cos \theta_s)$ and Eq. (4.3), the component of the inward directed unit vector $\mathbf{n}$ at a given point, S on the paraboloid surface, S are given by

$$n_x = -\frac{\sin \theta_s \cos \emptyset_s}{[2(1 - \cos \theta_s)]^{1/2}},$$

$$n_y = -\frac{\sin \theta_s \sin \emptyset_s}{[2(1 - \cos \theta_s)]^{1/2}}, \tag{4.9}$$

$$n_z = \left(\frac{1 - \cos \theta_s}{2}\right)^{1/2},$$

where θ_s is the polar, and $\emptyset_s$ is the azimuthal angle as shown in Fig. 4.1.

4.3. The Stratton−Chu Integral Formulae

For fields oscillating with ω angular frequency, Stratton and Chu constituted a formula pair for the electric and magnetic fields, see Eqs. (2.15) and (2.16), which can be regarded as the basic equations of the vector diffraction theory [102]. The Stratton−Chu formulae refer to a discontinuous (open) surface, S bounded by a closed contour, C as illustrated in Fig. 2.4. If the electric $\mathbf{E}$ and magnetic $\mathbf{H}$ fields are known at each $\mathbf{r}_s = (x_s, y_s, z_s)$ point

on S, and along C, then the electric and magnetic fields at $\mathbf{r} = (x, y, z)$ on arbitrary point P can be determined as

$$\mathbf{E}(\mathbf{r}) = \frac{1}{4\pi} \int_S [ik(\mathbf{n} \times \mathbf{H})G + (\mathbf{n} \times \mathbf{E}) \times \nabla G + (\mathbf{n} \cdot \mathbf{E})\nabla G]dA$$

$$+ \frac{1}{4\pi ik} \oint_C \nabla G(\mathbf{H} \cdot d\mathbf{s}) \qquad (4.10)$$

and

$$\mathbf{H}(\mathbf{r}) = \frac{1}{4\pi} \int_S [ik(\mathbf{E} \times \mathbf{n})G + (\mathbf{n} \times \mathbf{H}) \times \nabla G + (\mathbf{n} \cdot \mathbf{H})\nabla G]dA$$

$$- \frac{1}{4\pi ik} \oint_C \nabla G(\mathbf{E} \cdot d\mathbf{s}) \qquad (4.11)$$

with the free-space Green's function, G (see Eq. (2.2))

$$G = \frac{\exp(iku)}{u}, \qquad (4.12)$$

$$\mathbf{u} = \mathbf{r}_s - \mathbf{r}, \qquad (4.13)$$

$$u = [(x_s - x)^2 + (y_s - y)^2 + (z_s - z)^2]^{1/2} = (\Delta x^2 + \Delta y^2 + \Delta z^2)^{1/2}, \qquad (4.14)$$

and the ∇G should be calculated at the points S (x_s, y_s, z_s) of the paraboloid [103]. It can be expressed as:

$$\nabla G = \left(ik - \frac{1}{u}\right)\frac{\exp(iku)}{u^2}\mathbf{u} \qquad (4.15)$$

where $k = \omega/c = \omega\sqrt{\epsilon\mu}$ is a wave number. Let us notice that the expressions for both $\mathbf{E}$ and $\mathbf{H}$ consist of two main terms: a *surface* and a *contour* term, see Eqs. (4.10) and (4.11).

4.4. Vector Diffraction Field of Radially Polarized Monochromatic Plane Waves by Parabolic Mirror

The electric and magnetic fields created by focusing with a segment of a parabolic mirror are calculated by assuming that the segment of the paraboloid is bounded by the vertex V and a plane perpendicular to the optical axis located at $z \leq 0$, as illustrated in Fig. 4.2. Considering the complex electric and magnetic fields at an arbitrary point inside the parabolic mirror – because of practical interest, especially in its focal region. For the derivations, the electromagnetic boundary conditions concerning a perfectly reflecting

surface S, together with relations concerning the different geometry of the paraboloid [103] were used. If an incident beam illuminates the reflecting surface S, then based on the electromagnetic boundary conditions, the electric $\mathbf{E}$ and magnetic $\mathbf{H}$ fields related to the incident fields $\mathbf{E_i}$ and $\mathbf{H_i}$ as [103]:

$$\mathbf{E}(S) = 2\mathbf{n}(\mathbf{E_i} \cdot \mathbf{n}),$$
$$\mathbf{H}(S) = 2\mathbf{H_i} - 2\mathbf{n}(\mathbf{H_i} \cdot \mathbf{n}).$$
(4.16)
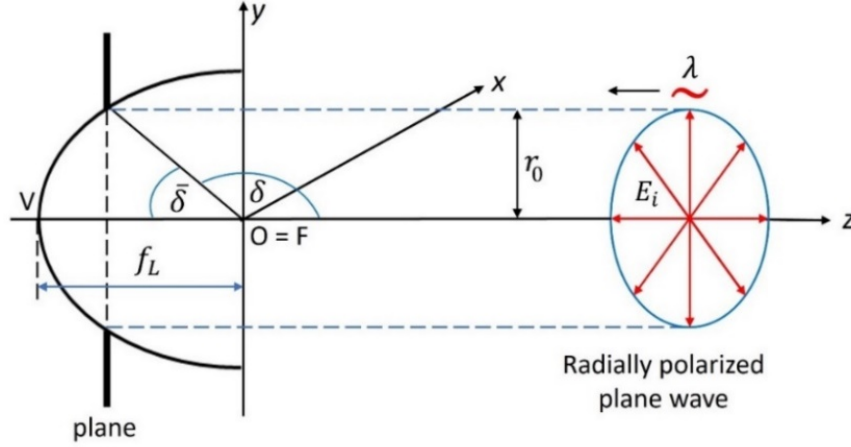
Figure 4.2. Schematic diagram with notations for the study of focusing radially polarized waves by a segment of a parabolic mirror [111].

Let the incoming radially polarized monochromatic plane wave propagate in the negative z direction. In the cylindrical coordinate system $(\rho, \emptyset, z)$, the radially polarized wave has an electric field in the radial direction concerning the propagation axis. In contrast, the magnetic field is aligned in azimuthal orientation. There are no longitudinal components for both electric and magnetic fields. The incident electromagnetic field can be written as:

$$\mathbf{E}_i = a\exp(-ikz)\big[\cos\emptyset\, \mathbf{e}_x + \sin\emptyset\, \mathbf{e}_y\big],$$
$$\mathbf{H}_i = a\exp(-ikz)\big[\sin\emptyset\, \mathbf{e}_x - \cos\emptyset\, \mathbf{e}_y\big],$$
(4.17)

where a represents the constant amplitude of the incoming field.

Let us start by discussing the surface integral term of the electric field in Equation (4.10). Using Eqs. (4.16) and (4.17), the expressions in Eq. (4.10) can be written as

$$\mathbf{n} \times \mathbf{H}(S) = 2an_z \left[\cos \emptyset_s \, \mathbf{e}_x + \sin \emptyset_s \, \mathbf{e}_y \right.$$

$$\left. - \left(\frac{n_x}{n_z} \cos \emptyset_s + \frac{n_y}{n_z} \sin \emptyset_s \right) \mathbf{e}_z \right] \exp(-ikz_s), \tag{4.18}$$

$$\mathbf{n} \times \mathbf{E}(S) = 0,$$

$$\mathbf{n} \cdot \mathbf{E}(S) = 2a(n_x \cos \emptyset_s + n_y \sin \emptyset_s) \exp(-ikz_s).$$

where S in the bracket refers to the surface.

Substituting Eqs. (4.2), (4.8), (4.12), (4.17) and (4.18) into Eq. (4.10), the surface integral term of electric field in Eq. (4.10) one can obtain

$$\mathbf{E}_S(P) = \mathbf{E}_S(\rho, z) = a \frac{\exp(2ikf_L)}{2\pi} ik \int_\delta^\pi \int_0^{2\pi} d\theta_s \, d\emptyset_s \frac{\exp[ik(u - r_s)]}{u} r_s^2 \sin \theta_s$$

$$\times \left\{ \left[\cos \emptyset_s - \cot\left(\frac{\theta_s}{2}\right) \left(1 - \frac{1}{iku}\right) \frac{\Delta x}{u} \right] \mathbf{e}_\rho + \cot\left(\frac{\theta_s}{2}\right) \left[1 - \left(1 - \frac{1}{iku}\right) \frac{\Delta z}{u} \right] \mathbf{e}_z \right\} \tag{4.19}$$

where $\Delta x = r_s \sin \theta_s \cos \emptyset_s - \rho$, $\quad \Delta y = r_s \sin \theta_s \sin \emptyset_s$, $\quad \Delta z = r_s \cos \theta_s - z$ and $u = [\Delta x^2 + \Delta y^2 + \Delta z^2]^{1/2}$. P was supposed to lie on the x axis (see Fig. 4.3). $\mathbf{e}_\rho$ and $\mathbf{e}_z$ are the unit vectors pointing in the radial and axial directions, respectively. Due to the axial symmetry $\mathbf{E}_S(P)$ has no azimuthal component.
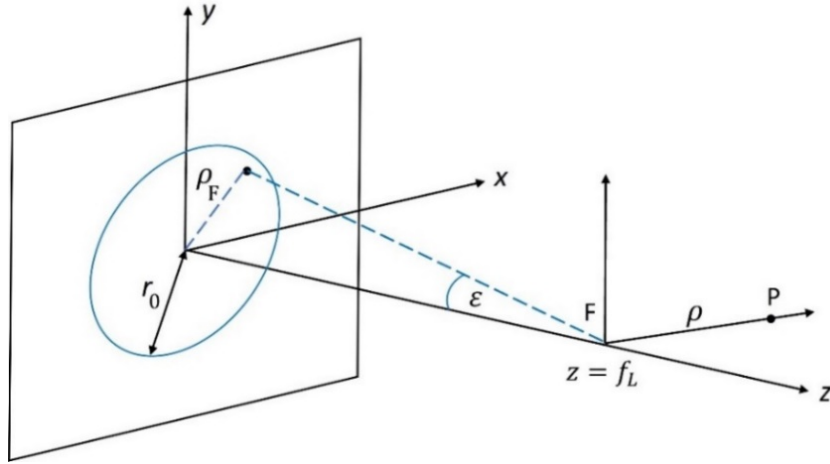
Figure 4.3. Schematic diagram with notations for the study of focusing radially polarized wave with a focusing element (the blue circle in the x-y plane) having small numerical aperture. The observation point P is located at a distance ρ from the z axis. The dashed line is a 'ray' passing through the focus F [111].

Let us now consider the contour integral term of the electric field in Eq. (4.10). From Eqs. (4.9), (4.16) and (4.17), the Cartesian coordinate components (H_x, H_y, H_z) of the total magnetic field can be written as:

$$H_x = 2a \sin \emptyset_s \exp(-ikz(\delta)),$$
$$H_y = -2a \cos \emptyset_s \exp(-ikz(\delta)), \tag{4.20}$$
$$H_z = 0,$$

where $\delta = \theta_s$ is the focusing angle (see Fig. 4.2).

From Eqs. (4.7) and (4.20), the dot product $\mathbf{H}(S) \cdot d\mathbf{s}$ becomes

$$\mathbf{H}(S) \cdot d\mathbf{s} = -4af_L \cot\left(\frac{\delta}{2}\right) \exp(-ikz(\delta)) d\emptyset_s. \tag{4.21}$$

Substituting Eqs. (4.12), (4.15) and (4.21) into (4.10), the contour integral term of electric field in Eq. (4.10) one can obtain

$$\mathbf{E}_C(\mathrm{P}) = \mathbf{E}_C(\rho, z)$$
$$= -\frac{af_L \exp(2ikf_L)}{\pi} \cot\left(\frac{\delta}{2}\right) \int_0^{2\pi} \frac{\exp[ik(u - r_s(\delta))]}{u} \tag{4.22}$$
$$\times \left(1 - \frac{1}{iku}\right)\left(\frac{\Delta x}{u}\mathbf{e}_\rho + \frac{\Delta z}{u}\mathbf{e}_z\right) d\emptyset_s,$$

with $\Delta x = r_s(\delta) \sin \delta \cos \emptyset_s - \rho$, $\Delta y = r_s(\delta) \sin \delta \sin \emptyset_s$, $\Delta z = r_s(\delta) \cos \delta - z$ and $u = [\Delta x^2 + \Delta y^2 + \Delta z^2]^{1/2}$. Due to the axial symmetry $\mathbf{E}_C(\mathrm{P})$ has no azimuthal component.

The total complex electric field can be given as:

$$\mathbf{E}(\rho, z) = \mathbf{E}_S(\rho, z) + \mathbf{E}_C(\rho, z). \tag{4.23}$$

In the following Section, call attention to the fact that, E_ρ and E_z represent the real parts of the complex field components.

Let us continue the derivation for the magnetic field. Using Eqs. (4.16) and (4.17), the expressions in Eq. (4.11) can be written as

$$\mathbf{E}(S) \times \mathbf{n} = 0,$$
$$\mathbf{n} \cdot \mathbf{H}(S) = 0. \tag{4.24}$$

Substituting $\mathbf{n} \times \mathbf{H}(S)$ from Eq. (4.18) into Eq. (4.11), the surface integral for the magnetic field having only azimuthal component one obtains:

$$\mathbf{H}_S(\mathrm{P}) = \mathbf{H}_S(\rho, z) = a \frac{\exp(2ikf_L)}{2\pi} ik \int\limits_{\delta}^{\pi} \int\limits_{0}^{2\pi} d\theta_s \, d\emptyset_s \frac{\exp[ik(u - r_s)]}{u} r_s^2 \sin \theta_s$$

$$\times \left(1 - \frac{1}{iku}\right) \left\{ \left[\cot\left(\frac{\theta_s}{2}\right) \frac{\Delta x}{u} - \cos \emptyset_s \frac{\Delta z}{u} \right] \mathbf{e}_\emptyset \right\}$$

(4.25)

where Δx, Δy, Δz and u are mentioned in Eq. (4.19). $\mathbf{e}_\emptyset$ is the azimuthal unit vector. The dot product $\mathbf{E}(S) \cdot d\mathbf{s} = 0$, hence the contour term for the magnetic field is zero.

4.5. Analyses of the Theoretical Results for Different Focusing Conditions

In this section, the results of calculations using the vector diffraction electric field distribution, previously introduced, are analyzed and discussed for various focusing geometries. It is important to note that parabolic mirrors are commonly used optical elements in experimental setups, especially within wavelength ranges such as THz, where conventional lenses and spherical mirrors are less effective. In the interest of broad applicability, rather than explicitly defining focal length (f_L), the wavelength (λ), and r_0 (which can be interpreted as the incident beam radius, as shown in Fig. 4.2) as absolute parameters, I introduce the ratios λ/f_L and r_0/f_L as relative parameters. This alternative approach allows for a more generalized consideration of these quantities. The relative parameter r_0/f_L is related to the focusing angle δ (see Fig. 4.2) as follows:

$$\delta = \arccos\left(\frac{\frac{1}{4}\left(\frac{r_0}{f_L}\right)^2 - 1}{\frac{1}{4}\left(\frac{r_0}{f_L}\right)^2 + 1}\right),$$

(4.26)

and

$$\bar{\delta} = \pi - \delta.$$

(4.27)

In this analysis, I kept the λ/f_L ratio below 0.1 because the case where λ/f_L is greater than 0.1 is not very relevant in practice. Assuming a standard value of $f_L = 50$ mm, the λ/f_L ratio being less than 0.1 applies not just to the visible and (near-, mid-) infrared, but also to the THz frequency range of $0.1-10$ THz. Even when λ/f_L equals 0.1, the corresponding

frequency is only 0.06 THz. Therefore, for λ/f_L is smaller than 0.1, the entire THz range is covered. The significance of THz fields is remarkable due to their usefulness in particle acceleration [148, 150, 164] because of their advantageous wavelength and the availability of pulses with extremely high energies and electric field strengths using the TPFP technique [54, 75].

Before implementing the above-introduced theory based on the Stratton-Chu formulae, it is essential to validate its reliability. To do so, I compare its results with those obtained from the commonly used scalar diffraction methods, considering separately two perpendicular (x and z) polarization components. The E_ρ and E_z field components obtained using scalar diffraction methods (depicted as red dashed curves in Fig. 4.4) were derived from the Rayleigh-Sommerfeld diffraction formula [155] adapted for the case shown in Fig. 4.3, assuming a 'thin' focusing element. The amplitudes of the aperture functions associated with the transversal and longitudinal field components from the focusing element are

$$E_{F_\rho} = E_0 \cos \varepsilon \cos \emptyset_F = E_0 \frac{f_L}{\sqrt{\rho_F{}^2 + f_L{}^2}} \cos \emptyset_F,$$

$$E_{F_z} = E_0 \sin \varepsilon = E_0 \frac{\rho_F}{\sqrt{\rho_F{}^2 + f_L{}^2}}$$

(4.28)

respectively, where E_0 is the electric field just before reaching the focusing element. The radially dependent part of the phase factor resulting from the focusing element is

$$\exp(-i\varphi_F) = \exp\left(-ik\frac{\rho_F{}^2}{2f_L}\right).$$

(4.29)

Hence,

$$E_\rho(\rho) \propto \int_0^{r_0} \int_0^{2\pi} E_{F\rho}\exp(-i\varphi_F)\frac{\exp(-iku)}{u^2}\rho_F \mathrm{d}\rho_F \mathrm{d}\emptyset_F,$$

$$E_z(\rho) \propto \int_0^{r_0} \int_0^{2\pi} E_{Fz}\exp(-i\varphi_F)\frac{\exp(-iku)}{u^2}\rho_F \mathrm{d}\rho_F \mathrm{d}\emptyset_F,$$

(4.30)

with

$$u = \left(\rho_F{}^2 + f_L{}^2 + \rho^2 - 2\rho\rho_F \cos \emptyset_F\right)^{1/2}. \qquad (4.31)$$

The methodology proposed by Endale *et al.* [113] was also used to analyze the electric field distributions for a flat-top beam as a validation. This approach is based on the diffraction theory established by Richards−Wolf [99]. The resulting curves, computed using this approach, are depicted as blue dotted lines in Fig. 4.4.

Figure 4.4. The transversal distribution of the radial (a,c) and longitudinal (b,d) component of the electric field at $z = 0$ for $\lambda/f_L = 10^{-3}$ and $r_0/f_L = 0.1$ (a,b), $r_0/f_L = 1.8$ (c,d) parameter values. The black solid curves were computed using the Stratton−Chu integral for parabolic mirror, the red dashed ones using the Rayleigh−Sommerfeld integral and the blue dotted ones using theory of Endale *et al.* (Richards−Wolf integral) [111].

Upon analyzing the parameters $\lambda/f_L = 10^{-3}$ and $r_0/f_L = 0.1$ (with corresponding $\bar{\delta} = 5.72°$ angle), it seems that the contour term in my model based on Stratton–Chu is

relatively negligible in comparison to the surface term. It is worth considering that the parabolic mirror can be regarded as thin, which could have potential implications for our model. In this paraxial regime, the results of my (Stratton–Chu) model show excellent agreement with the other two models (Rayleigh–Sommerfeld and Richards–Wolf), as shown in Figs. 4.4 a and b. The Rayleigh-Sommerfeld integral gives a misleading result for $\lambda/f_L = 10^{-3}$ and for large NA ($r_0/f_L = 1.8$ with corresponding $\bar{\delta} = 83.9°$ angle). Even the model of Endale *et al.* [113], which is not restricted to small numerical apertures, only works well in the vicinity of the z-axis for low ρ/λ values, as seen in Figs. 4.4 c and d. These conclusions confirm the necessity of using my model based on Stratton–Chu in large NA regimes when the spatial extension of the parabolic mirror in the z (longitudinal) direction becomes comparable with its transversal extension.
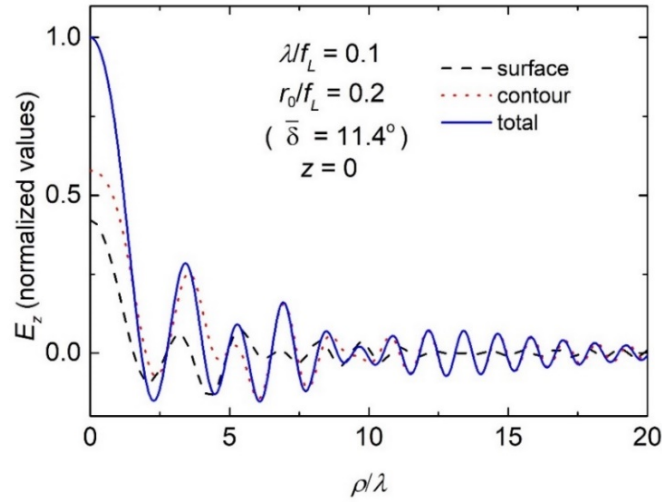
Figure 4.5. The transversal distribution of the longitudinal component of the electric field at $z = 0$ for $\lambda/f_L = 0.1$ and $r_0/f_L = 0.2$ parameter values. The total field (blue solid line) consists of a surface (black dashed line) and a contour (red dotted line) term [111].

In the analysis conducted, it has been established that the contribution of the contour term has been found to be negligible in all cases examined in the following discussion. However, for instance, when $r_0/f_L = 0.2$ and $\lambda/f_L = 0.1$, the surface and contour terms exhibit comparable magnitudes, as illustrated in Fig. 4.5. In this figure, the black dashed line represents the surface term, the red dotted line represents the contour term, and the blue solid line represents their sum, which is the total field component. Under the focusing

conditions in Fig. 4.5 for the field component, the surface term is more dominant than the contour term.

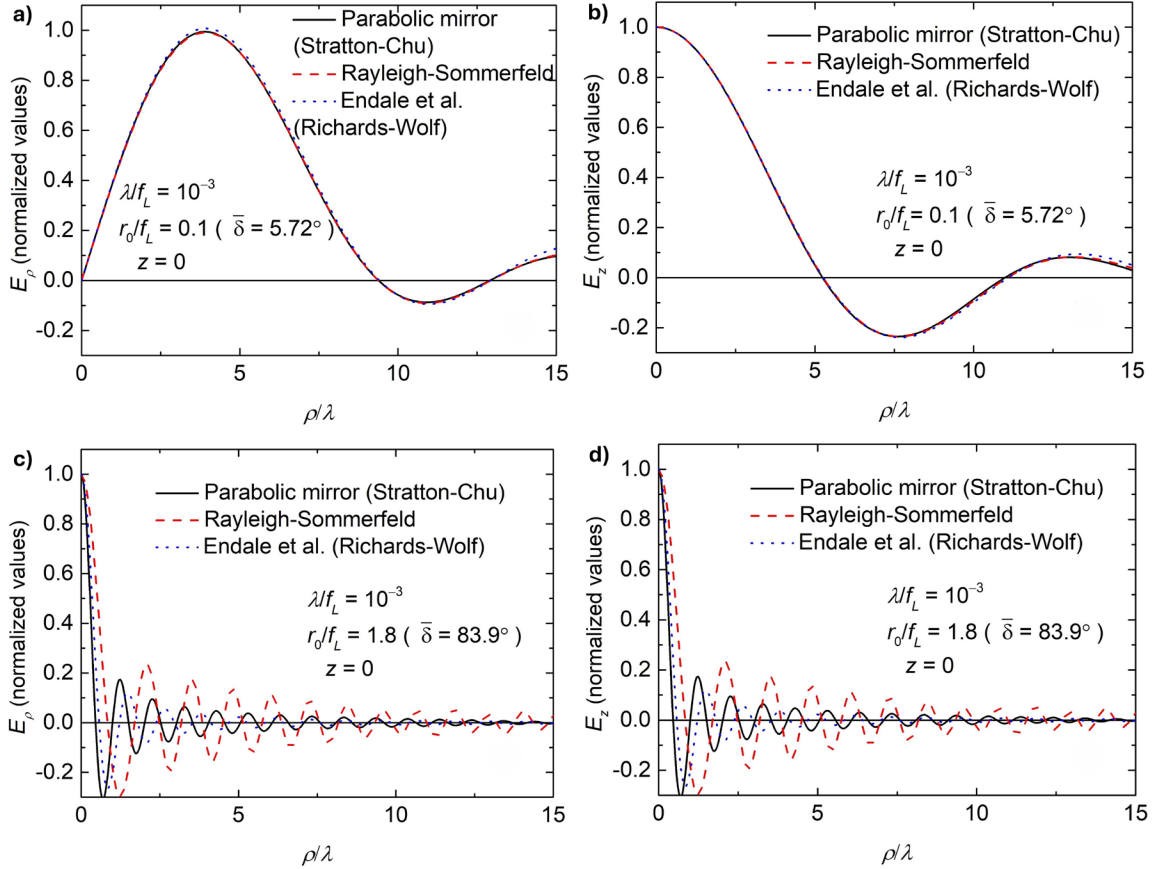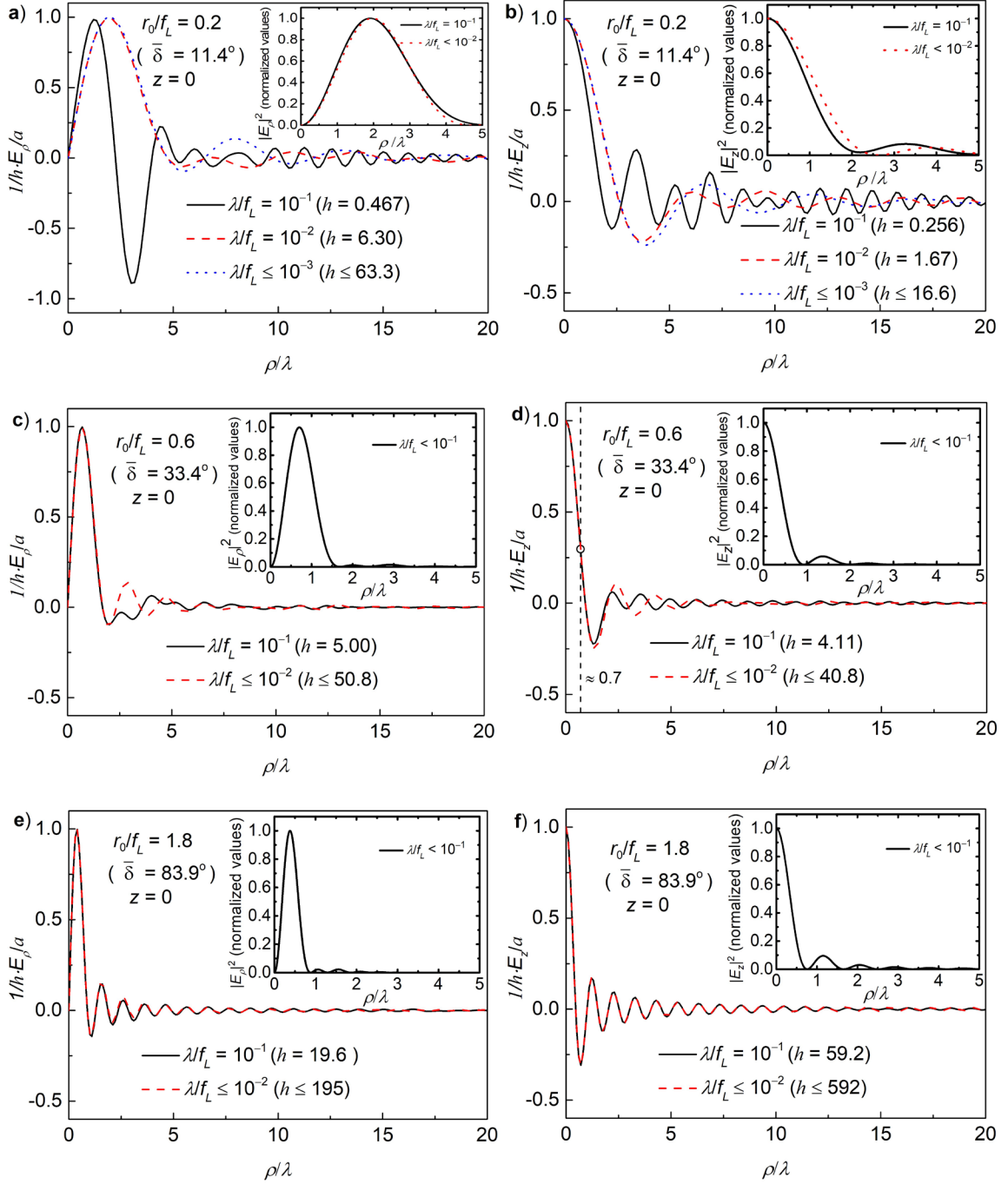Figure 4.6. The transversal distribution of the radial (a,c,e) and longitudinal (b,d,f) components of the electric field at $z = 0$ for various λ/f_L and r_0/f_L parameter values. The insets show the corresponding $|E|^2$ distribution. Please note that the vertical scale range for (a) differs from the ones of (b-f) [111].

43

The normalized distributions of the electric field components E_ρ and E_z are plotted against the radial coordinate, which has been normalized by the wavelength, as shown in Fig. 4.6. This normalization of coordinates allows for plotting curves with different λ/f_L values on the same scale. Specifically, Figs. 4.6 a and b are associated with $r_0/f_L = 0.2$ ($\bar{\delta} = 11.4°$ angle), Figs. 4.6 c and d with $r_0/f_L = 0.6$ ($\bar{\delta} = 33.4°$ angle), and Figs. 4.6 e and f with $r_0/f_L = 1.8$ ($\bar{\delta} = 83.9°$ angle). All the curves presented in Fig. 4.6 are located in the focal plane at $z = 0$ and are normalized to 1. Notably, the figures include explanations that specify the field amplitude enhancement factors, denoted as h, in comparison to the amplitude of the incoming field, labeled as a. These details are crucial for understanding how the magnitude of the field components is influenced by scale with the r_0/f_L and λ/f_L parameters, thereby facilitating a comparative analysis of the E_ρ and E_z amplitudes across different focusing geometries.

The curves shown in Fig. 4.6 oscillate with decreasing amplitude. At the focal point, E_z gets maximum values, while E_ρ is consistently zero, as expected. When the r_0/f_L value is constant, it becomes difficult to practically distinguish between the curves of different wavelengths unless they exceed a certain threshold of λ/f_L. These similar curves are indicated by the "$\leq$" sign (see the labels). The threshold λ/f_L value increases with increasing r_0/f_L.

Based on the analysis of the enhancement factors (shown in brackets), it is clearly evident that, at a constant r_0/f_L, the field strength increases as the wavelength decreases. Detailed calculations show that below the threshold, it scales with λ^{-1}. When the wavelength is held constant, the field strength significantly increases as r_0/f_L ratio increases. When comparing the amplitudes of curves with the same λ/f_L in pairs of figures (Figs. 4.6 a and b), (Figs. 4.6 c and d), and (Figs. 4.6 e and f), it is evident that for a low value of r_0/f_L (as seen in Figs. 4.6 a and b), the E_ρ field component is larger than E_z, while for a large r_0/f_L (as seen in Figs. 4.6e and f), E_z is dominant, as expected. This analysis is particularly relevant for those planning particle acceleration applications. It is also observed in Fig. 4.6 that the first zero crossing value decreases with increasing r_0/f_L for both field components. The absolute value of squared field components is plotted in the

insets to make it easier to observe certain characteristics. The first maxima for the radial component and the first minima for both components shift to the left as increases r_0/f_L, although the degree of this shift decreases for larger r_0/f_L.

The design of a waveguide-based electron accelerator requires results similar to those shown in Fig. 4.6. When aiming to efficiently in-coupling into the waveguide through focusing, it is important to match the width (in ρ/λ) of the E_z distribution curve to the characteristic r_1/f_L value of the waveguide, where r_1 represents the core radius. For the optimized parameters ($r_1 = 380$ μm core radius, $d = 32$ μm dielectric thickness, 0.6 THz frequency) of a dielectric-coated metallic waveguide, r_1/f_L is approximately 0.7 [138]. Among the curves in Fig. 4.6, the best agreement can be found in Fig. 4.6 d. This suggests that $r_0/f_L \approx 0.6$, making it a suitable focusing geometry for in-coupling into the waveguide.
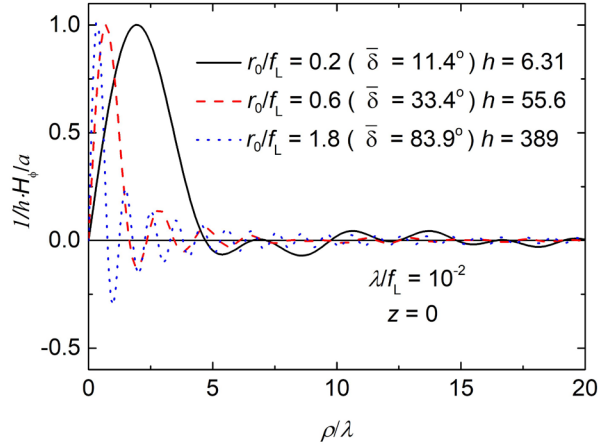
Figure 4.7. The transversal distribution of the azimuthal magnetic field at $z = 0$ for various r_0/f_L parameters for $\lambda/f_L = 10^{-2}$.

As mentioned above, the magnetic field has only azimuthal component. It can be determined by Eq. 4.25. The azimuthal magnetic field distribution with ρ/λ is shown in Fig. 4.7 for $z = 0$, $\lambda/f_L = 10^{-2}$ and for $r_0/f_L = 0.2$, 0.6 and 1.8 as also supposed in Figs. 4.6 a-f. The oscillation period decreases with increasing numerical aperture. The field enhancement factor, h obviously increases with the numerical aperture. For smaller NA ($r_0/f_L = 0.2$ and 0.6) h is close to the h values concerning the E_ρ (see Figs. 4.6 a and c),

while for large NA ($r_0/f_L = 1.8$) it is between the h values of E_ρ (see Fig. 4.6 e) and E_z (see Fig. 4.6 f).
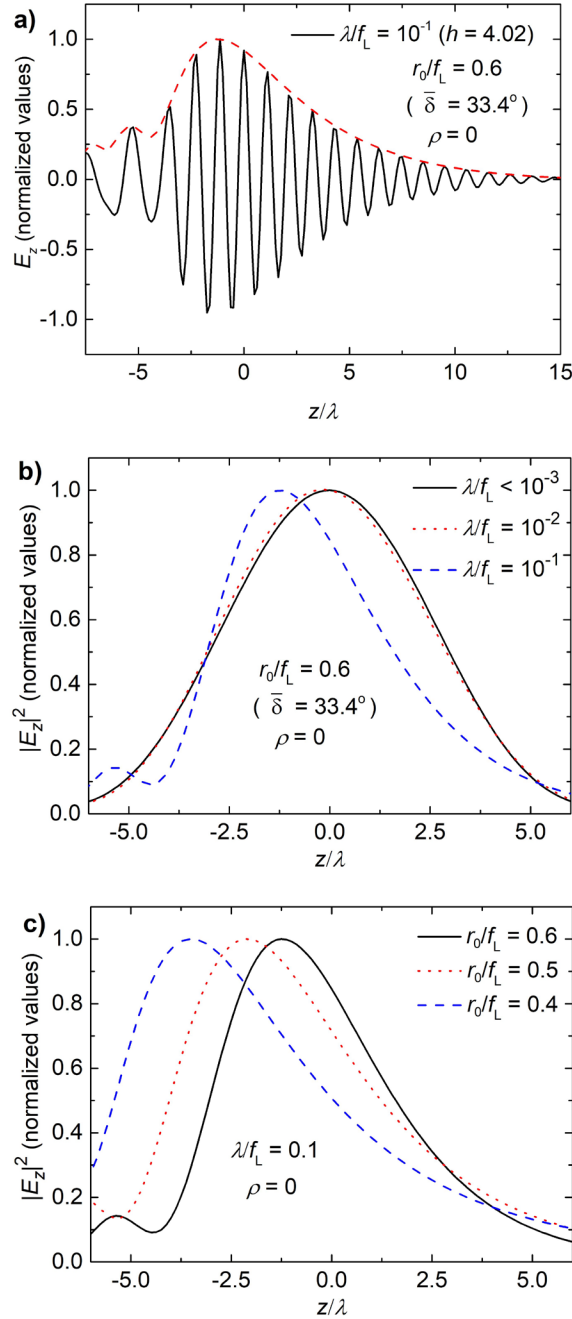
Figure 4.8. (a) The longitudinal distribution of the longitudinal component of the electric field at $\rho = 0$ for $r_0/f_L = 0.6$ and $\lambda/f_L = 0.1$ parameter values together with the absolute valued field. The corresponding $|E_z|^2$ distribution for, (b) a constant focusing angle ($r_0/f_L = 0.6$) for three different wavelengths (λ/f_L) and (c) a constant wavelength ($\lambda/f_L = 0.1$) for three different focusing angles (r_0/f_L).

For instance, to understand longitudinal distributions better, the E_z distribution along the optical axis was computed and plotted in the Fig. 4.8 a, considering $\lambda/f_L = 0.1$ and $r_0/f_L = 0.6$. The graph clearly indicates that the peak of the curve is shifted from the focus towards the apex of the mirror, as observed before in the case of linear polarization [103]. The relationship between λ/f_L and this shifting effect can be better studied using the $|E_z|^2$ curves, as seen in the Fig. 4.8 b. Below $\lambda/f_L = 10^{-2}$, this shift is insignificant, while for $\lambda/f_L = 10^{-1}$, the shift of the peak of the $|E_z|^2$ curve is approximately 1.2λ. The full width at half maximum (FWHM) of the $|E_z|^2$ curve is about 4.5λ for $\lambda/f_L = 10^{-1}$ and about 6λ for $\lambda/f_L \leq 10^{-2}$. Further examinations revealed that for a fixed λ/f_L, the shift is more pronounced for lower r_0/f_L values, as seen in the Fig. 4.8 c.

To further investigate this phenomenon, I expanded the calculations to include even smaller numerical apertures. The results for two different wavelengths are presented in the Fig. 4.9 a. The tendency is monotonous in the whole range. As the aperture size (relative to the focus) approaches zero, the location of the maximum amplitude converges to the vertex point. It is important to note that for extremely small apertures (when $r_0 \lesssim \lambda$, as indicated by the circled points), the contour term in the Stratton–Chu integral dominates the surface term. The Fig. 4.9 b. compares the curve representing the maximum of $|E_x|^2$ for a linearly polarized plane wave. The convincing similarity clears all doubt on the $r_0 = 0$ singularity of the radially polarized in the small numerical aperture regime.
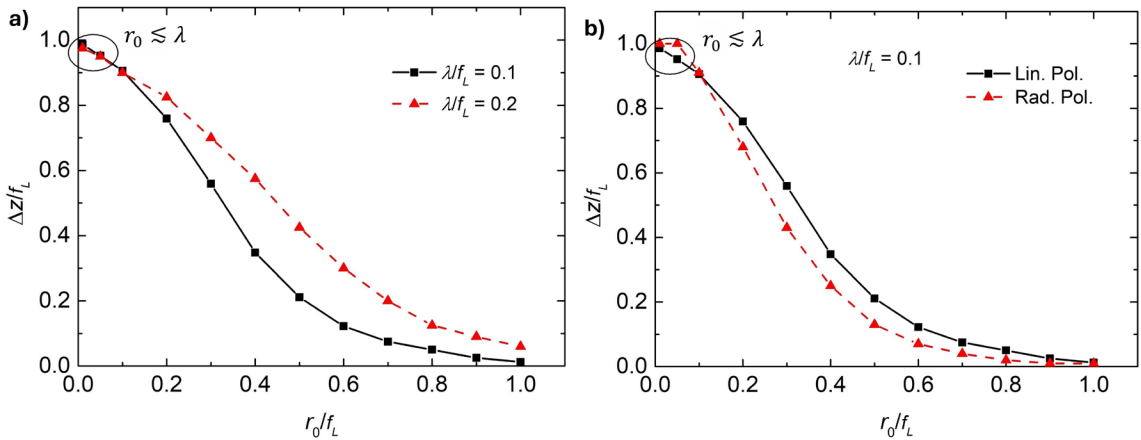
Figure 4.9. The shift of the high field point versus the aperture radius for the radially polarized (a) and linearly polarized plane wave (b). The axes are normalized by f_L.

4.6. Conclusion

This chapter presents derived formulae about electromagnetic field distributions when focusing radially polarized, monochromatic, flat-top beams using on-axis parabolic mirrors with perfect reflectance. The analytical calculations employed in this investigation were based on the well-known Stratton−Chu vector diffraction method. The method was effectively validated within a small NA and a negligible contour term, using the Rayleigh–Sommerfeld diffraction formula as a reliable alternative. Analysis of the transversal and longitudinal distribution of the radial and longitudinal electric field components was conducted under various focusing conditions. The implications of these results are significant in the area of THz techniques, like THz imaging and linear and nonlinear THz spectroscopy, particularly in particle acceleration applications, where intense longitudinal electric fields are essential. Although this investigation focused on monochromatic plane waves and connected paraboloid segments in on-axis geometry, there is potential for further development in electromagnetic pulses, various input beam types (e.g., vector Gaussian beam), and various types of parabola segment configurations (e.g., ring-like slice or off-axis geometry), as will be discussed in the following chapters.

5. Electromagnetic Field Distribution and Divergence-Dependence of a Radially Polarized Gaussian Vector Beam Focused by a Parabolic Mirror

5.1. Introduction

The focusing properties of radially polarized Gaussian beam with a high-NA objective has recently attracted many researchers because of a small spot size and a strong axial electric field components in focal region [113, 165]. Linearly polarized laser beams typically exhibit behavior consistent with the widely recognized Gaussian beam formula, which is derived from the paraxial wave equation governing the electric field [166, 167]. However, it is important to note that this is not the only solution attainable from Maxwell's equations through reasonable approximations. Kirk T. McDonalds has successfully deduced the formulae for a radially polarized *Gaussian Vector Beam*, also referred to as an Axicon Beam [114]. His approach relied upon the application of a paraxial approximation within the wave equation concerning the vector potential.

This chapter introduces derived formulae concerning the radial and axial electric fields, as well as the azimuthal magnetic field of a radially polarized Gaussian vector beam focused by a perfectly reflecting on-axis parabolic mirror with an arbitrary NA. The field properties at the focal point are analyzed, particularly for a case with a large numerical aperture. The potential use of a paraboloid ring as a practical tool for particle acceleration is considered, discussing its ability to generate a strong longitudinal field component. The model can manage divergent beams and address related issues. The variation in field distributions, including changes in the focal point and the field enhancement factor, in relation to the divergence angle is examined. The advantages of using THz wavelengths are highlighted, with specific examples provided. While the investigation is motivated by applications in particle acceleration, the acceleration mechanism itself is not discussed here. This chapter explains the second sub-study of the thesis, which is based on *my original scientific results* [160].

5.2. Vector Diffraction Field of Radially Polarized Gaussian Vector Beam by Parabolic Mirror

When considering a vectorial Gaussian incident beam as described by Eqs. (2.36) and (2.37), the electric and magnetic fields can be expressed using Cartesian components, while cylindrical arguments are:

$$\mathbf{E}_i(\rho, z) = [a(\rho, z, z_w) \cos \emptyset, a(\rho, z, z_w) \sin \emptyset, b(\rho, z, z_w)] \exp(-ikz),$$

$$\mathbf{H}_i(\rho, z) = [a(\rho, z, z_w) \cos \emptyset, -a(\rho, z, z_w) \sin \emptyset, 0] \exp(-ikz),$$

(5.1)

where in accordance with Eqs. (2.36) and (2.37)

$$a(\rho, z, z_w) = E_0 \frac{\rho}{w_0} [f(z - z_w)]^2 \exp\left(-f(z - z_w)\frac{\rho^2}{w_0^2}\right),$$

$$b(\rho, z, z_w) = i\theta_0 E_0 [f(z - z_w)]^2 \left(1 - f(z - z_w)\frac{\rho^2}{w_0^2}\right) \exp\left(-f(z - z_w)\frac{\rho^2}{w_0^2}\right),$$

(5.2)

where the f function is defined in Eq. (2.26). The role of the z_w parameter is to shift the beam waist from $z = 0$ to $z = z_w$ (by replacing z with $z - z_w$ in the argument of f) according to the circumstances in Subsection 5.3.2.

Due to the cylindrical symmetry of the illumination, a and b along the surface, S can be only considered as a function of the θ_s coordinate (see Fig. 4.1) and the z_w parameter as:

$$a(\theta_s, z_w) = E_0 \frac{\rho_s(\theta_s)}{w_0} \{f[z_s(\theta_s) - z_w]\}^2 \exp\left\{-f[z_s(\theta_s) - z_w]\left[\frac{\rho_s(\theta_s)}{w_0}\right]^2\right\},$$

$$b(\theta_s, z_w) = i\theta_0 E_0 \{f[z_s(\theta_s) - z_w]\}^2 \left\{1 - f[z_s(\theta_s) - z_w]\left[\frac{\rho_s(\theta_s)}{w_0}\right]^2\right\}$$

(5.3)

$$\times \exp\left\{-f[z_s(\theta_s) - z_w]\left[\frac{\rho_s(\theta_s)}{w_0}\right]^2\right\},$$

The integral expressions used to describe the electric and magnetic field distribution for focusing a radially polarized Gaussian vector beam were derived using the same mathematical procedure as the previous chapter [111]. By using Eqs. (4.9), (4.16) and (5.1) one can obtain

$$\mathbf{n} \times \mathbf{H}(S) = 2an_z \left[\cos \varnothing_s, \sin \varnothing_s, \cot \left(\frac{\theta_s}{2} \right) \right] \exp(-ikz_s),$$

$$\mathbf{n} \times \mathbf{E}(S) = 0, \tag{5.4}$$

$$\mathbf{n} \cdot \mathbf{E}(S) = 2n_z \left[b - a \cot \left(\frac{\theta_s}{2} \right) \right] \exp(-ikz_s)$$

Taking into consideration Eqs. (4.6), (4.12), (4.15) and (5.4), and by symmetry considerations the surface term of the complex electric field in Eq. (4.10) is:

$$
\mathbf{E}_S(\rho, z) = \frac{\exp(2ikf_L)}{2\pi} ik \int_\delta^\pi \int_0^{2\pi} d\theta_s \, d\varnothing_s \frac{\exp[ik(u - r_s)]}{u} r_s^2 \sin \theta_s
$$

$$
\times \left\{ \left[a \cos \varnothing_s + \left(b - a \cot \left(\frac{\theta_s}{2} \right) \right) \left(1 - \frac{1}{iku} \right) \frac{\Delta x}{u} \right] \mathbf{e}_\rho \right. \tag{5.5}
$$

$$
\left. + \left[a \cot \left(\frac{\theta_s}{2} \right) + \left(b - a \cot \left(\frac{\theta_s}{2} \right) \right) \left(1 - \frac{1}{iku} \right) \frac{\Delta z}{u} \right] \mathbf{e}_z \right\},
$$

where $\Delta x = r_s \sin \theta_s \cos \varnothing_s - \rho$, $\Delta y = r_s \sin \theta_s \sin \varnothing_s$, $\Delta z = r_s - 2f_L - z$ and $u = [\Delta x^2 + \Delta y^2 + \Delta z^2]^{1/2}$.

The dot product $\mathbf{H}(S) \cdot \mathbf{ds}$ with $\theta_s = \delta$ for the Gaussian vector beam is as follows:

$$\mathbf{H}(S) \cdot \mathbf{ds} = -4af_L \cot \left(\frac{\delta}{2} \right) \exp(-ikz_s) d\varnothing_s. \tag{5.6}$$

Substituting Eqs. (4.15) and (5.6) into Eq. (4.10), the contour term of the complex electric field in Eq. (4.11) is:

$$
\mathbf{E}_C(\rho, z) = -\frac{f_L \exp(2ikf_L)}{\pi} \cot \left(\frac{\delta}{2} \right) \oint a \frac{\exp[ik(u - r_s(\delta))]}{u}
$$

$$
\times \left(1 - \frac{1}{iku} \right) \left(\frac{\Delta x}{u} \mathbf{e}_\rho + \frac{\Delta z}{u} \mathbf{e}_z \right) d\varnothing_s, \tag{5.7}
$$

with $\Delta x = r_s(\delta) \sin \delta \cos \varnothing_s - \rho$, $\Delta y = r_s(\delta) \sin \delta \sin \varnothing_s$, $\Delta z = r_s(\delta) - 2f_L - z$ and $u = [\Delta x^2 + \Delta y^2 + \Delta z^2]^{1/2}$. At the focus, $(\rho = z = 0)$ a fully analytical expression can be obtained for the contour term:

$$
\mathbf{E}_C(\rho, z) = -\frac{a(\delta, z_w)}{2} \exp(2ikf_L) \sin(2\delta) \left(1 - \frac{1 - \cos \delta}{iku} \right) \mathbf{e}_z. \tag{5.8}
$$

In situations where the contour term is dominant, this expression becomes especially valuable for determining the electric field at the focus. By using Eqs. (5.5) and (5.7), the total complex electric field can be expressed as follows:

$$\mathbf{E}(\rho, z) = \mathbf{E}_S(\rho, z) + \mathbf{E}_C(\rho, z). \tag{5.9}$$

Let us continue with the derivation of the complex magnetic field. By using Eqs. (4.9), (4.16) and (5.1) one can obtain

$$\mathbf{E}(S) \times \mathbf{n} = 0,$$
$$\mathbf{n} \cdot \mathbf{H}(S) = 0. \tag{5.10}$$

This means that two terms are zero in the surface integral. Combining Eqs. (4.7), (4.16) and (5.1) we arrive to

$$\mathbf{E}(S) \cdot d\mathbf{s} = 0 \tag{5.11}$$

resulting in zero contour terms. Substituting $\mathbf{n} \times \mathbf{H}(S)$ from Eq. (5.4) into Eq. (4.11) for the magnetic field having solely azimuthal component one obtains:

$$\mathbf{H}_S(\rho, z) = \frac{\exp(2ikf_L)}{2\pi} ik \int_\delta^\pi \int_0^{2\pi} d\theta_s \, d\emptyset_s \, a \frac{\exp[ik(u - r_s)]}{u} r_s^2 \sin\theta_s$$
$$\times \left(1 - \frac{1}{iku}\right) \left\{ \left[\cot\left(\frac{\theta_s}{2}\right) \frac{\Delta x}{u} - \cos\emptyset_s \frac{\Delta z}{u} \right] \mathbf{e}_\emptyset \right\} \tag{5.12}$$

where Δx, Δy, Δz and u are mentioned in Eq. (5.5). In the next Section, the electric and magnetic fields will be analyzed in the focal region based on the formulae derived in this Section.

It is important to note that in the following section and in Chapter 5, the curves will represent the absolute value of the fields (i.e., field amplitudes) instead of the real parts of the fields as discussed in Chapter 4. This is simply a plotting technique and will not affect the conclusions.

5.3. Analyses of the Electromagnetic Field in the Focal Region

In the discussion that follows, the parabolic mirror is treated as a segment of a paraboloid within the $\pi/3 < \theta_s < \pi$ region (see Fig. 5.1) as a practical approach. Like a previous chapter, for broader applicability, it is preferred to introduce the relative parameters λ/f_L and w_0/f_L. It is important to note that the effect of the λ/f_L ratio on the electric field

distributions has already been extensively discussed [111]. For the purpose of the following analysis, it is assumed that the range $\lambda/f_L < 0.1$. The range $\lambda/f_L > 0.1$ is of no practical interest.

5.3.1. Incident beam with negligible divergence

In most practical cases, the divergence of the incident beam on the focusing element can be considered negligible. This means the limit of $\theta_0 \to 0$ in Eq. (2.74), in other words, the Rayleigh range is much larger than the typical size of the parabolic mirror, i.e., $z/z_0 \to 0$ in the formulae. Accordingly, using $f(z) \approx 1$, and $w(z) \approx w_0$ approximations lead to

$$a(\rho, z) = a(\rho, z) = E_0 \frac{\rho}{w_0} \exp\left(-\frac{\rho^2}{w_0^2}\right),$$

(5.13)

$$b(\rho, z) = 0.$$

5.3.1.1. The fields at the focus

Let us consider a Gaussian vector beam with negligible divergence as described in Eqs. (2.36), (2.37) and (5.13) being incident on the parabolic mirror, as illustrated in Fig. 5.1 a. According to Eqs. (4.3) and (4.4), the relationship between w_0 and the parameter related to the beam size δ_0 (as shown in Fig. 5.1a) can be written as

$$\frac{w_0}{\sqrt{2}} = \frac{2f_L}{1 - \cos\delta_0} \sin\delta_0.$$

(5.14)

The P_a beam power selected by the parabolic mirror with its $r_a = r_s(\theta_s = 60^o) = 2\sqrt{3}f_L$ aperture radius relative to the total beam power P is depicted in Fig. 5.2 a versus the δ_0 angle.

Firstly, it is important to concentrate specifically on the fields at the focal point. At this point, the magnetic field is zero, and the electric field comprises only a z component. The electric field strength $|E_z|$ at the focus ($\rho = z = 0$) can be determined using Eqs. (5.5), (5.8), (5.9), and (5.13). According to the special selection of the paraboloid segment, the lower bound of the integration (concerning θ_s in Eq. (5.5)) was $\delta = \pi/3$. In Fig. 5.2 b $|E_z|$ is plotted versus the δ_0 parameter (related to the beam radius according to Eq. (5.14)). The

peak is normalized to 1, thereby obtaining a curve that is practically independent of λ/f_L (if $\lambda/f_L < 0.1$) [111].
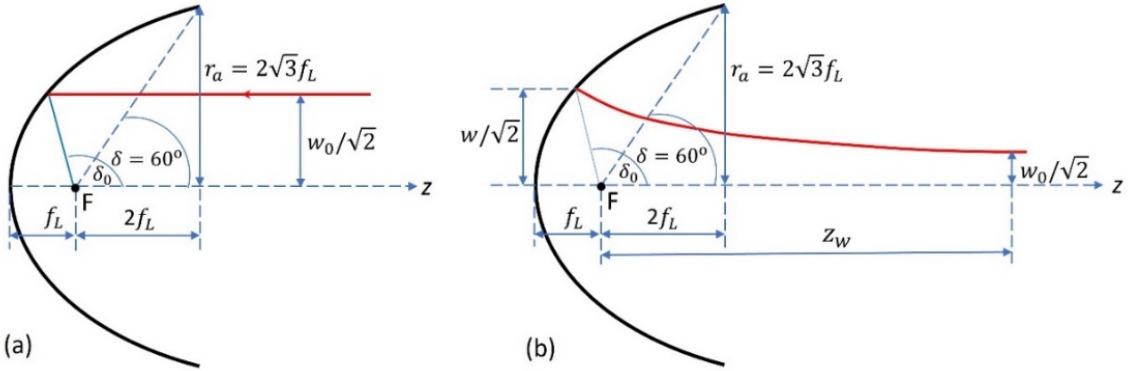
Figure 5.1. The geometry of the incidence on the parabolic mirror for a beam with negligible (a), and nonnegligible divergence (b) [160].

The peak belongs to $\delta_0 = 110°$ (see Fig. 5.2 a) with corresponding value of $w_0/f_L = 1.98$. In this case, 98.4% of the total beam power is transmitted through the aperture of the parabolic mirror (see the black square in Fig. 5.2 a). From a practical point of view, it is important to know how the focused field amplitude relates to the total beam power. Therefore, we introduced an average electric field E_f, which scales with the total beam power. E_f is fixed by the condition to get power equivalence between the Gaussian beam going to be focused and a fictive flat-top beam with uniform amplitude E_f and beam radius r_a [168], namely

$$\frac{1}{2} c \epsilon_0 E_f^2 r_a^2 \pi = 6\pi c \epsilon_0 E_f^2 f_L^2 = P\left(=\frac{1}{8} c \epsilon_0 \varepsilon_0^2 w_0^2 \pi\right). \tag{5.15}$$

The field enhancement factor relative to this fictive average field (used for characterization in the following) is defined as $h = |E_z|/E_f$. For the peak point of Fig. 5.1 a $h = 16.1 \cdot f_L/\lambda$ (if $\lambda/f_L < 0.1$) was found. This enhancement value is only $\sim$10% lower than the $h_{max} = E_{max}/E_f = \sqrt{32\pi} \cdot f_L/\lambda = 17.8 \cdot f_L/\lambda$ theoretical maximum obtained for ideal dipole wave in 4π focusing geometry [169]. It is obvious, that for a given f_L the shorter wavelength is preferable.
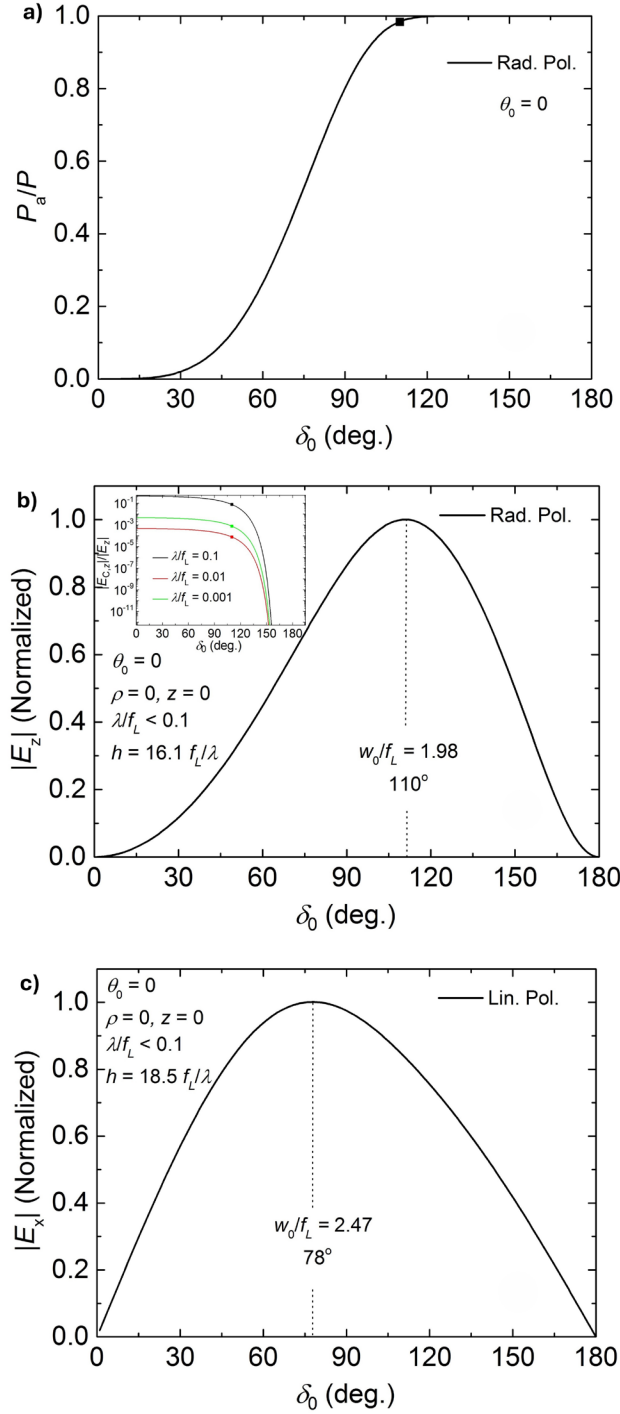
Figure 5.2. The beam power ratio falling into the aperture of the parabolic mirror (a). The longitudinal (b) and transversal (c) electric field amplitudes at the focus for radially (b) and linearly (c) polarized Gaussian beam versus the δ_0 focusing angle. The inset (b) shows the amplitude ratio of the contour term to the total field for $\lambda/f_L = 0.1$, 0.01 and 0.001. I draw attention for the logarithmic scale [160].

Supposing the focal length/wavelength ratio to be a typical value of 100 and 0.6 THz frequency (typically available with LiNbO₃ nonlinear crystals), the enhancement factor concerning the radial electric field was found to be 1610. This is close to the h value estimated by less sophisticated approximations under very similar geometrical circumstances [168]. This means that in the terahertz frequency range longitudinal electric field component as large as ~160 MV/cm is available, which is ideal for particle acceleration applications.

In many cases, depending on the focusing geometry and on the wavelength, the contribution of the contour integral term (Eq. (5.7)) is negligible compared to the surface term (Eq. (5.5)). In Fig. 5.2 b in the inset one can see the $|E_{C,z}|/|E_z|$ amplitude ratio of the contour term to the total field versus δ_0 for $\lambda/f_L = 0.1$, 0.01 and 0.001. It is seen that this ratio decreases with increasing δ_0. This behavior is understandable since the radius of the high-intensity part of the illustrated paraboloid decreases with δ_0 and consequently the field decreases along the contour. The particular case belonging to the peak (at $110°$) of the main curve of Fig. 5.2 b is shown by a square.

It is also informative and useful to make a comparison with the focusing of the linearly polarized Gaussian beam. Therefore, we determined $|E_x|$ at the focus ($\rho = z = 0$). In Fig. 5.2 c the normalized $|E_x|$ is plotted versus δ_0. Note that in this case the relationship between w_0 and δ_0 corresponding to Eq. (5.14) reads as:

$$w_0 = \frac{2f_L}{1 - \cos \delta_0} \sin \delta_0, \tag{5.16}$$

since for a linearly polarized beam w_0 is regarded as the characteristic size instead of $w_0/\sqrt{2}$ as mentioned above. The peak of the curve is reached at $\delta_0 = 78°$, with corresponding beam waist of $w_0/f_L = 2.47$. In this case, 98% of the total beam power is transmitted through the aperture of the parabolic mirror (which is very close to the above-mentioned value of 94.4% for the case of a radially polarized beam), hence providing a basis for making the comparison with the radially polarized beam. The field enhancement factor is $h = 18.5 \cdot f_L/\lambda$. This value just exceeds the corresponding h for the radial polarization also underlining the effectiveness of generating a longitudinal electric field.

56
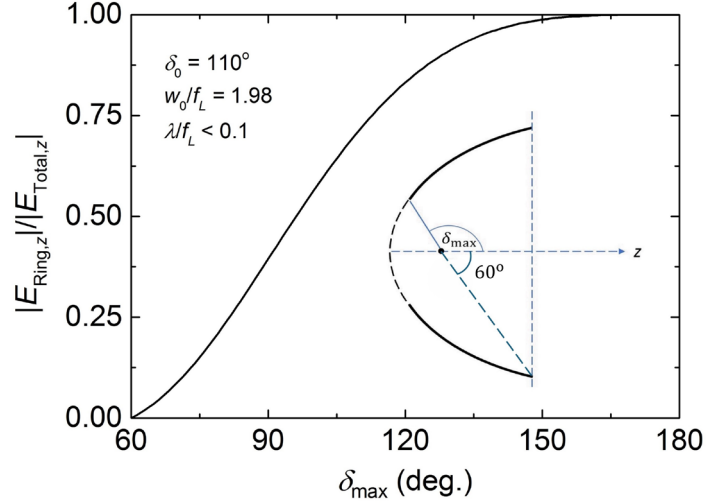
Figure 5.3. The amplitude of the longitudinal field component concerning the ring relative to the field amplitude achievable with the entire paraboloid (at the focus) versus δ_{max} (see the inset). The left edge of the curve corresponds to the thin ring, while its right edge is to the continuous paraboloid [160].

Let us return to the concept of radial polarization. When the peak point (belonging to the position of $\delta_0 = 110^o$ in Fig. 5.2 b) was calculated, the integration range in θ_s was encompassed from 60° to 180°. In a thought experiment considering, for example, the advantageous illumination geometry belonging to $\delta_0 = 110^o$ (with corresponding $w_0/f_L = 1.98$) let us keep the lower bound of the integration range at a value of 60°, but vary the upper bound, δ_{max} between 60° and 180°. Consequently, a ring-like paraboloid segment (as illustrated in the inset of Fig. 5.3) is obtained bounded by two contours (at 60° and δ_{max}, respectively). In Fig. 5.3 the amplitude of the longitudinal electric field at the focus concerning the ring relative to the field amplitude achievable with the entire ($60^o < \theta_s < 180^o$) paraboloid is plotted versus δ_{max}. During the calculations, this ring-like structure was taken into consideration by the difference of two contour terms (Eq. (5.7)). It is obvious from the graph, that – in this particular focusing geometry − the region of the paraboloid between 150° and 180° has practically no contribution to the total electric field. This result is important information for specialists dealing with the development of particle accelerators. The 'hole' on the paraboloid around its vertex does not detract from the available longitudinal electric field and might have a practical purpose

57

as well: it ensures unobstructed particle transfer. The details of the ring-like paraboloid setup are discussed in the following chapter [168].

5.3.1.2. The fields at the vicinity of the focus

In this particular section, the investigation focused on analyzing how the amplitude of the field components changes as distance from the focal point increases in the radial direction. The behavior of the radial (black line) and axial (red line) electric fields and the azimuthal magnetic field (green line) are plotted in Fig. 5.4. The horizontal scale is normalized with the wavelengths, and the peaks of all the curves are normalized to 1. Advantageously, by such normalization the curves do not change with the λ/f_L ratio in the $\lambda/f_L < 0.1$ range. The illumination parameters were again $\delta_0 = 110°$, $w_0/f_L = 1.98$.

As can be seen in Fig. 5.4, all field components oscillate with a decaying amplitude. The spatial oscillation period is somewhat shorter for $|H_\emptyset|$ than for $|E_\rho|$ leading to a continuous slight phase shift with the ρ distance. The position of the axial electric field amplitude maxima and the magnetic field minima (and vice versa) approximately coincide. Except for the first (for the axial electric field the first half) period, the period of the spatial oscillation approximately equals $\lambda/2$ as it is expected for a standing wave. Considering the enhancement factors, for the radial electric field component, $|E_\rho|$ it is the lowest ($h = 1.64 \cdot f_L/\lambda$), and for the axial electric field, $|E_z|$ it is the largest ($h = 16.1 \cdot f_L/\lambda$). For a typical value of $f_L/\lambda = 100$ (as also supposed in the example above) these enhancement factors are 164, 1610, and 1010 for $|E_\rho|$, $|E_z|$ and $|H_\emptyset|$, respectively. The $\int_0^\infty \left(|E_\rho|^2 + |E_z|^2 \right) \rho d\rho = \int_0^\infty |H_\emptyset|^2 \rho d\rho$ relation was verified numerically.

The amplitude ratio of the maximal axial, $|E_{z,\max}|$ to the maximal radial, $|E_{\rho,\max}|$ electric field component [79] is plotted versus the δ_0 focusing angle in Fig. 5.5. The curve belongs to the focal plane ($z = 0$). Note, that $|E_{z,\max}|$ is reached on the axis ($\rho = 0$), while $|E_{\rho,\max}|$ is reached at an off-axis ($\rho \neq 0$) point for any δ_0 (similarly, as it is seen in Fig. 5.4 for $\delta_0 = 110°$). As it is seen, the $|E_{z,\max}|/|E_{\rho,\max}|$ ratio has a maximum value of around 26

at δ_0 nearly 90°. The case belonging to Fig. 5.4 is indicated by a square symbol. The corresponding amplitude ratio is $h_z/h_\rho = 16.1 \cdot (f_L/\lambda)/1.64(f_L/\lambda) = 9.81$.
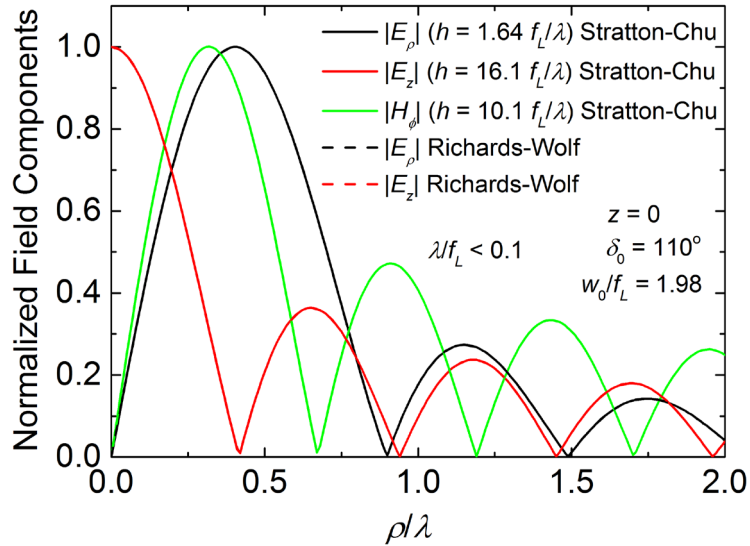
Figure 5.4. The radial electric (black line), the axial electric (red line), and the azimuthal magnetic (green line) field components versus the radial distance from the focus for $z = 0$. The horizontal scale is normalized by the wavelength, and the peaks of the curves are normalized to unity. The field enhancement factors, h is indicated in the graph. Note that the dashed curves used for validation fully coincide with the corresponding solid curves [160].
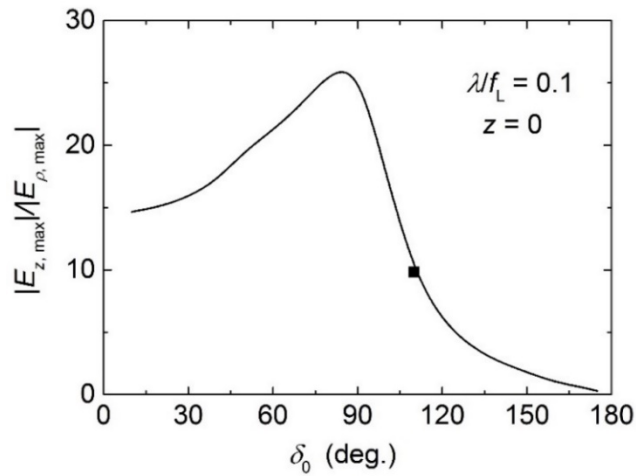
Figure 5.5. The amplitude ratio of the maximal axial to the maximal radial electric field component versus the focusing angle [160].

It was also examined how the fields vary in the z direction. For simplicity, this was examined only for the longitudinal electric field, for $\rho = 0$. $|E_z|$ normalized to 1 is plotted in Fig. 5.6. The horizontal scale is normalized by the wavelengths because of the reason mentioned above. The focusing parameters mentioned are the same as those for Fig. 5.4. The curve is symmetric to $z = 0$. It shows a quasi-oscillation nature with a spatial period more than twice that in the ρ direction for the given δ_0 (Fig. 5.4). For smaller δ_0 this ratio is larger.
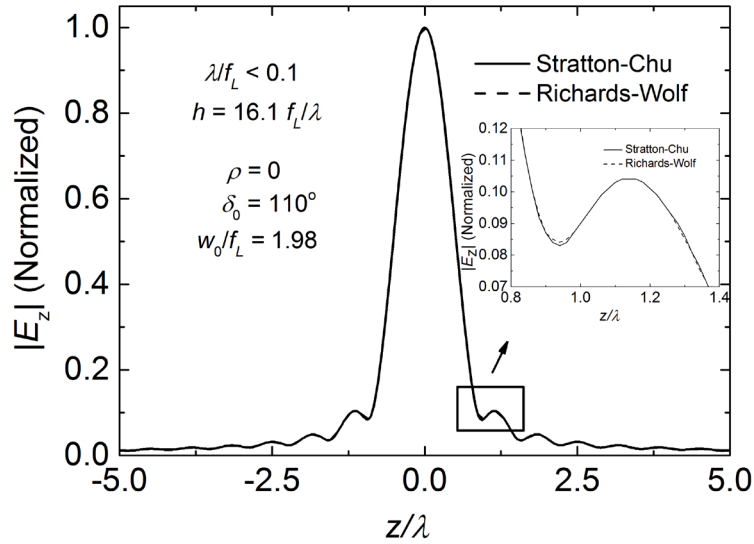
Figure 5.6. The amplitude of the longitudinal electric field component versus the longitudinal coordinate, z for $\rho = 0$. The horizontal scale is normalized by the wavelength, and the peaks of the curves are normalized to unity. The inset shows a magnified region of the main graph. The solid lines refer to our Stratton−Chu-based, while the dashed ones refer to the Richards−Wolf-based theory. Note that in the main part of the figure, the two types of lines fully coincide [160].

I have compared the results obtained from the derived electric field formulae based on the Stratton–Chu vector diffraction method with a method based on Richards−Wolf theory [80]. The curves were calculated using Eqs. 4 a and b of [80] are included in Figs. 5.4 and 5.6, as dashed lines, respectively. In both figures, the dashed curves from Richards–Wolf theory perfectly match the solid curves from Stratton–Chu theory. Any distinction between them can only be seen through magnification, as shown in the inset of Fig. 5.6, convincingly demonstrating the validity of the derivations. I have observed that the results

from the different theories (Stratton–Chu/Richards–Wolf) agree when the size of the illuminated area with high intensity is significantly larger than the wavelength. However, if the size of the high intensity illuminated area gets comparable to the wavelength a deviation appears between the curves obtained by the different theoretical concepts. For $\lambda/f_L = 0.1$ the deviation in the radial field distribution is well observable for $\delta_0 \gtrsim 175^o$ (Fig. 5.7 a), while in the longitudinal field distribution the deviation appears even for $\delta_0 \gtrsim 170^o$ (Fig. 5.7 b). Therefore, in such cases, the use of the formalism developed in this work is unavoidable.
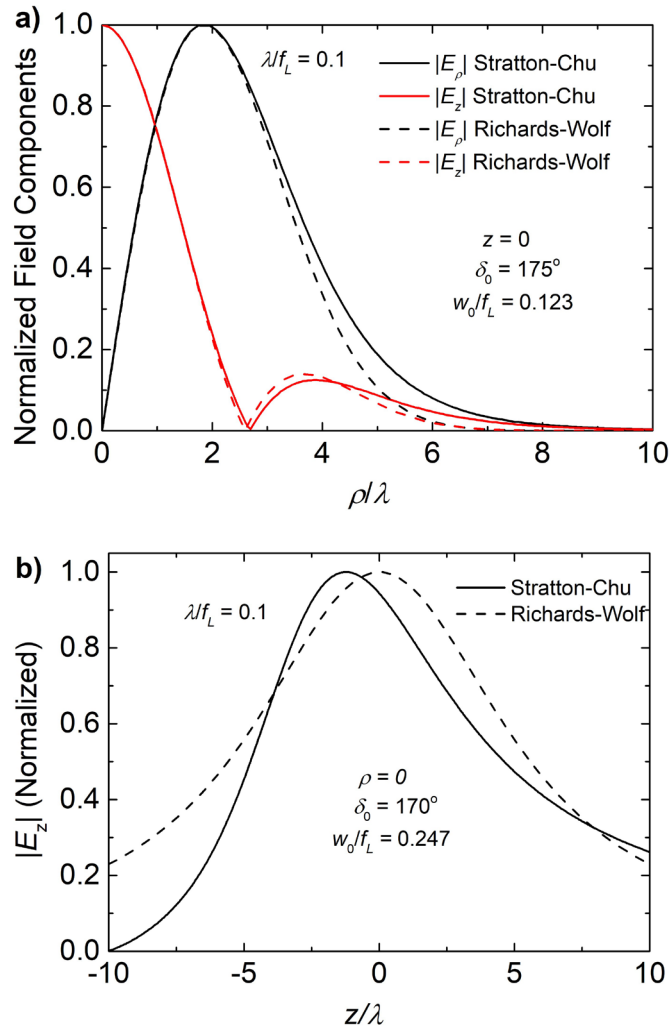
Figure 5.7. The normalized transversal (a) and longitudinal (b) distribution of the electric field components around the focus for $\lambda/f_L = 0.1$. The solid curves were computed by the Stratton−Chu based, and the dashed ones by the Richards−Wolf-based theory [160].

61

Certainly, the information provided by Figs. 5.4, 5.5 and 5.6 on the field characteristics and on the expansion of the high field region around the focus is interesting for specialists designing particle acceleration by tightly focused fields.

5.3.2. The effect of the beam divergence

The divergence of the incident beam, θ_0 which was neglected in the previous investigations, is considered to be a finite parameter in the following. At a given λ wavelength the θ_0 parameter determines the beam waist and the Rayleigh range in the following way:

$$w_0(\theta_0) = \frac{\lambda}{\pi\theta_0} \quad \text{and} \quad z_0(\theta_0) = \frac{\lambda}{\pi\theta_0^2}. \tag{5.17}$$

Let us suppose that the position of the beam waist of the incident beam with a given θ_0 divergence angle is at $z = z_w$ (Fig. 5.1 b). The relation between w and the δ_0 focusing angle (belonging to the $w/\sqrt{2}$ point on the paraboloid, as can be seen in Fig. 5.1 b) is:

$$\frac{w}{\sqrt{2}} = \frac{2f_L}{1 - \cos\delta_0} \sin\delta_0. \tag{5.18}$$

Hence, w as the function of δ_0 is:

$$w(\delta_0) = \frac{2\sqrt{2}f_L}{1 - \cos\delta_0} \sin\delta_0. \tag{5.19}$$

Using the relation

$$w(\delta_0) = w_0 \sqrt{1 + \left(\frac{z_w - r_s(\delta_0)\cos\delta_0}{z_0(\theta_0)}\right)^2} \tag{5.20}$$

together with Eq. (4.3) one obtains

$$z_w(\delta_0, \theta_0) = \frac{2f_L}{1 - \cos\delta_0}\sin\delta_0 + z_0(\theta_0)\sqrt{\left(\frac{w(\delta_0)}{w_0(\theta_0)}\right)^2 - 1}. \tag{5.21}$$

So, for given f_L and given θ_0 and δ_0 parameters the incident beam becomes known according to Eqs. (5.17) and (5.21).

It is straightforward to take into consideration the divergence of the incident beam during the calculations since the formulae concerning the a and b inputs (Eq. (5.3)) are well

prepared for this general case, where θ_0 is not negligible. Merely, Eq. (5.3) z_w has to be considered according to Eq. (5.17), and Eq. (5.21) has to be taken into consideration when w is expressed through w_0.

During the following investigation, the θ_0-dependence was studied only for the most interesting $|E_z|$ field. The θ_0 parameter was varied on the $0 < \theta_0 \leq 15^o$ range not exceeding the limit of validity of the theory due to the lack of terms proportional to $\mathcal{O}(\theta_0^2)$. Furthermore, occasionally the divergence of the THz beam originating from TPF sources falls in this range [170].
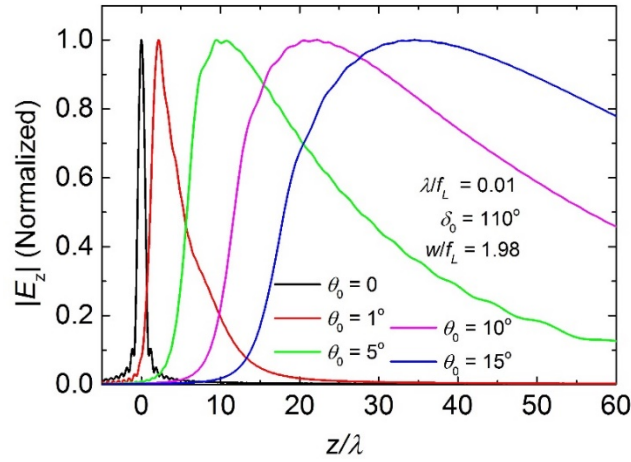
Figure 5.8. The amplitude of the longitudinal electric field component versus the longitudinal coordinate, z for $\rho = 0$, and different θ_0 values. The horizontal scale is normalized by the wavelength, the peaks are normalized to unity [160].

Contrary to the case of $\theta_0 = 0$, it is not informative enough to plot the field amplitude exactly at the focus since the presence of the divergence results in a shift of the field maxima as it will be seen. Therefore, the z-dependence of $|E_z|$ was computed and plotted in Fig. 5.8 for $\delta_0 = 110^o$ ($w/f_L = 1.98$) and $\lambda/f_L = 0.01$. As can be seen, if θ_0 differs from zero, the symmetry of the curve breaks. The width of the curves increases rapidly with increasing θ_0. Furthermore, the maxima shift monotonously towards the positive z direction as expected. This shift shows a quasi-linear dependence on θ_0 as can be seen in Fig. 5.9 (black line, left scale). The widening inevitably involves a decrease in the amplitude. The field enhancement factors (h) are plotted versus θ_0 in Fig. 5.9 (red line, right scale). They show a significant decrease with θ_0.

The radial distribution of $|E_z|$ was also determined at that specific z position, where the amplitude of the curve (at a given θ_0) had maxima. The normalized curves belonging to different θ_0 do not show so significant deviation from each other along the ρ radial direction (Fig. 5.10) as was observed for the z-dependence (Fig. 5.8). It is seen from the curves that the amplitudes of the side maxima relative to the main maxima increase with the divergence.
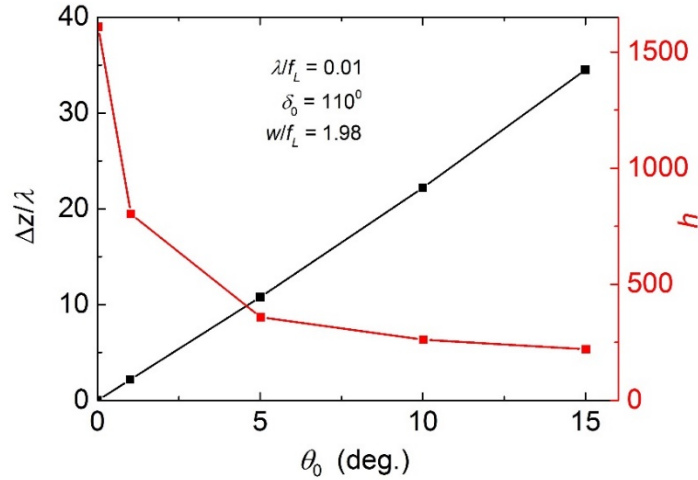
Figure 5.9. The shift of the peak position, Δz (normalized by the wavelength) (left scale, black line), and the field amplitude enhancement factor, h (right scale, red line) versus the divergence angle θ_0 [160].
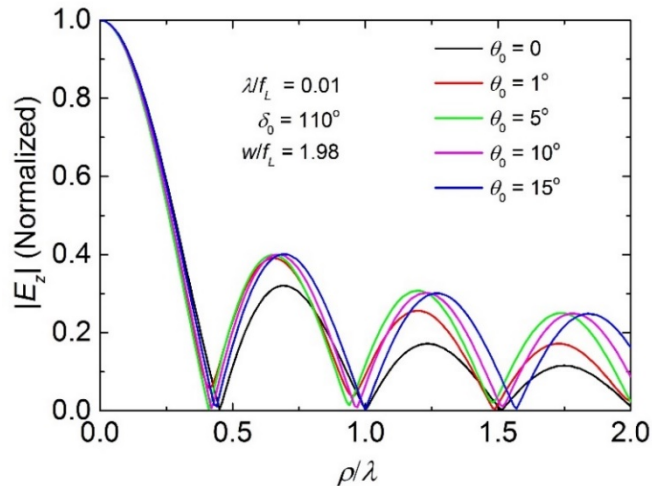
Figure 5.10. The amplitude of the longitudinal electric field component versus the radial distance from the focus. The horizontal scale is normalized by the wavelength, and the peaks of the curves are normalized to unity [160].

In this section, both the Gouy and the radial (related to the curvature) phase shifts were also treated correctly. The variation of these phases inside the mirror are plotted below for $\theta_0 = 0.1^0$ and $\theta_0 = 1^0$ divergences. Both the Gouy and the radial phase shift values are given in the units of kf_L (which is the phase shift of a plane wave between the focus and the vertex). As shown in Fig. 5.11, the effect of the Gouy phase shift is very small even for the smaller divergence angle (note that this phase shift is smaller for larger divergences).
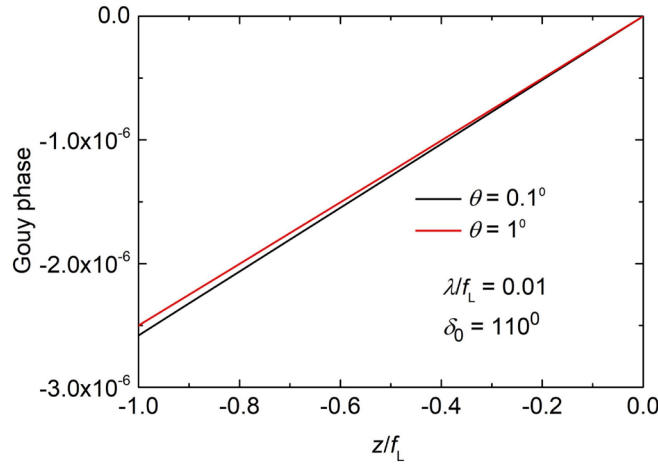
Figure 5.11. The Gouy phase shift versus the z position between the focus and the vertex.
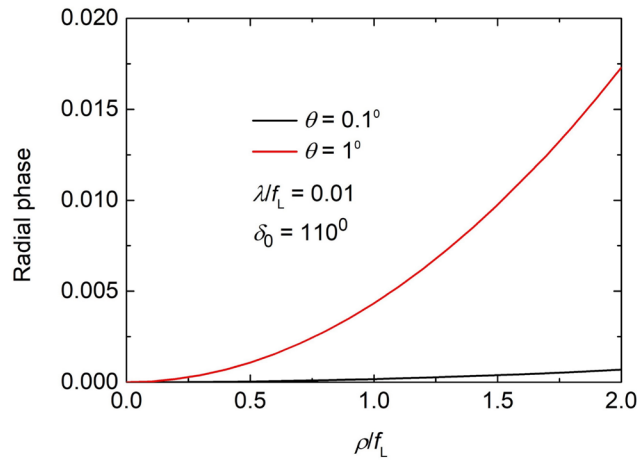
Figure 5.12. The radial phase shift versus the ρ radial position at $z = 0$.

The radial phase variation is significantly larger than the Gouy phase (Fig. 5.12). Additionally, increasing the divergence further increases this difference. It is evident that the radial phase is related to the radius of curvature, R. Given that the radius of curvature and phase values vary considerably across the entire range of divergences were examined

in this section, I have compiled these values in the following Table 5.1 instead of plotting them.

Table 5.1. The calculated values of beam parameters related to the curved phase front for different divergence angle.

ϑ_0 (deg)	R (m)	f_L/R	Rad. phase at $r = 2f_L$ (relative units)
0.1	145.213	3.44 1E-4	6.88 1E-4
1	5.7673	8.66 1E-3	0.0173
5	1.2049	0.0415	0.083
10	0.6374	0.0784	0.1569
15	0.4483	0.1115	0.2231

The dimensionless f_L/R value shown in the Table 5.1 is responsible to indicate whether the divergence of the beam arriving to the mirror is negligible during the focusing or not. If $f_L/R \to 0$ the beam can be considered as collimated. Practically, as shown in the Table 5.1, and the Fig. 5.12 if f_L/R is the order of 10^{-4} the effect is negligible, but at the order of $10^{-4} - 10^{-3}$ it becomes perceptible in spite of the small divergence angle. In the Fig. 5.13, the significance of considering/neglecting the radial phase factor is seen even for the low divergence angles. When the dashed curves were calculated, the radial phase was neglected. In conclusion the radial phase (curvature) has significance.
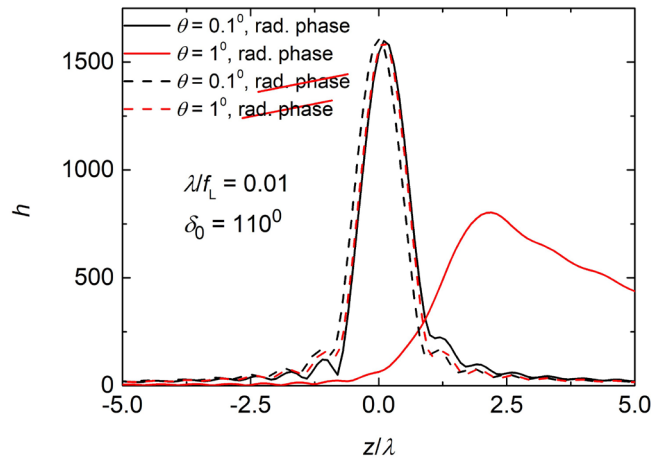
Figure 5.13. The field amplitude enhancement factor, h versus the longitudinal coordinate, z, normalized by the wavelength for two different divergence angles with and without radial phase factor.

5.4. Conclusion

This chapter presents derived formulae concerning the electric and magnetic fields obtained when focusing of radially polarized, monochromatic Gaussian vector beam with a parabolic mirror. Unlike plane waves with a uniform field distribution, these focused beams are rigorously derived from Maxwell's equations. The Stratton–Chu vector diffraction method provides a realistic picture of field distributions. A key finding is that the ring-like paraboloid segment is crucial for achieving strong longitudinal electric fields, making it particularly relevant for vacuum particle accelerator applications, which benefit from the unobstructed entrance and exit of particles. Therefore, it will be discussed in detail in the following chapter. For a typical focal length/wavelength ratio of 100, the enhancement factor for the radial electric field is 1610, indicating that longitudinal electric field components as large as ~160 MV/cm are available in the THz frequency range, marking an ideal condition for particle acceleration. Additionally, the investigation was shown that the physical focus is shifted relative to the geometrical focus along the symmetry axis for divergent beams. This shift is linearly proportional to the beam divergence. The effect of the divergence angle on the field enhancement factor was also studied. Furthermore, it was shown that the amplitudes of the side maxima relative to the main maxima in the radial field distribution increase with the divergence.

6. Generation of Extremely Strong Accelerating Electric Field by Focusing Radially Polarized THz Pulses with a Paraboloid Ring

6.1. Introduction

The focused THz pulses could be a potential solution for efficient particle acceleration [146]. Single-cycle THz pulses are promising because of their advantageous wavelength and the available peak electric field at the MV/cm level [37, 38, 54, 75]. It is important to carefully consider the shape of the electric field of the low-frequency THz pulses at the focus for the case of particle acceleration [141, 151]. The choice of the paraboloid mirror shape, whether annular or of arbitrary opening, can potentially impact the sharpness and dimensions of the focal spot. Consequently, a fully illuminated paraboloid having one contour is not the optimal focusing element if the goal is to achieve the maximal field component in the z direction for a fixed amount of input energy/beam power. Instead, a ring-like paraboloid segment to convert optimally the input radial THz field into axial component is proposed in this chapter. Thus, this chapter proposes a new setup and method for tightly focusing radially polarized THz pulses to generate a strong accelerating electric field suitable for vacuum electron acceleration. For this purpose, a suitable optical arrangement consisting of a reflaxicon and a ring-like segment of an on-axis parabolic mirror as a focusing element is introduced. The electric field distribution in the focal region is determined using the Stratton−Chu vector diffraction theory. Additionally, the characteristics of the pulse at the focus and the electric field distribution in the focal region are studied. The investigation is motivated by applications in particle acceleration, but the acceleration mechanism will be a future task, a simple calculation is performed. This chapter explains the third sub-study of the thesis, which is based on *my original scientific results* [168].

6.2. The Proposed Setup

The proposed focusing element is a ring-like slice of a paraboloid (referred to as 'ring' in the following), obtained by cutting the paraboloid with two parallel planes perpendicular to the z symmetry axis (Fig. 6.1). This is suggested as an alternative to the widely used on-

axis or off-axis parabolic mirror. The angles of view of the contours (intersections of the paraboloid and the planes), C_1, C_2 relative to the focus, F are δ_1 and δ_2. The missing ($\delta_2 < \theta_s < 180^o$) region, the 'hole', has practical purpose; it ensures the unobstructed exit of the accelerated electrons. The $2\gamma = \delta_2 - \delta_1$ range is chosen to be symmetric to the radial direction ($\theta_s = 90^o$). γ is regarded as an optimization parameter.
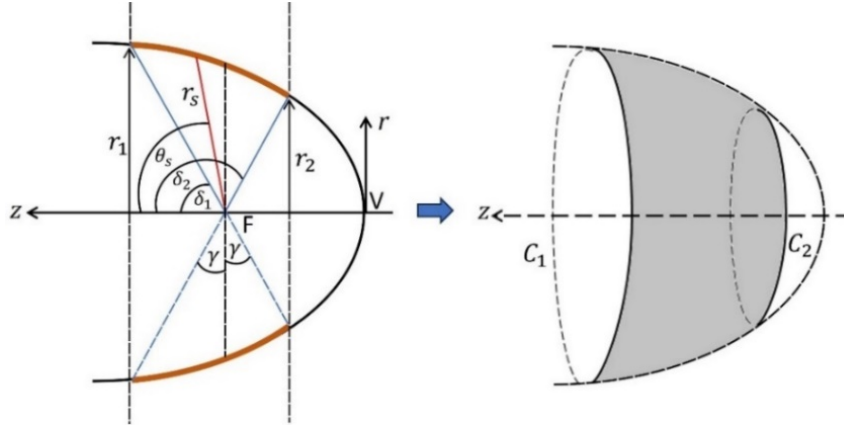
Figure 6.1. Schematic diagram of the paraboloid ring with notations [168].

To effectively use the pump beam power and prevent losses, as well as to achieve an interaction range free from blocking the incoming pulse, the illumination of the ring is solved through a reflaxicon [171-173]. It consists of a diverging (DM) and a converging (CM) conical mirror, as shown in Fig. 6.2. The DM and CM, with equal cone angles, are arranged coaxially; hence, the beam reflected from CM is parallel to the beam incident on DM. The segmented half-waveplate (SHWP in Fig. 6.2) is used to convert the linear pump polarization to radial polarization. The radially polarized THz beam is generated in the segmented nonlinear material (SNM in Fig. 6.2), which can be created, for example, from a semiconductor contact grating [34, 174], pumped by a CO_2 laser [38]. The incoming pump beam must not overlap with the beam reflected on CM. This requirement restricts the radii ratio to $r_2/r_1 > 0.5$ (Fig. 6.1), which means $\gamma < 20°$ (exactly 19.45^o). This restriction can be overcome when the reflaxicon is replaced by a transmissive axicon pair. In Fig. 6.3, the r_2/r_1 ratio is depicted versus γ in the $0 < \gamma < 20°$ range.
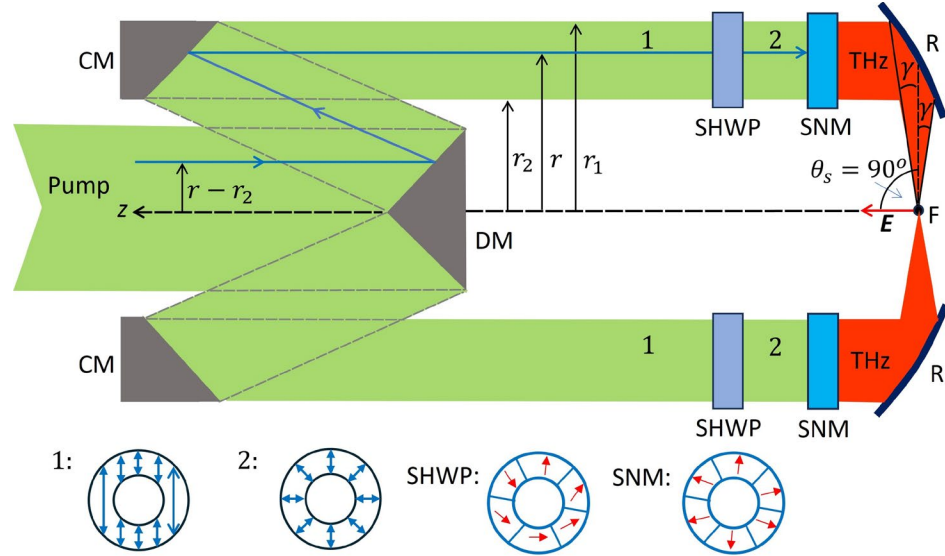
Figure 6.2. The layout of the proposed setup. DM: (conical) Diverging Mirror, CM: (conical) Converging Mirror, SHWP: Segmented Half-Waveplate, SNM: Segmented Nonlinear Material, R: (paraboloid) Ring, F: Focus. The pump polarization is linear (radial) in region 1 (2), as illustrated. The segmented structure of SHWP and SNM is illustrated on a front view, the optical axis of a segment is indicated by an arrow [168].
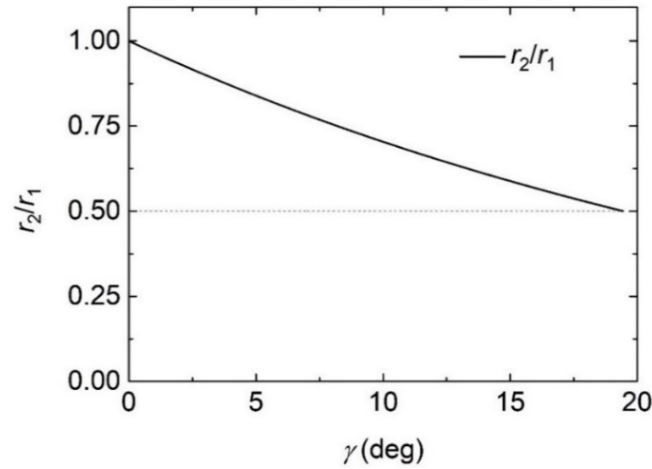
Figure 6.3. The r_2/r_1 ratio versus γ. For notations see Figs. 6.1 and 6.2 [168].

In order to determine the radial (r) electric filed distributions, an arbitrarily chosen ray in the pump beam (blue, thick ray in Fig. 6.2) can be considered. Upon reflection on CM and with its distance from the z axis denoted as r, it becomes clear that its distance from the axis is $r - r_2$ before reaching DM. The power has to be conserved, which is also true for the imagined thin-walled tube with $r - r_2$ radius and dr thickness, whose element is the

thick ray. This means $E_{P0}^2 2(r - r_2)\pi dr = E_P^2(r) 2r\pi dr$, where E_{P0} and $E_P(r)$ are the peak pump electric fields at the distances of $r - r_2$ and r from the z axis. Therefore, the r-dependence of the pump electric field is represented as:

$$E_P[r(\theta_s)] = E_{P0}\sqrt{1 - \frac{r_2}{r}} = E_{P0}\sqrt{1 - \frac{r_2}{r_s(\theta_s)\sin\theta_s}} \tag{6.1}$$

where $r_s(\theta_s) = \frac{2f_L}{1-\cos\theta_s}$ (see Eq. (4.3) and Fig. 6.1).

It is assumed that the incoming pump beam has an intensity independent of the distance from the z-axis (i.e., a flat-top beam, which is usually approximated by the beam of a large energy laser). Contrary to the effect, in the previous chapter I rigorously determined the vectorial Gaussian beam with simplicity as well and this kind of flat-top beam (e.g., CO_2 laser) is experimentally available. Three different possible THz beam profiles are considered. THz generation is a second-order nonlinear optical process, with conversion efficiency proportional to the pump intensity in an ideal case. This means that the THz intensity is proportional to the square of the pump intensity, i.e., the THz electric field is proportional to the square of the pump electric field (given in Eq. (6.1) as the first (*nonlinear*) assumption. As a second (*uniform*) assumption, for simplicity, I assume that the THz electric field distribution is uniform. Thirdly (*linear* case), I suppose that the THz beam inherits the radial field strength distribution of the pump given in Eq. (6.1). In all of these cases, the r-dependence of the E THz electric field incident on R can be given in the form of

$$E[r(\theta_s)] = \beta_n\left(1 - \frac{r_2}{r}\right)^n = \beta_n\left(1 - \frac{r_2}{r_s\sin\theta_s}\right)^n, \tag{6.2}$$

where β_n is a constant. $n = 1$ corresponds to the *nonlinear*, $n = 0$ to the *uniform*, and $n = 1/2$ to the *linear* case.

6.3. Theoretical Considerations

The surface and contour terms of the complex electric field are given by the Eqs. (4.20) and (4.23), based the Stratton-Chu vector diffraction method for the electric field inside the paraboloid illuminated by a radially polarized, monochromatic flat-top beam [111]. To

adapt these equations for the setup proposed in Section 6.2 (Fig. 6.2), the following improvements have to be made. The electric field belonging to the ring can be regarded as the electric field belonging to a paraboloid, which is continuous in the $\delta_1 < \theta_s < 180°$ region, minus the electric field belonging to a paraboloid, which is continuous in the $\delta_2 < \theta_s < 180°$ region. Consequently, in the surface term of Eq. (4.10) the integration by θ_s has to be performed between δ_1 and δ_2. Furthermore, since the ring is bounded by two contours (C_1, C_2), instead of one contour term [111] as it appears in Eq. (4.22) the difference of two contour terms belonging to C_1 and C_2 appear as seen in Eq. (6.4). The scaling factor in the electric field due to the beam shaping with the reflaxicon also has to be taken into consideration according to Eq. (6.1). Therefore, the surface, and the contour terms for the complex electric field are:

$$\mathbf{E}_S(\mathrm{P}) = \mathbf{E}_S(\rho, z) = \beta_n \frac{\exp(2ikf_L)}{2\pi} ik \int_{\delta_1}^{\delta_2} \int_0^{2\pi} d\theta_s\, d\emptyset_s$$

$$\times \left(1 - \frac{r_2}{r_s(\theta_s)\sin\theta_s}\right)^n \frac{\exp[ik(u - r_s(\theta_s))]}{u} r_s{}^2 \sin\theta_s \qquad (6.3)$$

$$\times \left\{\left[\cos\emptyset_s - \cot\left(\frac{\theta_s}{2}\right)\left(1 - \frac{1}{iku}\right)\frac{\Delta x}{u}\right]\mathbf{e}_\rho + \cot\left(\frac{\theta_s}{2}\right)\left[1 - \left(1 - \frac{1}{iku}\right)\frac{\Delta z}{u}\right]\mathbf{e}_z\right\}$$

where $\Delta x = r_s(\theta_s)\sin\theta_s\cos\emptyset_s - \rho$, $\Delta y = r_s(\theta_s)\sin\theta_s\sin\emptyset_s$, $\Delta z = r_s(\theta_s)\cos\theta_s - z$ and $u = [\Delta x^2 + \Delta y^2 + \Delta z^2]^{1/2}$, and

$$\mathbf{E}_C(\mathrm{P}) = \mathbf{E}_C(\rho, z) = \frac{\beta_n f_L}{\pi} \exp(2ikf_L)\left[\cot\left(\frac{\delta_2}{2}\right)\left(1 - \frac{r_2}{r_s(\delta_2)\sin\delta_2}\right)^n\right.$$

$$\times \int_0^{2\pi} \frac{\exp[ik(u - r_s(\delta_2))]}{u}\left(1 - \frac{1}{iku}\right)\left(\frac{\Delta x}{u}\mathbf{e}_\rho + \frac{\Delta z}{u}\mathbf{e}_z\right)d\emptyset_s$$

$$\qquad (6.4)$$

$$- \cot\left(\frac{\delta_1}{2}\right)\left(1 - \frac{r_1}{r_s(\delta_1)\sin\delta_1}\right)^n \int_0^{2\pi} \frac{\exp[ik(u - r_s(\delta_1))]}{u}$$

$$\left.\times \left(1 - \frac{1}{iku}\right)\left(\frac{\Delta x}{u}\mathbf{e}_\rho + \frac{\Delta z}{u}\mathbf{e}_z\right)d\emptyset_s\right]$$

with $\Delta x = r_s(\delta)\sin\delta\cos\emptyset_s - \rho$, $\Delta y = r_s(\delta)\sin\delta\sin\emptyset_s$, $\Delta z = r_s(\delta)\cos\delta - z$ and $u = [\Delta x^2 + \Delta y^2 + \Delta z^2]^{1/2}$, where $\delta = \delta_1$ in the first, and $\delta = \delta_2$ in the second term.

The total complex electric field can be given as:

$$\mathbf{E}(\rho, z) = \mathbf{E}_S(\rho, z) + \mathbf{E}_C(\rho, z). \qquad (6.5)$$

For $\lambda/f_L \ll 1$ (as it is fulfilled in the following discussion) the contribution $\mathbf{E}_C$ can be neglected beside $\mathbf{E}_S$. Furthermore, in the case of uniform input field distribution ($n = 0$) if $r/f_L, z/f_L \ll 1$ also holds, the E_z field component (most important from the point of view of applications), it can be very well approximated by the integral equation:

$$E_z(\rho, z) = 2ikf_L\beta_0 \exp(2ikf_L) \int_{\delta_1}^{\delta_2} J_0(kr \sin \theta_s) \tag{6.6}$$
$$\times (1 + \cos \theta_s) \exp(-ikz \cos \theta_s) d\theta_s$$

and the distribution of E_ρ field component by

$$E_\rho(\rho, z) = 2ikf_L\beta_0 \exp(2ikf_L) \int_{\delta}^{\pi} J_1(kr \sin \theta_s) \tag{6.7}$$
$$\times \exp(-ikz \cos \theta_s) \cot\left(\frac{\theta_s}{2}\right) \cos \theta_s \, d\theta_s$$

where J_0 and J_1 are denote the zeroth and first order Bessel function of the first kind, respectively. β_0 is the amplitude at $z = 0$. This follows from Eq. (6.3) after the reasonable approximations corresponding to the above-mentioned circumstances. Especially at the focus ($r = z = 0$) for the ring (with $\delta_1 = 90^\circ - \gamma$ and $\delta_2 = 90^\circ + \gamma$) shown in Fig. 6.2 a fully analytical expression is obtained:

$$E_z(\mathrm{F}) = 4ikf_L\beta_0\gamma \exp(2ikf_L). \tag{6.8}$$

The $\exp(2ikf_L)$ factor is the phase relative to the phase of the incoming beam, which is considered to be zero at the focal plane.

6.4. Results and Discussion

Consider a pump beam with a flat-top intensity distribution is incident on DM (Fig. 6.2). The THz beam generated in the SNM is assumed to be monochromatic (Subsection 6.4.1). Furthermore, the investigation extends to single-cycle THz pulses (Subsection 6.4.2), which are of significant practical importance. The focal length of the paraboloid is $f_L = 50$ mm in all cases examined below.

6.4.1. Focusing of monochromatic radiation

The THz peak electric field $E(r)$ in the region before R (Fig. 6.2) is supposed to follow the radial field profile given in Eq. (6.2). The value of β_n can be determined from the $P = \frac{1}{2}\epsilon_0 c \int_{r_2}^{r_1} \beta_n^2 \left(1 - \frac{r_2}{r}\right)^{2n} 2\pi r\, dr$ condition, where P is the average THz beam power regarded to be constant. For the purpose of normalization, introducing the fictive E_0 electric field defined as $P = 2\pi\epsilon_0 c E_0^2 f_L^2$, namely making the THz beam power equal to the power of a beam with uniform E_0 electric field, and radius of $2f_L$. Here, $2f_L = \rho_s(90^\circ)$ represents the radius of the circle at the intersection between the paraboloid and a plane perpendicular to the z axis at the focus.
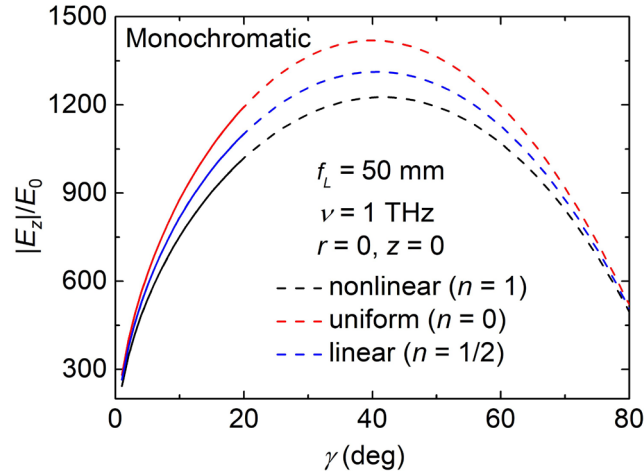
Figure 6.4. The z component of the electric field (in E_0 units) at the focus versus γ. The three curves belong to three different radial electric field distributions described by Eq. (6.2). The important parameters are indicated in the graph [168].

In the analysis, the frequency of $\nu = 1$ THz ($\lambda = 0.3$ mm, $T = 1$ ps) was considered. From the perspective of particle acceleration applications, the E_z axial (z) electric field component holds key importance; thus, it is examined in the following using the Eq. (6.3). It is determined first at the focus ($z = r = 0$) as the function of the γ, view angle of the ring, which was varied between 0 and 80°. The absolute value of E_z electric field relative to E_0 is plotted versus γ in Fig. 6.4. The three curves belong to the three different radial electric field profile: the nonlinear ($n = 1$), the uniform ($n = 0$) and the linear ($n = 1/2$). For $n = 0$ the curve obtained even more simply by the equation:

$$\frac{E_z}{E_0} = 2ikf_L\gamma\frac{\cos(\gamma)}{\sqrt{\sin(\gamma)}} \tag{6.9}$$

analytical expression following from Eq. (6.8) by normalization (as described at the beginning of this Subsection).

When using a reflaxicon for beam shaping, only setups corresponding to $\gamma < 20°$ (the continuous part of the curves) can be achieved. However, when using a diverging and converging transmissive axicon pair, setups corresponding to any γ can be realized. All three curves reach their maxima at nearly the same position. The curve belonging to the linear field profile ($n = 1/2$, which is regarded as the most realistic case) is very close to the average of the other two ($n = 1, n = 0$) curves. The largest difference between the three curves can be observed around their peaks (at $\gamma \approx 40°$), but even at that point the relative deviation of the two extreme ($n = 1, n = 0$) curves from the average is only $\sim7\%$. The curve of the "linear" distribution ($n = 1/2$) reach $\sim84\%$ of its peak value at the edge of the applicability range of the reflaxicon ($\gamma = 20°$). The other two curves behave similarly.

It was also determined how the electric field varies with the distance from the focus. In Fig. 6.5 a, $|E_z(r)|/E_0$ is plotted at the focal plane ($z = 0$) for $\gamma = 20°$ for a "linear" input THz electric field profile. It was noticed that, for different input THz beam profiles ($n = 0, 1/2$ and 1) the $|E_z(r)|/|E_z(0)|$ normalized curves were fully identical with each other, independently of n, and a decaying oscillation was also observed. Apart from the first period, the distances between the minima fall very close to $\lambda/2$ in coherence with the interference phenomenon. I mention here that the minima points are slightly moved away from each other when γ is increased, Eq. (6.6) can explain this behavior, since in the argument of J_0 the average value of the $\sin\theta_s$ decreases with increasing γ. It is also important to get information on axial distributions. $|E_z(r)|$ is plotted in Fig. 6.5 b for $r = 0$. The field-distribution is symmetric to $z = 0$. It shows a quasi-oscillation nature with a period of about 4-times larger than that of the curve in Fig. 6.5 a. The phase varies monotonously with z as it is seen in the right scale. The phase difference between the adjacent electric field minima points is π.
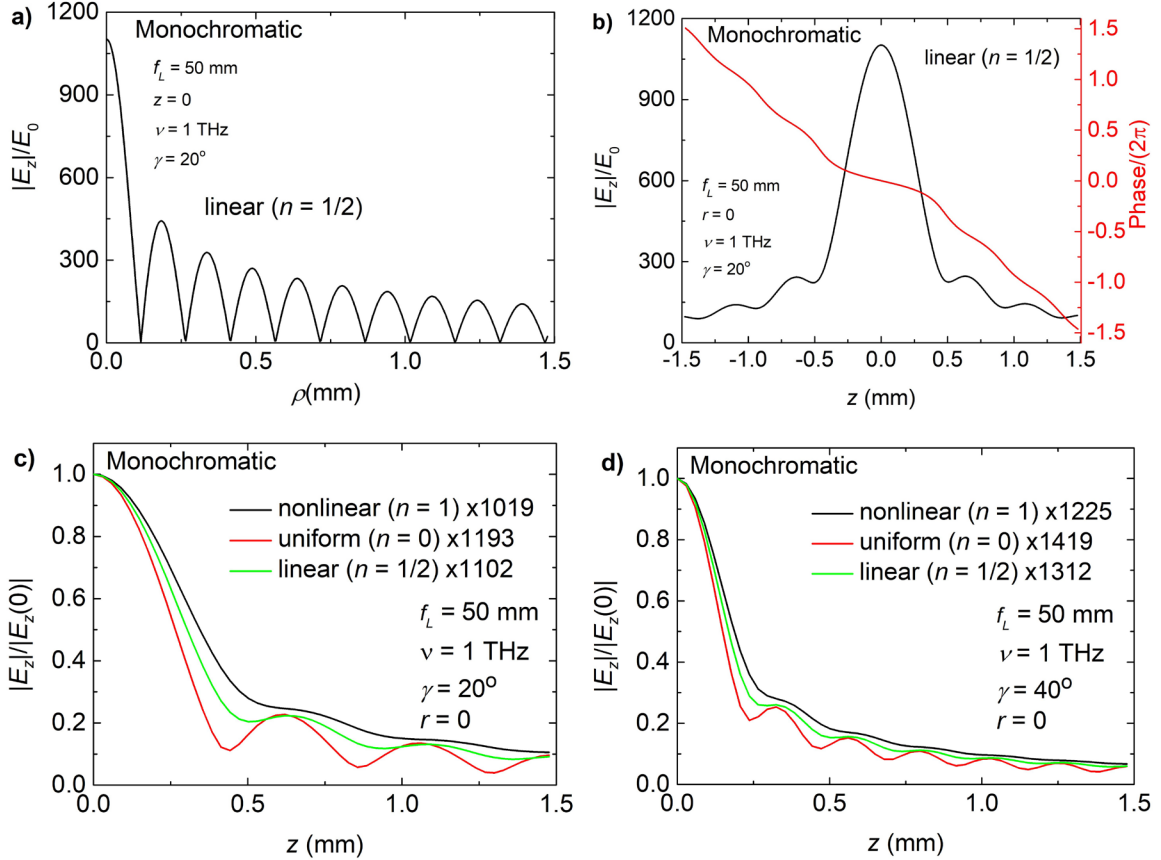
Figure 6.5. Radial distribution of the z electric field component at the focal region for $\gamma = 20^o$, $n = 1/2$ (a). Axial distribution of the z electric field component at the focal region for $\gamma = 20^o$, $n = 1/2$ (b). The phase is shown on the right scale. Axial distribution of the z electric field component at the focal region for $n = 0, 1/2$ and 1 for $\gamma = 20^o$ (c), and for $\gamma = 40^o$ (d). The important parameters are indicated in the graph [168].

In a similar manner to the radial distribution, the axial distribution for different input THz beam profiles ($n = 0, 1/2$ and 1) was determined and plotted in the $|E_z(z)|/|E_z(0)|$ normalized curves as a function of z in Fig. 6.5 c for $\gamma = 20^o$. Contrary to the behavior of the r-dependence (not shown), these curves differ from each other in their period, but the difference does not exceed $\pm 10\%$, unlike the radial distribution. The multiplication factors to obtain the $|E_z(z)|/E_0$ amplitude is indicated in Fig. 6.5 c. The z-distributions for $\gamma = 40^o$ (corresponding to the peak position in Fig. 6.4) were also determined and are shown in Fig. 6.5 d. Similarly to $\gamma = 20^o$, the curves of different n differ from each other in their period. Importantly, the periods are approximately half of the corresponding

76

periods of the curves with $\gamma = 20^\circ$, resulting in a less expanded high-field region in the z direction. The multiplication factors to obtain the $|E_z(z)|/E_0$ amplitude is indicated in Fig. 6.5 d, and they are larger than the corresponding factors in Fig. 6.5 c.

In Fig 6.5, the FWHM diameter of the high field region is approximately 150 μm in the radial direction, which is sufficiently large for electron acceleration applications. The expansion is about 600 μm (regarding the expansion in $-z$ direction as well) in the axial direction for a $\gamma = 20^\circ$, but for a $\gamma = 40^\circ$, it reduces by a factor of about 2. This shortening of the high-field region in the axial direction will also be observed in the case of single-cycle pulses discussed in the following Subsection. The subsequent Subsection demonstrates simple calculations that show the performance of single-cycle pulses, providing an advantage from the viewpoint of particle acceleration applications.

6.4.2. Focusing of THz Pulses

In this Subsection, instead of considering monochromatic waves, THz beam generated in the SNM is considered to be single cycle THz pulses. In the case of THz generation by phase-matched OR of ultrashort laser pulses the THz waveform is the derivative of the pump pulse envelope [175]. Accordingly, considering pump pulses with Gaussian temporal envelope, together with the 'linear'-type ($n = 1/2$) r-dependence the electric field of the THz pulse described in Eq. (2) also be expressed as:

$$E(r,t) = \frac{6}{r_1 - r_2}\left(\frac{3\varepsilon_P}{\pi\epsilon_0 c\tau}\right)^{\frac{1}{2}}\left(\frac{2}{\pi}\right)^{\frac{1}{4}}\left(1 - \frac{r_2}{r}\right)^{\frac{1}{2}}\frac{t}{\tau}\exp\left(-\frac{9t^2}{\tau^2}\right),\qquad(6.10)$$

where r_1 and r_2 are explained in Figs. 6.1 and 6.2. The waveform given in Eq. (6.10) reaches the $1/e$ value of its peak at instants $t = \pm\tau/2$ and satisfies the condition $\epsilon_0 c \int_{-\infty}^{\infty}\int_{r_2}^{r_1} E_0(r,t)^2 \, 2\pi r \, dr \, dt = \varepsilon_P$. The 'sine-like' input THz waveform given by Eq. (6.10) is depicted in Fig. 6.6 a by red solid curve beside the realistic parameters of $\tau = 1$ ps, $\varepsilon_P = 3$ mJ THz pulse energy and $r_1 = 14.1$ cm and $r_2 = r_1/2$ coming from the geometry ($f_L = 50$ mm, $\gamma = 20^\circ$ of the ring. The generation of THz pulses with similar parameters has been demonstrated [75, 78]. The spectra derived from Eq. (6.10) by Fourier transformation after averaging over r is:

$$e(\omega) = -\frac{i}{\sqrt{r_1^2 - r_2^2}}\left(\frac{3\varepsilon_P}{\epsilon_0 c\tau}\right)^{\frac{1}{2}}\left(\frac{2}{\pi}\right)^{\frac{1}{4}}\omega\tau^2\exp\left(-\frac{\omega^2\tau^2}{36}\right). \tag{6.11}$$

The inset displays the normalized spectral intensity density, which is proportional to $|e(\omega)|^2$, plotted against the frequency ν, with the spectral intensity curve reaching its peak at a frequency of $\nu_0 = 0.68$ THz. In the spectral domain, focusing is characterized through the $\mathcal{H}(\omega)$ transfer function, which is calculated directly from Eqs. (6.3) – (6.5). This transfer function allows for the determination of the THz waveform at the focal point as follow:

$$E_z(t) = \frac{1}{\pi}\int_0^\infty \mathcal{H}(\omega)e(\omega)\exp(i\omega t)\mathrm{d}\omega. \tag{6.12}$$

The output pulse has a 'cosine-like' shape (shown as a red solid curve in Fig. 6.6 b), when the input pulse has a 'sine-like' (red solid curve in Fig. 6.6 a). On the other hand, if the input pulse has a cosine-like shape (black dashed curve in Fig. 6.6 a), the output pulse takes on a sine-like shape (black dashed curve in Fig. 6.6 b) with an additional half cycle compared to the input pulse. These relationships between the input and the focused pulse shapes agree with the general consideration that the waveform at the focus is the temporal derivative of the input waveform [176]. When these curves are computed, also the $\tau = 1$ ps, $\varepsilon_P = 3$ mJ, $r_1 = 14.1$ cm and $r_2 = r_1/2$ parameter values were assumed. The input curves belong to the $r = r_1$ radial position, where the electric field reaches its maxima (Eq. (6.10)).
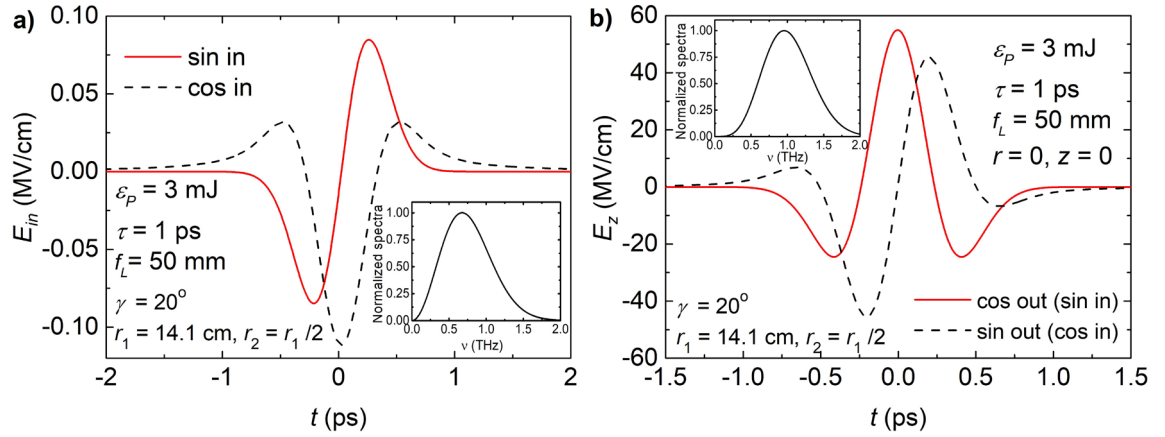
Figure 6.6. The THz waveforms in front of ring, R (a), and at the focal point (b). The input and output normalized spectral intensity densities are shown in the insets [168].

The sine-like input can be obtained directly from THz pulse sources based on OR. A 56 MV/cm field (as shown in Fig. 6.6 b) is present at the focus, with a corresponding field enhancement factor of 934 relative to the spatially averaged input field amplitude. This value is below the enhancement factor of 1101 as predicted for 1 THz frequency in Subsection 6.4.1. This can be explained by the fact that the spectral peak of the incoming pulse is at 0.68 THz (see the inset of Fig. 6.6 a), and the field enhancement is linearly proportional to the frequency. The focusing of the pulse results in the shift of the maximum of the spectra from 0.68 to 0.95 THz as shown in the insets (obviously such shift is not observed for the monochromatic wave). From the spectra shown in the inset of Fig. 6.6 b, the weighted average frequency determined as $\bar{v} = \int_0^\infty |e(v)|^2 \, v dv / \int_0^\infty |e(v)|^2 \, dv$ was found to be 1.02 THz. The reason of setting the frequency of the THz wave to 1 THz in Subsection 6.4.1 is to be close to this value.
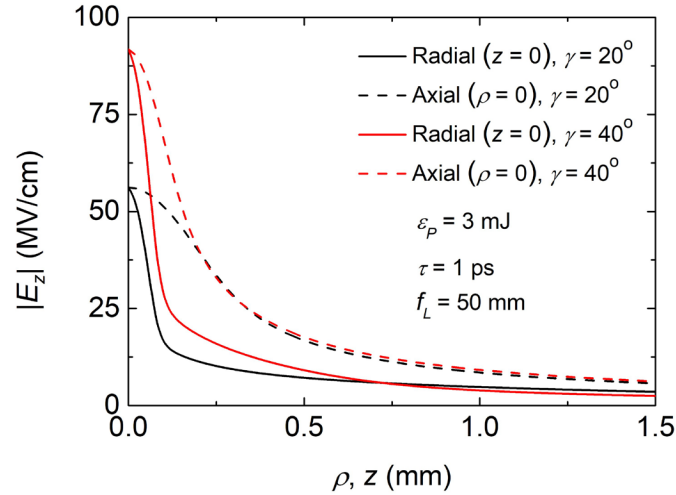
Figure 6.7. The radial (solid curves) and the axial (dashed curves) distribution of the accelerating electric field component at the focal region. The black color belongs to $\gamma = 20^o$, the red to $\gamma = 40^o$. The important parameters are indicated in the graph [168].

The radial and axial distributions of $|E_z|$ are plotted near the focus for $\gamma = 20^o$ and 40° as shown in Fig. 6.7. In contrast to the curves in the monochromatic case (Fig. 6.5 a and b), these curves do not show any oscillation due to the averaging of the oscillations related to the different components. The maximal fields, reached at the focus were 56 and 91 MV/cm, respectively for the two γ-s. All curves in Fig. 6.7 showed monotonous decay as away from the focus. In the radial direction the decay of the field is more rapid, and the FWHM

diameters are $\sim 150\ \mu$m for both γ, since this is influenced by the wavelength only. This FWHM diameter value advantageously exceeds the typical diameter of the particle beams. The axial extension reduces almost to its half (from FWHM of $\sim 600\ \mu$m to $\sim 300\ \mu$m) by changing from 20° to 40° in the γ. The $50 - 100$ MV/cm peak electric field value is ideal for electron acceleration applications. Peak electric field value close to 100 MV/cm could be reached by the superposition of four counter propagating THz beams as well, assuming the same input THz energy of 3 mJ but different frequencies [151]. The ring-based setup offers a perfectly cylindrical field distribution, which is a significant advantage compared to the four-beam setup.

A comprehensive investigation of the acceleration mechanism will be a future task. However, a simple calculation has been performed to provide an impression of the performance of the pulses described above for acceleration. The calculation determined the energy gained by an electron (traveling at a speed of $v \approx c$) during its interaction with the cosine-like pulse (illustrated in Fig. 6.6 b by the red solid curve) synchronized to the electron at $t \approx -0.25$ ps, $z = 0$ (zero crossing). Figure 6.8 shows the temporal variation of the axial electric field component for several z. It is obvious from the graph, the highest field point sweeps into the $+z$ direction with velocity of $v_s \approx 2.9c$ (Fig. 6.8 a). The expectation is that the energy gain will depend on the direction of relative motion (whether identical or opposite) between the electron and the movement of the field peaks. This hypothesis is confirmed by calculations, which show an energy gain of 0.28 MeV for identical motion and 0.23 MeV for opposite motion at $\gamma = 20^o$. At a $\gamma = 40^o$, the energy gains are 0.63 MeV for identical motion and 0.36 MeV for opposite motion. The significantly larger energy gain, 2.3 times for identical motion at the higher γ, cannot be solely attributed to the 1.63 times increase in the focal electric field (as shown in Fig. 6.7). The shorter expansion of the high-field region and the moderated sweeping velocity $v_s \approx 1.6c$ of the accelerating field also play crucial roles in enhancing acceleration efficiency (Fig. 6.8 b). It is obvious that beside the field enhancement, advantageously the sweeping velocity is reduced ($2.9c \rightarrow 1.6c$) by changing γ from 20^0 to 40^0.
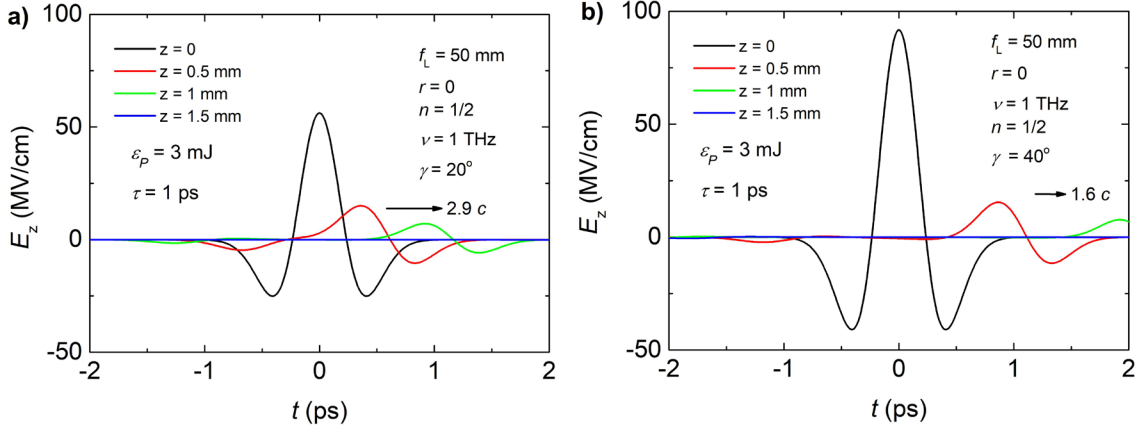
Figure 6.8. The accelerating pulse-forms for $\gamma = 20^0$ (a) and $\gamma = 40^0$ (b), respectively at several z values.

The sweeping velocity and the axial field distribution (Fig. 6.7) are together responsible for the formation of the field characteristics experienced by the electron. The zero crossing happens at a larger z for $\gamma = 40^0$ due to the slower sweeping velocity. As seen in the Fig. 6.9 the ratio of the negative/positive field amplitudes, but more importantly the negative/positive work ratio are more advantageous for the $\gamma = 40^0$ resulting more efficient net energy gain.
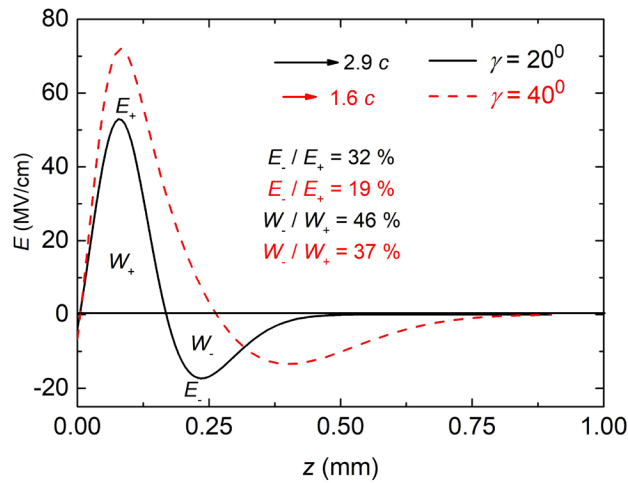
Figure 6.9. The axial field experience by the electron for $\gamma = 20^0$ (a) and $\gamma = 40^0$.

Interestingly, the energy gain values mentioned can be surpassed by approximately 13% using a sine-like accelerating field, which is less commonly applied. A more comprehensive study on acceleration is identified as a future task.

6.5. Conclusion

In this chapter, a focusing optical setup providing a strong axial electric field suitable for particle acceleration was designed and discussed. The setup was planned to be illuminated by a linearly polarized flat-top pump beam. Before generating THz radiation, a reflaxicon was proposed for beam shaping to avoid power loss. A segmented waveplate converts the linear polarization to radial, and the segmented nonlinear material generates the THz radiation with radial polarization. A ring-like segment of an on-axis parabolic mirror performed the tight focusing of the generated THz beam. The electric field was computed using the Stratton–Chu vector diffraction method. Easily applicable semi-analytical and purely analytical formulae applicable at the vicinity of the focus were also derived. Pulse characteristics in the focus, and electric field distribution in the focal region were studied. Supposing radially polarized 1 ps pulse duration of THz pulses with 3 mJ pulse energy and 50 mm focal length of parabolic ring, calculations predicted field enhancement above 1000 and accelerating electric field component exceeding 50 MV/cm - by slightly modifying the setup approaching 100 MV/cm - at the focus. Such focused pulses are well suited for particle acceleration applications.

7. Comparison of the Efficiency of Three-Focusing Geometry

This chapter examines and compares the field enhancement factor h in three different sub-studies, as previously discussed. A common key parameter for the characterization in the three sub-studies is the field enhancement factor, h, namely the ratio of the longitudinal electric field amplitude (at the focus) and the incident radial electric field amplitude. It is important to note that the geometry of the focusing has an impact on this parameter. When the whole paraboloid surface is illuminated, the focusing geometry is characterized by the focusing angle $\bar{\delta}$ (the complementary angle of δ, see Fig. 4.2) for uniform illumination, or $\bar{\delta}_0$ (the complementary angle of δ_0, see Fig. 5.1) for vectorial Gaussian incident beam.

For uniform illumination, the enhancement factor can be well approximated by the

$$h = 4\pi \frac{f_L}{\lambda} \left(\bar{\delta}_0 - \sin \bar{\delta}_0 \right) \tag{7.1}$$

simple analytical formula, which can be derived from Eq. (4.20) using reasonable approximations. For the Gaussian vector beam no simple analytical formula was found, Eq. (5.5) was used with reasonable neglections. Considering a practical sized parabolic mirror with solid angle of $2\pi/3$, and $f_L/\lambda = 10^2$ the enhancement factors were determined versus $\bar{\delta}$ and $\bar{\delta}_0$ as shown in Figs. 7.1 a and b for uniform illumination and for Gaussian vector beam, respectively. In both cases enhancement factors somewhat exceeding 1500 can be achieved, as shown by the squares.

For the setup containing the parabolic ring, the characteristic geometrical parameter is the illumination angle, γ as shown in Figs. 6.1 and 6.2. According to Eq. 6.8 the γ-dependent enhancement factor is:

$$h = 4\pi \frac{f_L}{\lambda} \gamma \frac{\cos \gamma}{\sqrt{\sin \gamma}}. \tag{7.2}$$

This was plotted in Fig. 7.2 for $f_L/\lambda = 10^2$. The maximum belongs to $\gamma = 40°$ shown by square. The square at $\gamma = 20°$ shows the limit of using a reflaxicon. For larger γ-s the setup can be realized by a transmission axicon pair only. Although the achievable enhancement is lower than with the entire parabolic mirror this setup is most appropriate for the realization of the particle acceleration.
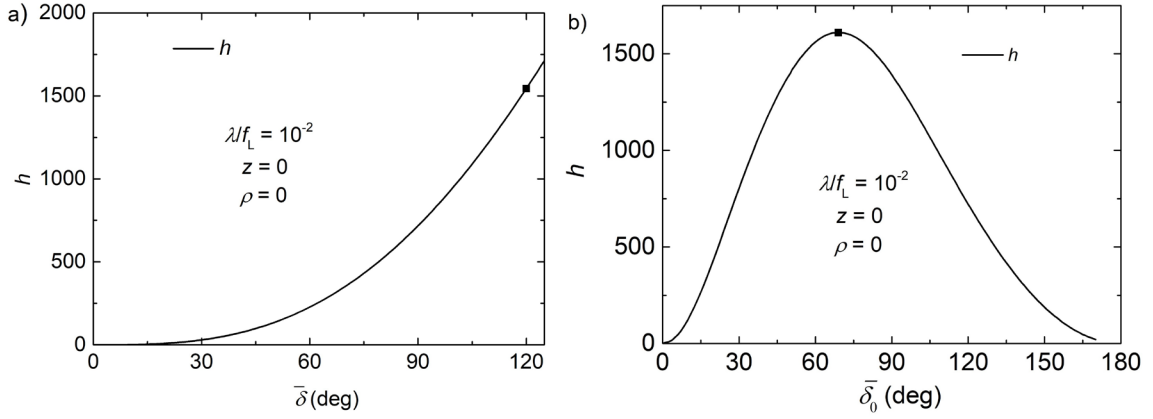
Figure 7.1. Field enhancement factor versus the focusing angles $\bar{\delta}$ (a) and $\bar{\delta}_0$ (b) for uniform illumination and for Gaussian vector beam, respectively. The angle of the parabolic mirror is $2\pi/3$, and $f_L/\lambda = 10^2$.
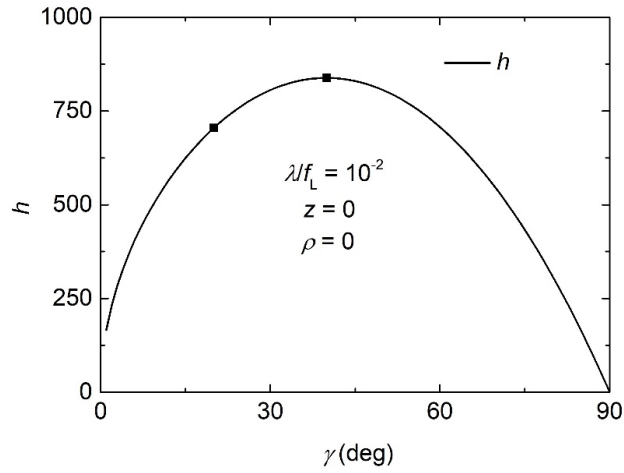

Figure 7.2. Field enhancement factor versus the illumination angle γ of a ring-like paraboloid for $f_L/\lambda = 10^2$.

8. Conclusions and Future Perspectives

8.1. Conclusions

The thesis examined the development of techniques for accelerating particles using tightly focused, radially polarized monochromatic laser beams and electromagnetic pulses. It emphasizes the need for high-NA parabolic mirrors to achieve strong longitudinal electric field components crucial for efficient particle acceleration. The thesis provides accurate electromagnetic field distribution models derived using the Stratton−Chu vector diffraction method, validated by comparison with other methods like Rayleigh−Sommerfeld and Richards−Wolf. It is particularly effective for systems with high-NA and long wavelengths. The thesis presents an analytical approach for calculating electric and magnetic field distributions when focusing radially polarized, monochromatic, flat-top and vector Gaussian beams using a perfectly reflecting on-axis parabolic mirrors. It verifies the importance of the longitudinal electric field component at high-NA for achieving the intense field strengths needed for particle acceleration. In case of radially polarized vector Gaussian beam, it examined the effects of beam divergence on axial and radial distributions of the longitudinal electric field component, showing that divergent beams shift the physical focus and influence the field enhancement factor. It was also observed that the shift of physical focus relative to the geometrical focus along the longitudinal direction exhibits a linear dependence on the divergence.

The thesis also introduces a novel setup for generating strong accelerating fields by focusing radially polarized THz pulses using a ring-like segment of a parabolic mirror. The designed setup consists of a reflaxicon for beam shaping to minimize power loss, a ring-like segment of an on-axis parabolic mirror for tightly focusing the radially polarized pulses, a SHWP for converting linear pump polarization to radial, and a SNM for generating the radially polarized THz beam. The field enhancement factor, which is the ratio of the longitudinal electric field strength to the input radial electric field component, significantly exceeds 1000. By focusing radially polarized 1 ps single-cycle THz pulses with 3 mJ pulse energy, calculations predicted accelerating electric field component in the order of 100 MV/cm, which is well suitable for particle acceleration. An energy gain on

the order of MeV by an electron moving at nearly the speed of light was obtained from the study of acceleration using a simple model. The thesis contributes significantly to particle acceleration by providing theoretical foundations and practical methodologies for generating strong accelerating fields using focused radially polarized electromagnetic pulses.

8.2. Future Perspectives

The thesis suggests several future research directions. This includes further optimizing the focusing setup and exploring different geometries to enhance field intensities. The thesis also recommends expanding and verifying the theoretical models used in this study through experimental setups to establish a solid foundation for future advancements in particle acceleration. Additionally, the detailed study of the acceleration mechanism will be a future task, which involves exploring the interaction between the pulses and particles in more depth, improving the design of the focusing setup, and potentially increasing the efficiency and effectiveness of the particle acceleration process. The implementation is planned in the frame of the TWAC project, which is funded by the EIC Pathfinder Open 2021 of the Horizon Europe program under grant agreement 101046504. The thesis also emphasizes the potential for extending the application of these findings to other areas requiring high-intensity THz pulses, such as imaging and spectroscopy.

9. Thesis Statements

1. Using the Stratton-Chu vector diffraction method, I derived formulae regarding the spatial distribution of the electric and magnetic field strength of radially polarized monochromatic laser beams focused with a parabolic mirror. The derivations were performed for both a flat-top input beam and a vector beam with a Gaussian intensity distribution. I derived relationships regarding the spatial distribution of the electric field components of a radially polarized beam focused by a system consisting of axicons and a parabolic mirror ring designed for accelerating charged particles. The transverse intensity distribution of the beam arriving at the parabolic mirror ring was considered in three different cases that were relevant from a practical point of view. All of my above-mentioned derivations are universal: they can be applied to any wavelength/focal length ratio and arbitrary NA. [S1,S2,S3]

2. In the cases mentioned in the first thesis point, I analyzed and interpreted in detail the spatial distribution of electric and magnetic field strength components in the vicinity of the focus – with particle acceleration applications in mind – with special attention on the longitudinal component of electric field strength. In each case, I determined the scale law for the longitudinal electric field strength in focus, the variables of which are the parameters of the input beam, the focal length and the characteristic parameter of the geometry of focusing. I looked for the optimal geometry for achieving maximum longitudinal field strength in each case. I showed that in the case of practical, optimized focusing, the ratio of the longitudinal electric field strength in focus to the input radial electric field component exceeds 1000. I showed that by optimized focusing of today's THz pulses with energy of the order of mJ, longitudinal electric field strength of the order of 100 MV/cm can be achieved, which is a remarkable fact from the point of view of particle acceleration applications. [S1,S2,S3]

3. The longitudinal and transverse distribution of the longitudinal component of the electric field of a radially polarized, monochromatic vector beam with a Gaussian intensity distribution focused with a parabolic mirror was investigated in the vicinity of the focus as a function of the divergence of the input beam. I showed that the real focus (the maximum location of the longitudinal field strength component) is shifted

relative to the geometric focus along the axis of symmetry of the beam. I showed that this shift is a linear function of the divergence of the input beam. I found that the maximum longitudinal electric field component value achievable by focusing is a monotonically decreasing function of the input beam divergence, and that this dependence is significant. Furthermore, I showed that in the transverse distribution of the longitudinal component of the electric field amplitude, the ratio of the sub maxima to the principal maximum value increases with the degree of beam divergence. [S2]

4. I applied a numerical code to simulate the post-acceleration of relativistic electrons with the longitudinal electric field of THz pulses focused with a parabolic mirror ring. According to the simulations, assuming a THz pulse energy of 3 mJ, a pulse length of 1 ps, and a parabolic mirror ring with a focal length of 5 cm illuminated at 20° and 40° viewing angles, electrons gain of 0.28 MeV/0.23 MeV (20°) and 0.63 MeV/0.36 MeV (40°) are available depending on whether the direction of motion of electrons moving at nearly the speed of light is the same/opposite to the direction of the electric field's sweeping velocity. [S3]

10.Összefoglaló

10.1. Absztrakt

A dolgozat radiálisan polarizált lézernyaláb parabolatükörrel (illetve parabola-gyűrűvel) történő fókuszálásának problémakörét tárgyalja különös tekintettel a THz-es frekvenciatartományú nyalábokra, impulzusokra. Az értekezés fő célkitűzése olyan optimális fókuszálási geometria megtalálása, ami kellő nagyságú longitudinális elektromos teret biztosít részecskegyorsítási alkalmazásokhoz. A lézer- és THz-es impulzusok részecskegyorsításra történő alkalmazásakor kulcsfontosságú a fókuszált nyaláb/impulzus elektromágneses terének pontos jellemzése főként a fókusz környezetében. A disszertáció a Stratton-Chu vektordiffrakciós módszert alkalmazza az elektromágneses térerősség eloszlásának pontos meghatározására különböző fókuszálási körülmények között. Az analitikus levezetések különböző bemenő nyalábprofilokra, köztük (homogén transzverzális intenzitáseloszlású) flat-top és Gaussian vektornyalábokra lettek elvégezve, nem csak „egyszeresen összefüggő" paraboloid tükörfelületre, hanem paraboloid-gyűrű esetére is, mely egy axikon-pár előtaggal kiegészítve a gyakorlatban is egyszerűen lehetővé teszi töltött részecskék (utó)gyorsítását. A részletes elemzések a longitudinális elektromos tér dominanciáját mutatták, ami a részecskegyorsítás szempontjából figyelemre méltó. A dolgozat részletesen vizsgálta a radiálisan polarizált, monokromatikus Gauss-vektornyaláb elektromos mezője longitudinális komponensének eloszlását a parabolatükör fókuszában. Vizsgálta többek között azt is, hogy a nyalábdivergencia hogyan befolyásolja a longitudinális elektromos tér longitudinális és radiális eloszlását. Az eredmények azt mutatták, hogy a nyalábdivergencia eltolja a fókuszt, és jelentős befolyással van a maximálisan elérhető longitudinális elektromos térre is. Az értekezésben megállapításra kerül, hogy a fizikai fókusz eltolódása a geometriai fókuszhoz képest a hosszirány mentén lineárisan függ a divergenciától. Optimalizált fókuszálás során a fókuszban kialakuló longitudinális elektromos térerősség és a bemenő radiális elektromos térkomponens aránya az 1000-et is meghaladja. A számítások azt is előrevetítették, hogy a radiálisan polarizált THz-es impulzusok fókuszálásának optimalizálásával az elektromos térkomponens elérheti a 100 MV⁄cm-es nagyságrendet, ami részecskegyorsításra kiválóan alkalmas. Numerikus szimulációk eredményei megalapozzák relativisztikus elektronok utólagos

gyorsításának lehetőségét THz-es impulzusok fókuszált longitudinális elektromos mezőjének felhasználásával. A szimulációk szerint 3 mJ terahertzes impulzusenergiát, 1 ps impulzushosszt és 20°, illetve 40°-os látószögben megvilágított, 50 mm-es fókusztávolságú parabola-gyűrűt feltételezve közel fénysebességgel mozgó elektronok 0,23/0,28 MeV (20°), illetve 0,36 MeV/0,63 MeV (40°) energianyereségre tehetnek szert attól függően, hogy mozgásirányuk az elektromos tér söprési sebességének irányával azonos/ellentétes.

10.2. Tézispontok

1. A Stratton-Chu vektor diffrakciós módszert alkalmazva összefüggéseket vezettem le parabolatükörrel fókuszált radiálisan polarizált monokromatikus lézernyaláb elektromos és mágneses térerősségének térbeli eloszlására vonatkozóan. A levezetéseket elvégeztem mind homogén intenzitáseloszlású (flat-top) bemenő nyaláb, mind Gauss-intenzitáseloszlású vektornyaláb esetére. Összefüggéseket vezettem le egy – töltött részecskék gyorsításához tervezett – axikonokból és parabolatükör-gyűrűből álló rendszerrel fókuszált radiálisan polarizált nyaláb elektromos térkomponenseinek a térbeli eloszlására vonatkozóan. A parabolatükör-gyűrűre érkező nyaláb transzverzális intenzitáseloszlására három különböző, gyakorlati szempontból releváns esetet tekintettem. Fent említett levezetéseim mindegyike általános érvényű: tetszőleges hullámhossz/fókusztávolság arány és tetszőleges numerikus apertúra esetén alkalmazható. [S1,S2,S3]

2. Az első tézispontban említett esetekben részletesen elemeztem és értelmeztem az elektromos és mágneses térerősség-komponensek térbeli eloszlását a fókusz környezetében – részecskegyorsítási alkalmazásokat szem előtt tartva – különös hangsúlyt szentelve az elektromos térerősség longitudinális komponensének. Valamennyi esetben meghatároztam a fókuszbeli longitudinális elektromos térerősségre vonatkozó skálatörvényt, melynek változói a bemenő nyaláb paraméterei, a fókusztávolság, illetve a fókuszálás geometriájára jellemző paraméter. Megkerestem a maximális longitudinális térerősség eléréséhez tartozó optimális geometriát az egyes esetekben. Megmutattam, hogy gyakorlatban is kivitelezhető, optimalizált fókuszálás esetén a fókuszbeli longitudinális elektromos térerősség és a bemenő radiális

elektromos térkomponens hányadosa meghaladja az 1000-t. Megmutattam, hogy a napjainkban hozzáférhető, mJ-os nagyságrendű energiájú terahertzes impulzusok optimalizált fókuszálásával 100 MV/cm nagyságrendű longitudinális elektromos térerősség érhető el, ami részecskegyorsítási alkalmazások szempontjából figyelemre méltó tény. [S1,S2,S3]

3. Parabolatükörrel fókuszált Gauss-intenzitáseloszlású, radiálisan polarizált, monokromatikus vektornyaláb elektromos tere longitudinális komponensének longitudinális és transzverzális eloszlását vizsgáltam a fókusz környezetében a bemenő nyaláb divergenciájának függvényében. Megmutattam, hogy a valódi fókusz (a longitudinális térerősség komponens maximumhelye) a nyaláb szimmetriatengelye mentén eltolódik a geometriai fókuszhoz képest. Megmutattam, hogy ezen eltolódás a bemenő nyaláb divergenciájának lineáris függvénye. Megállapítottam, hogy a fókuszálással elérhető maximális longitudinális elektromos térkomponens érték a bemenő nyaláb divergenciájának monoton csökkenő függvénye, és azt, hogy e függés jelentős. Megmutattam továbbá, hogy az elektromos téramplitúdó longitudinális komponensének transzverzális eloszlásában a mellékmaximum értékek főmaximum értékhez viszonyított aránya a nyalábdivergencia mértékével növekszik. [S2]

4. Numerikus kódot alkalmaztam relativisztikus elektronok parabolatükör-gyűrűvel lefókuszált terahertzes impulzusok longitudinális elektromos terével történő utógyorsításának modellezésére. Szimulációim szerint 3 mJ terahertzes impulzusenergiát, 1 ps impulzushosszt és 20 illetve 40°-os látószögben kivilágított 5 cm fókusztávolságú parabolatükör-gyűrűt feltételezve az elektronok 0,28 MeV/0,23 MeV (20°), illetve 0,63 MeV/0,36 MeV (40°) energianyereségre tesznek szert attól függően, hogy a közel fénysebességgel mozgó elektronok haladási iránya az elektromos tér söprésének irányával azonos/ellentétes. [S3]

List of Publications

Publications in the topic of thesis

[S1] **Z. T. Godana**, J. Hebling, and L. Pálfalvi, "Focusing of Radially Polarized Electromagnetic Waves by a Parabolic Mirror," in Photonics, vol. 10, no. 7: MDPI, p. 848, 2023. [111]

[S2] L. Pálfalvi, **Z. T. Godana**, and J. Hebling, "Electromagnetic Field Distribution and Divergence-Dependence of a Radially Polarized Gaussian Vector Beam Focused by a Parabolic Mirror," *arXiv preprint arXiv:2406.00795,* 2024. [160]

[S3] L. Pálfalvi, **Z. T. Godana**, G. Tóth, and J. Hebling, "Generation of extremely strong accelerating electric field by focusing radially polarized THz pulses with a paraboloid ring," Optics & Laser Technology, vol. 180, p. 111554, 2025. [168]

Conference contributions

[E1] **<u>Z. T. Godana</u>**, J. Hebling, and L. Pálfalvi, " Radially Polarized Electromagnetic Wave Focused by a Segment of a Parabolic Mirror," in Proceedings of the 6th International Conference on Optics, Photonics and Lasers (OPAL), 2023, pp64. (ISBN: 978-84-09-48335-8).

[E2] <u>L. Pálfalvi</u>, **Z. T. Godana**, G. Tóth, and J. Hebling, " Extremely High Electric Field for Electron Acceleration by Focusing of THz Pulses with Paraboloid Mirrors," in 10th Optical Terahertz Science and Technology (OTST), 2024, Paper WeA5.106.

[E3] L. Pálfalvi, **<u>Z. T. Godana</u>**, G. Tóth, and J. Hebling, " Production of Extremely Strong Accelerating Electric Field by Focusing THz Pulses with a Paraboloid Ring," in Conference on Lasers and Electro-Optics (CLEO), 2024: Optica Publishing Group, Paper JTu2A.63. (ISBN: 978-1-957171-39-5).

[E4] **<u>Zerihun Tadele Godana</u>**, László Pálfalvi, György Tóth and János Hebling, " Extremely Strong Longitudinal Electric Field by Focusing of Radially Polarized THz Pulses with a Paraboloid Ring," in Proceedings of the Doctoral Students' Conference for the Discussion of Optical Concepts (DoKDoK), 2024, Friedrich Schiller University Jena, Abbe School of Photonics, Germany, pp72.

Acknowledgments

I would like to express my heartfelt gratitude to my beloved wife, Firealem Yirga, my daughter, Yohana Zerihun, and my son, Biniyam Zerihun, for their unwavering love,

patience, understanding, and support throughout my PhD journey. I would also like to express my gratitude to my family, my wife's family, and friends, whose encouragement kept me focused and helped me overcome numerous challenges during my PhD journey. Lastly, I am thankful to Dilla University for their support during my PhD studies. Once again, I would like to express my heartfelt gratitude to everyone who has already been acknowledged and helped me complete this PhD thesis. Your assistance, encouragement, and invaluable contributions have been essential to my success.

References

[1]   Y.-S. Lee, *Principles of terahertz science and technology*. Springer Science & Business Media, 2009.

[2]   N. Sellers, *Handbook of Terahertz Technology*. Scientific e-Resources, 2018.

[3]   C. Yu, S. Fan, Y. Sun, and E. Pickwell-MacPherson, "The potential of terahertz imaging for cancer diagnosis: A review of investigations to date," *Quantitative imaging in medicine and surgery,* vol. 2, no. 1, p. 33, 2012.

[4]   I. Amenabar, F. Lopez, and A. Mendikute, "In introductory review to THz non-destructive testing of composite mater," *Journal of Infrared, Millimeter, and Terahertz Waves,* vol. 34, pp. 152-169, 2013.

[5]   L. Skvortsov, "Standoff detection of hidden explosives and cold and fire arms by terahertz time-domain spectroscopy and active spectral imaging," *Journal of Applied Spectroscopy,* vol. 81, no. 5, pp. 725-749, 2014.

[6]   E. V. Yakovlev, K. I. Zaytsev, I. N. Dolganova, and S. O. Yurchenko, "Non-destructive evaluation of polymer composite materials at the manufacturing stage using terahertz pulsed spectroscopy," *IEEE Transactions on Terahertz science and Technology,* vol. 5, no. 5, pp. 810-816, 2015.

[7]   J. Federici and L. Moeller, "Review of terahertz and subterahertz wireless communications," *Journal of Applied Physics,* vol. 107, no. 11, 2010.

[8]   P. Tan, J. Huang, K. Liu, Y. Xiong, and M. Fan, "Terahertz radiation sources based on free electron lasers and their applications," *Science China Information Sciences,* vol. 55, pp. 1-15, 2012.

[9]   L. Feigin, A. Gover, A. Friedman, A. Weinberg, D. Azar, and A. Nause, "High-Power Terahertz Free Electron Laser via Tapering-Enhanced Superradiance," *Electronics,* vol. 13, no. 7, p. 1171, 2024.

[10]   B. S. Williams, "Terahertz quantum-cascade lasers," *Nature photonics,* vol. 1, no. 9, pp. 517-525, 2007.

[11]   K. Fujita *et al.*, "Recent progress in terahertz difference-frequency quantum cascade laser sources," *Nanophotonics,* vol. 7, no. 11, pp. 1795-1817, 2018.

[12]   X. Ropagnol *et al.*, "Intense THz pulses with large ponderomotive potential generated from large aperture photoconductive antennas," *Optics express,* vol. 24, no. 11, pp. 11299-11311, 2016.

[13]   G. Lu, R. Zhao, H. Yin, Z. Xiao, and J. Zhang, "Study of the super directive THz photoconductivity antenna," *Plasmonics,* vol. 16, no. 3, pp. 677-685, 2021.

[14]   N. Nilforoushan *et al.*, "Efficient THz generation from low-temperature-grown GaAs photoconductive antennas driven by Yb-doped fiber amplifier at 200 kHz repetition rate," *Applied Physics Letters,* vol. 123, no. 24, 2023.

[15]   V. Andreeva *et al.*, "Ultrabroad terahertz spectrum generation from an air-based filament plasma," *Physical review letters,* vol. 116, no. 6, p. 063902, 2016.

[16] A. D. Koulouklidis *et al.*, "Observation of extremely efficient terahertz generation from mid-infrared two-color laser filaments," *Nature communications,* vol. 11, no. 1, p. 292, 2020.

[17] J. Buldt, H. Stark, M. Müller, C. Grebing, C. Jauregui, and J. Limpert, "Gas-plasma-based generation of broadband terahertz radiation with 640 mW average power," *Optics Letters,* vol. 46, no. 20, pp. 5256-5259, 2021.

[18] Z. Fan, C. Lu, and Y. Liu, "Tunable broadband THz emission from air plasma pumped by femtosecond pulses composed of a fundamental frequency with its detuned second harmonic," *Optics Communications,* vol. 505, p. 127532, 2022.

[19] T. Seifert *et al.*, "Ultrabroadband single-cycle terahertz pulses with peak fields of 300 kV cm− 1 from a metallic spintronic emitter," *Applied Physics Letters,* vol. 110, no. 25, 2017.

[20] E. T. Papaioannou and R. Beigang, "THz spintronic emitters: a review on achievements and future challenges," *Nanophotonics,* vol. 10, no. 4, pp. 1243-1257, 2021.

[21] M. Wang, Y. Zhang, L. Guo, M. Lv, P. Wang, and X. Wang, "Spintronics based terahertz sources," *Crystals,* vol. 12, no. 11, p. 1661, 2022.

[22] F. Blanchard *et al.*, "Generation of 1.5 µJ single-cycle terahertz pulses by optical rectification from a large aperture ZnTe crystal," *Opt. Express,* vol. 15, no. 20, pp. 13212-13220, 2007.

[23] J. Fülöp, L. Pálfalvi, G. Almási, and J. Hebling, "Design of high-energy terahertz sources based on optical rectification," *Optics express,* vol. 18, no. 12, pp. 12311-12327, 2010.

[24] C. Gollner *et al.*, "Highly efficient THz generation by optical rectification of mid-IR pulses in DAST," *APL Photonics,* vol. 6, no. 4, 2021.

[25] F. Junginger *et al.*, "Single-cycle multiterahertz transients with peak fields above 10 MV/cm," *Optics Letters,* vol. 35, no. 15, pp. 2645-2647, 2010.

[26] J. A. Fülöp, S. Tzortzakis, and T. Kampfrath, "Laser-driven strong-field terahertz sources," *Advanced Optical Materials,* vol. 8, no. 3, p. 1900681, 2020.

[27] R. W. Boyd and D. Prato, *Nonlinear Optics*. Elsevier Science, 2008.

[28] M. Bass, P. Franken, J. Ward, and G. Weinreich, "Optical rectification," *Physical Review Letters,* vol. 9, no. 11, p. 446, 1962.

[29] K. Yang, P. Richards, and Y. Shen, "Generation of far-infrared radiation by picosecond light pulses in LiNbO3," *Applied Physics Letters,* vol. 19, no. 9, pp. 320-323, 1971.

[30] D. H. Auston, K. Cheung, J. Valdmanis, and D. Kleinman, "Cherenkov radiation from femtosecond optical pulses in electro-optic media," *Physical Review Letters,* vol. 53, no. 16, p. 1555, 1984.

[31] F. Blanchard *et al.*, "Terahertz pulse generation from bulk GaAs by a tilted-pulse-front excitation at 1.8 µm," *Applied Physics Letters,* vol. 105, no. 24, 2014.

[32]   Gy. Polónyi *et al.*, "High-energy terahertz pulses from semiconductors pumped beyond the three-photon absorption edge," *Optics express,* vol. 24, no. 21, pp. 23872-23882, 2016.

[33]   J. A. Fülöp *et al.*, "Highly efficient scalable monolithic semiconductor terahertz pulse source," *Optica,* vol. 3, no. 10, pp. 1075-1078, 2016.

[34]   W. Cui, K. M. Awan, R. Huber, K. Dolgaleva, and J. M. Ménard, "Broadband and high-sensitivity time-resolved THz system using grating-assisted tilted-pulse-front phase matching," *Advanced Optical Materials,* vol. 10, no. 1, p. 2101136, 2022.

[35]   N. M. Mbithi *et al.*, "Investigation of terahertz pulse generation in semiconductors pumped at long infrared wavelengths," *JOSA B,* vol. 39, no. 10, pp. 2684-2691, 2022.

[36]   Z. Tibai, N. M. Mbithi, G. Almási, J. A. Fülöp, and J. Hebling, "Design of semiconductor contact grating terahertz source with enhanced diffraction efficiency," *Crystals,* vol. 12, no. 8, p. 1173, 2022.

[37]   Z. Tibai *et al.*, "Scalable microstructured semiconductor THz pulse sources," *Optics Express,* vol. 30, no. 25, pp. 45246-45258, 2022.

[38]   G. Tóth, G. Illés, G. Nazymbekov, N. Mbithi, G. Almási, and J. Hebling, "Possibility of CO2 laser-pumped multi-millijoule-level ultrafast pulse terahertz sources," *Scientific Reports,* vol. 14, no. 1, p. 999, 2024.

[39]   M. Hedegaard Kristensen, E. Herault, D. Zhai, E. Skovsen, and J.-L. Coutaz, "Terahertz generation through optical rectification in reflection," *Journal of Applied Physics,* vol. 133, no. 17, 2023.

[40]   M. Jazbinsek, U. Puc, A. Abina, and A. Zidansek, "Organic crystals for THz photonics," *Applied Sciences,* vol. 9, no. 5, p. 882, 2019.

[41]   S. J. Kim *et al.*, "Highly nonlinear optical organic crystals for efficient terahertz wave generation, detection, and applications," *Advanced Optical Materials,* vol. 9, no. 23, p. 2101019, 2021.

[42]   S. Mansourzadeh *et al.*, "Towards intense ultra-broadband high repetition rate terahertz sources based on organic crystals," *Optical Materials Express,* vol. 13, no. 11, pp. 3287-3308, 2023.

[43]   P. D. Cunningham and L. M. Hayden, "Optical properties of DAST in the THz range," *Optics express,* vol. 18, no. 23, pp. 23620-23625, 2010.

[44]   H. Uchida, H. Ochiai, K. Suizu, T. Shibuya, and K. Kawase, "Improving the laser-Induced-damage tolerance characteristics of 4-dimethylamino-N-methyl-4-stilbazoliumtosylate crystals for THz wave generation by annealing," *Japanese Journal of Applied Physics,* vol. 51, no. 2R, p. 022601, 2012.

[45]   C. P. Hauri, C. Ruchert, C. Vicario, and F. Ardana, "Strong-field single-cycle THz pulses generated in an organic crystal," *Applied Physics Letters,* vol. 99, no. 16, 2011.

[46]   C. Vicario *et al.*, "High efficiency THz generation in DSTMS, DAST and OH1 pumped by Cr: forsterite laser," *Optics express,* vol. 23, no. 4, pp. 4573-4580, 2015.

[47] C. Vicario, A. Ovchinnikov, S. Ashitkov, M. Agranat, V. Fortov, and C. Hauri, "Generation of 0.9-mJ THz pulses in DSTMS pumped by a Cr: Mg 2 SiO 4 laser," *Optics letters,* vol. 39, no. 23, pp. 6632-6635, 2014.

[48] C. Somma, G. Folpini, J. Gupta, K. Reimann, M. Woerner, and T. Elsaesser, "Ultra-broadband terahertz pulses generated in the organic crystal DSTMS," *Optics letters,* vol. 40, no. 14, pp. 3404-3407, 2015.

[49] T. O. Buchmann *et al.*, "High-power few-cycle THz generation at MHz repetition rates in an organic crystal," *APL Photonics,* vol. 5, no. 10, 2020.

[50] S. Mansourzadeh, T. Vogel, M. Shalaby, F. Wulf, and C. J. Saraceno, "Milliwatt average power, MHz-repetition rate, broadband THz generation in organic crystal BNA with diamond substrate," *Optics Express,* vol. 29, no. 24, pp. 38946-38957, 2021.

[51] S. Mansourzadeh, T. Vogel, A. Omar, M. Shalaby, M. Cinchetti, and C. J. Saraceno, "Broadband, high power THz source at 540 kHz using organic crystal BNA," *APL Photonics,* vol. 8, no. 1, 2023.

[52] G. Tóth, G. Polónyi, and J. Hebling, "Tilted pulse front pumping techniques for efficient terahertz pulse generation," *Light: Science & Applications,* vol. 12, no. 1, p. 256, 2023.

[53] J. Hebling, A. Stepanov, G. Almási, B. Bartal, and J. Kuhl, "Tunable THz pulse generation by optical rectification of ultrashort laser pulses with tilted pulse fronts," *Applied Physics B,* vol. 78, pp. 593-599, 2004.

[54] J. A. Fülöp *et al.*, "Efficient generation of THz pulses with 0.4 mJ energy," *Optics express,* vol. 22, no. 17, pp. 20155-20163, 2014.

[55] L. Pálfalvi *et al.*, "Nonlinear refraction and absorption of Mg doped stoichiometric and congruent LiNbO 3," *Journal of applied physics,* vol. 95, no. 3, pp. 902-908, 2004.

[56] O. Gayer, Z. Sacks, E. Galun, and A. Arie, "Temperature and wavelength dependent refractive index equations for MgO-doped congruent and stoichiometric LiNbO3," *Applied Physics B,* vol. 91, no. 2, pp. 343-348, 2008/05/01 2008, doi: 10.1007/s00340-008-2998-2.

[57] X. Wu, C. Zhou, W. R. Huang, F. Ahr, and F. X. Kärtner, "Temperature dependent refractive index and absorption coefficient of congruent lithium niobate crystals in the terahertz range," *Optics Express,* vol. 23, no. 23, pp. 29729-29737, 2015/11/16 2015, doi: 10.1364/OE.23.029729.

[58] J. Hebling, G. Almasi, I. Z. Kozma, and J. Kuhl, "Velocity matching by pulse front tilting for large-area THz-pulse generation," *Optics express,* vol. 10, no. 21, pp. 1161-1166, 2002.

[59] J. Hebling, K.-L. Yeh, M. C. Hoffmann, B. Bartal, and K. A. Nelson, "Generation of high-power terahertz pulses by tilted-pulse-front excitation and their application possibilities," *JOSA B,* vol. 25, no. 7, pp. B6-B19, 2008.

[60]   A. G. Stepanov, L. Bonacina, S. V. Chekalin, and J.-P. Wolf, "Generation of 30 µJ single-cycle terahertz pulses at 100 Hz repetition rate by optical rectification," *Optics letters,* vol. 33, no. 21, pp. 2497-2499, 2008.

[61]   L. Pálfalvi, J. Fülöp, G. Almási, and J. Hebling, "Novel setups for extremely high power single-cycle terahertz pulse generation by optical rectification," *Applied Physics Letters,* vol. 92, no. 17, 2008.

[62]   Z. Ollmann, J. Hebling, and G. Almási, "Design of a contact grating setup for mJ-energy THz pulse generation by optical rectification," *Applied Physics B,* vol. 108, pp. 821-826, 2012.

[63]   M. Tsubouchi, K. Nagashima, F. Yoshida, Y. Ochi, and M. Maruyama, "Contact grating device with Fabry–Perot resonator for effective terahertz light generation," *Optics Letters,* vol. 39, no. 18, pp. 5439-5442, 2014.

[64]   L. Pálfalvi, Z. Ollmann, L. Tokodi, and J. Hebling, "Hybrid tilted-pulse-front excitation scheme for efficient generation of high-energy terahertz pulses," *Optics express,* vol. 24, no. 8, pp. 8156-8169, 2016.

[65]   B. K. Ofori-Okai, P. Sivarajah, W. R. Huang, and K. A. Nelson, "THz generation using a reflective stair-step echelon," *Optics express,* vol. 24, no. 5, pp. 5057-5068, 2016.

[66]   L. Guiramand, J. Nkeck, X. Ropagnol, T. Ozaki, and F. Blanchard, "Near-optimal intense and powerful terahertz source by optical rectification in lithium niobate crystal," *Photonics Research,* vol. 10, no. 2, pp. 340-346, 2022.

[67]   Y. Avetisyan, A. Makaryan, V. Tadevosyan, and M. Tonouchi, "Design of a multistep phase mask for high-energy terahertz pulse generation by optical rectification," *Journal of Infrared, Millimeter, and Terahertz Waves,* vol. 38, pp. 1439-1447, 2017.

[68]   L. Pálfalvi *et al.*, "Numerical investigation of a scalable setup for efficient terahertz generation using a segmented tilted-pulse-front excitation," *Optics express,* vol. 25, no. 24, pp. 29560-29573, 2017.

[69]   P. S. Nugraha *et al.*, "Demonstration of a tilted-pulse-front pumped plane-parallel slab terahertz source," *Optics letters,* vol. 44, no. 4, pp. 1023-1026, 2019.

[70]   G. Tóth *et al.*, "Numerical investigation of imaging-free terahertz generation setup using segmented tilted-pulse-front excitation," *Optics express,* vol. 27, no. 5, pp. 7762-7775, 2019.

[71]   G. Illés *et al.*, "Terahertz generation by imaging-free nonlinear echelon slab," in *High Intensity Lasers and High Field Phenomena*, 2022: Optica Publishing Group, p. JW5A. 13.

[72]   L. Wang, G. Tóth, J. Hebling, and F. Kärtner, "Tilted-pulse-front schemes for terahertz generation," *Laser & Photonics Reviews,* vol. 14, no. 7, p. 2000021, 2020.

[73]   G. Krizsán *et al.*, "Demonstration of an imaging-free terahertz generation setup using segmented tilted-pulse-front excitation," *Optics letters,* vol. 48, no. 14, pp. 3777-3780, 2023.

[74]   G. Tóth *et al.*, "Single-cycle scalable terahertz pulse source in reflection geometry," *Optics express,* vol. 27, no. 21, pp. 30681-30691, 2019.

[75]   B. Zhang *et al.*, "1.4-mJ high energy terahertz radiation from lithium niobates," *Laser & Photonics Reviews,* vol. 15, no. 3, p. 2000295, 2021.

[76]   Q. Tian *et al.*, "Efficient generation of a high-field terahertz pulse train in bulk lithium niobate crystals by optical rectification," *Optics Express,* vol. 29, no. 6, pp. 9624-9634, 2021.

[77]   G. Krizsán *et al.*, "Uniformly scalable lithium niobate THz pulse source in transmission geometry," *Optics Express,* vol. 30, no. 3, pp. 4434-4443, 2022.

[78]   X. Wu *et al.*, "Generation of 13.9-mJ terahertz radiation from lithium niobate materials," *Advanced Materials,* vol. 35, no. 23, p. 2208947, 2023.

[79]   K. S. Youngworth and T. G. Brown, "Focusing of high numerical aperture cylindrical-vector beams," *Optics Express,* vol. 7, no. 2, pp. 77-87, 2000.

[80]   H. Dehez, A. April, and M. Piché, "Needles of longitudinally polarized light: guidelines for minimum spot size and tunable axial extent," *Optics Express,* vol. 20, no. 14, pp. 14891-14905, 2012.

[81]   R. Dorn, S. Quabis, and G. Leuchs, "Sharper focus for a radially polarized light beam," *Physical review letters,* vol. 91, no. 23, p. 233901, 2003.

[82]   V. Marceau, C. Varin, and M. Piché, "Validity of the paraxial approximation for electron acceleration with radially polarized laser beams," *Optics letters,* vol. 38, no. 6, pp. 821-823, 2013.

[83]   X. Hao, C. Kuang, T. Wang, and X. Liu, "Phase encoding for sharper focus of the azimuthally polarized beam," *Optics letters,* vol. 35, no. 23, pp. 3928-3930, 2010.

[84]   S. Hell and E. H. Stelzer, "Properties of a 4Pi confocal fluorescence microscope," *JOSA A,* vol. 9, no. 12, pp. 2159-2166, 1992.

[85]   S. W. Hell, S. Lindek, C. Cremer, and E. H. Stelzer, "Measurement of the 4Pi-confocal point spread function proves 75 nm axial resolution," *Applied Physics Letters,* vol. 64, no. 11, pp. 1335-1337, 1994.

[86]   N. Bokor and N. Davidson, "4π focusing with single paraboloid mirror," *Optics communications,* vol. 281, no. 22, pp. 5499-5503, 2008.

[87]   A. April and M. Piché, "4π Focusing of TM 01 beams under nonparaxial conditions," *Optics express,* vol. 18, no. 21, pp. 22128-22140, 2010.

[88]   C. Debus, M. Lieb, A. Drechsler, and A. Meixner, "Probing highly confined optical fields in the focal region of a high NA parabolic mirror with subwavelength spatial resolution," *Journal of microscopy,* vol. 210, no. 3, pp. 203-208, 2003.

[89]   N. Bokor and N. Davidson, "Toward a spherical spot distribution with 4π focusing of radially polarized light," *Optics letters,* vol. 29, no. 17, pp. 1968-1970, 2004.

[90]   W. Chen and Q. Zhan, "Creating a spherical focal spot with spatially modulated radial polarization in 4Pi microscopy," *Optics letters,* vol. 34, no. 16, pp. 2444-2446, 2009.

[91] Z. Chen and D. Zhao, "4Pi focusing of spatially modulated radially polarized vortex beams," *Optics Letters,* vol. 37, no. 8, pp. 1286-1288, 2012.

[92] S. Yan, B. Yao, W. Zhao, and M. Lei, "Generation of multiple spherical spots with a radially polarized beam in a 4π focusing system," *JOSA A,* vol. 27, no. 9, pp. 2033-2037, 2010.

[93] S. Yan, B. Yao, and R. Rupp, "Shifting the spherical focus of a 4Pi focusing system," *Optics Express,* vol. 19, no. 2, pp. 673-678, 2011.

[94] N. Bokor and N. Davidson, "Generation of a hollow dark spherical spot by 4pi focusing of a radially polarized Laguerre-Gaussian beam," *Optics letters,* vol. 31, no. 2, pp. 149-151, 2006.

[95] N. Davidson and N. Bokor, "High-numerical-aperture focusing of radially polarized doughnut beams with a parabolic mirror and a flat diffractive lens," *Optics Letters,* vol. 29, no. 12, pp. 1318-1320, 2004.

[96] J. Stadler, C. Stanciu, C. Stupperich, and A. Meixner, "Tighter focusing with a parabolic mirror," *Optics letters,* vol. 33, no. 7, pp. 681-683, 2008.

[97] V. Ignatovsky, "The relationship between geometric and wave optics and diffraction of an azimuthally symmetric beam," *Trans. Opt. Inst. Petrograd,* vol. 1, p. 3, 1920.

[98] V. Ignatovsky, "Diffraction by a parabolic mirror having arbitrary opening," *Trans. Opt. Inst. Petrograd,* vol. 1, no. 5, 1920.

[99] B. Richards and E. Wolf, "Electromagnetic diffraction in optical systems, II. Structure of the image field in an aplanatic system," *Proceedings of the Royal Society of London. Series A. Mathematical and Physical Sciences,* vol. 253, no. 1274, pp. 358-379, 1959.

[100] N. Lindlein, R. Maiwald, H. Konermann, M. Sondermann, U. Peschel, and G. Leuchs, "A new 4π geometry optimized for focusing on an atom with a dipole-like radiation pattern," *Laser Physics,* vol. 17, pp. 927-934, 2007.

[101] N. Lindlein, M. Sondermann, R. Maiwald, H. Konermann, U. Peschel, and G. Leuchs, "Focusing light with a deep parabolic mirror," *arXiv preprint arXiv:1905.05997,* 2019.

[102] J. A. Stratton and L. Chu, "Diffraction theory of electromagnetic waves," *Physical Review,* vol. 56, no. 1, p. 99, 1939.

[103] P. Varga and P. Török, "Focusing of electromagnetic waves by paraboloid mirrors. I. Theory," *JOSA A,* vol. 17, no. 11, pp. 2081-2089, 2000.

[104] P. Varga and P. Török, "Focusing of electromagnetic waves by paraboloid mirrors. II. Numerical results," *JOSA A,* vol. 17, no. 11, pp. 2090-2095, 2000.

[105] H. Zhang *et al.*, "Parabolic Mirror Focusing of Spatiotemporally Coupled Ultrashort Terahertz Pulses," *IEEE Photonics Journal,* 2023.

[106] T. M. Jeong, S. Weber, B. Le Garrec, D. Margarone, T. Mocek, and G. Korn, "Spatio-temporal modification of femtosecond focal spot under tight focusing condition," *Optics Express,* vol. 23, no. 9, pp. 11641-11656, 2015.

[107] J. Dumont, F. Fillion-Gourdeau, C. Lefebvre, D. Gagnon, and S. MacLean, "Efficiently parallelized modeling of tightly focused, large bandwidth laser pulses," *Journal of Optics,* vol. 19, no. 2, p. 025604, 2017.

[108] X. Zeng and X. Chen, "Characterization of tightly focused vector fields formed by off-axis parabolic mirror," *Optics Express,* vol. 27, no. 2, pp. 1179-1198, 2019.

[109] X. Zeng, "Configuration optimization of off-axis parabolic mirror for enhancing the focusability of a laser beam," *Chinese Optics Letters,* vol. 19, no. 3, p. 032601, 2021.

[110] H. Chen, S. Tripathi, and K. C. Toussaint, "Demonstration of flat-top focusing under radial polarization illumination," *Optics letters,* vol. 39, no. 4, pp. 834-837, 2014.

[111] Z. T. Godana, J. Hebling, and L. Pálfalvi, "Focusing of Radially Polarized Electromagnetic Waves by a Parabolic Mirror," in *Photonics*, 2023, vol. 10, no. 7: MDPI, p. 848.

[112] J. Lin, Y. Ma, P. Jin, G. Davies, and J. Tan, "Longitudinal polarized focusing of radially polarized sinh-Gaussian beam," *Optics Express,* vol. 21, no. 11, pp. 13193-13198, 2013.

[113] G. Endale, D. Mohan, and S. Yadav, "Focusing of radially polarized bessel gaussian and hollow gaussian beam of high NA to achieve super resolution," *Optik,* vol. 253, p. 168586, 2022.

[114] K. T. McDonald, "Axicon Gaussian Laser Beams," p. physics/0003056doi: 10.48550/arXiv.physics/0003056.

[115] S. Payeur *et al.*, "Generation of a beam of fast electrons by tightly focusing a radially polarized ultrashort laser pulse," *Applied Physics Letters,* vol. 101, no. 4, 2012.

[116] L. J. Wong and F. X. Kärtner, "Direct acceleration of an electron in infinite vacuum by a pulsed radially-polarized laser beam," *Optics express,* vol. 18, no. 24, pp. 25035-25051, 2010.

[117] H. Wang, L. Shi, B. Lukyanchuk, C. Sheppard, and C. T. Chong, "Creation of a needle of longitudinally polarized light in vacuum using binary optics," *Nature photonics,* vol. 2, no. 8, pp. 501-505, 2008.

[118] M. Meier, V. Romano, and T. Feurer, "Material processing with pulsed radially and azimuthally polarized laser radiation," *Applied Physics A,* vol. 86, pp. 329-334, 2007.

[119] S. Skelton, M. Sergides, R. Saija, M. Iatì, O. Maragó, and P. Jones, "Trapping volume control in optical tweezers using cylindrical vector beams," *Optics letters,* vol. 38, no. 1, pp. 28-30, 2013.

[120] D. P. Biss, K. S. Youngworth, and T. G. Brown, "Dark-field imaging with cylindrical-vector beams," *Applied optics,* vol. 45, no. 3, pp. 470-479, 2006.

[121] G. Chang, C. J. Divin, C.-H. Liu, S. L. Williamson, A. Galvanauskas, and T. B. Norris, "Generation of radially polarized terahertz pulses via velocity-mismatched optical rectification," *Optics letters,* vol. 32, no. 4, pp. 433-435, 2007.

[122] R. Imai, N. Kanda, T. Higuchi, Z. Zheng, K. Konishi, and M. Kuwata-Gonokami, "Terahertz vector beam generation using segmented nonlinear optical crystals with threefold rotational symmetry," *Optics Express,* vol. 20, no. 20, pp. 21896-21904, 2012.

[123] M. J. Cliffe, D. M. Graham, and S. Jamison, "Longitudinally polarized single-cycle terahertz pulses generated with high electric field strengths," *Applied Physics Letters,* vol. 108, no. 22, 2016.

[124] Y. Minami, T. Kurihara, K. Yamaguchi, M. Nakajima, and T. Suemoto, "Longitudinal terahertz wave generation from an air plasma filament induced by a femtosecond laser," *Applied Physics Letters,* vol. 102, no. 15, 2013.

[125] K. Kan *et al.*, "Radially polarized terahertz waves from a photoconductive antenna with microstructures," *Applied Physics Letters,* vol. 102, no. 22, 2013.

[126] M. J. Cliffe, A. Rodak, D. M. Graham, and S. P. Jamison, "Generation of longitudinally polarized terahertz pulses with field amplitudes exceeding 2 kV/cm," *Applied Physics Letters,* vol. 105, no. 19, 2014.

[127] H. Hirori, F. Blanchard, and K. Tanaka, "Single-cycle terahertz pulses with amplitudes exceeding 1 MV/cm generated by optical rectification in LiNbO3," *Applied Physics Letters,* vol. 98, no. 9, 2011.

[128] A. Woldegeorgis *et al.*, "Multi-MV/cm longitudinally polarized terahertz pulses from laser–thin foil interaction," *Optica,* vol. 5, no. 11, pp. 1474-1477, 2018.

[129] M. Hibberd, D. Lake, N. Johansson, T. Thomson, S. Jamison, and D. Graham, "Magnetic-field tailoring of the terahertz polarization emitted from a spintronic source," *Applied Physics Letters,* vol. 114, no. 3, 2019.

[130] C. Bull *et al.*, "Spintronic terahertz emitters: Status and prospects from a materials perspective," *Apl Materials,* vol. 9, no. 9, 2021.

[131] S. Carbajo *et al.*, "Direct longitudinal laser acceleration of electrons in free space," *Physical Review Accelerators and Beams,* vol. 19, no. 2, p. 021303, 2016.

[132] L. J. Wong *et al.*, "Laser-induced linear-field particle acceleration in free space," *Scientific reports,* vol. 7, no. 1, p. 11159, 2017.

[133] K. Popov, V. Y. Bychenkov, W. Rozmus, and R. Sydora, "Electron vacuum acceleration by a tightly focused laser pulse," *Physics of Plasmas,* vol. 15, no. 1, 2008.

[134] S. Bochkarev, K. Popov, and V. Y. Bychenkov, "Vacuum electron acceleration by a tightly focused, radially polarized, relativistically strong laser pulse," *Plasma physics reports,* vol. 37, pp. 603-614, 2011.

[135] C. Varin *et al.*, "Direct electron acceleration with radially polarized laser beams," *Applied Sciences,* vol. 3, no. 1, pp. 70-93, 2013.

[136] S. W. Jolly, "On the importance of frequency-dependent beam parameters for vacuum acceleration with few-cycle radially polarized laser beams," *Optics Letters,* vol. 45, no. 14, pp. 3865-3868, 2020.

[137] J. A. Fülöp, L. Pálfalvi, M. C. Hoffmann, and J. Hebling, "Towards generation of mJ-level ultrashort THz pulses by optical rectification," *Optics express,* vol. 19, no. 16, pp. 15090-15097, 2011.

[138] L. J. Wong, A. Fallahi, and F. X. Kärtner, "Compact electron acceleration and bunch compression in THz waveguides," *Optics express,* vol. 21, no. 8, pp. 9792-9806, 2013.

[139] J. Hebling, J. Fülöp, M. Mechler, L. Pálfalvi, C. Tőke, and G. Almási, "Optical manipulation of relativistic electron beams using THz pulses," *arXiv preprint arXiv:1109.6852,* 2011.

[140] L. Pálfalvi, J. A. Fülöp, G. Tóth, and J. Hebling, "Evanescent-wave proton postaccelerator driven by intense THz pulse," *Physical Review Special Topics-Accelerators and Beams,* vol. 17, no. 3, p. 031301, 2014.

[141] Z. Tibai, S. Turnár, G. Tóth, J. Hebling, and S. W. Jolly, "Spatiotemporal modeling of direct acceleration with high-field terahertz pulses," *Optics express,* vol. 30, no. 18, pp. 32861-32870, 2022.

[142] S. Turnár, G. Krizsán, J. Hebling, and Z. Tibai, "Waveguide structure based electron acceleration using terahertz pulses," *Optics Express,* vol. 30, no. 15, pp. 27602-27608, 2022.

[143] E. A. Nanni *et al.*, "Linear electron acceleration in THz waveguides," in *IPAC2014: 5th International Particle Accelerator Conference*, 2014: Joint Accelerator Conferences Website JACoW, pp. 1896-1899.

[144] W. R. Huang *et al.*, "Toward a terahertz-driven electron gun," *Scientific reports,* vol. 5, no. 1, p. 14899, 2015.

[145] A. Sharma, Z. Tibai, and J. Hebling, "Intense tera-hertz laser driven proton acceleration in plasmas," *Physics of Plasmas,* vol. 23, no. 6, 2016.

[146] Z. Tibai *et al.*, "Relativistic electron acceleration by focused THz pulses," *Journal of Physics B: Atomic, Molecular and Optical Physics,* vol. 51, no. 13, p. 134004, 2018.

[147] S. Turnár, B. Sarkadi, S. Jolly, J. Hebling, and Z. Tibai, "Numerical investigation of terahertz wave driven electron acceleration generated from gas jet," *Applied Physics B,* vol. 130, no. 2, pp. 1-8, 2024.

[148] D. Zhang *et al.*, "Segmented terahertz electron accelerator and manipulator (STEAM)," *Nature photonics,* vol. 12, no. 6, pp. 336-342, 2018.

[149] D. Zhang *et al.*, "Femtosecond phase control in high-field terahertz-driven ultrafast electron sources," *Optica,* vol. 6, no. 7, pp. 872-877, 2019.

[150] M. T. Hibberd *et al.*, "Acceleration of relativistic beams using laser-generated terahertz pulses," *Nature Photonics,* vol. 14, no. 12, pp. 755-759, 2020.

[151] S. Turnár, J. Hebling, J. Fülöp, G. Tóth, G. Almási, and Z. Tibai, "Design of a THz-driven compact relativistic electron source," *Applied Physics B,* vol. 127, pp. 1-7, 2021.

[152] X. Yu, Y. Zeng, Y. Bai, L. Song, and Y. Tian, "Hollow metal tubes for efficient electron manipulation using terahertz surface waves," *Optics Express,* vol. 32, no. 3, pp. 3076-3084, 2024.

[153] S. Mezouari and A. R. Harvey, "Validity of Fresnel and Fraunhofer approximations in scalar diffraction," *Journal of Optics A: Pure and Applied Optics,* vol. 5, no. 4, p. S86, 2003.

[154] K. G. Lee *et al.*, "Vector field microscopic imaging of light," *Nature Photonics,* vol. 1, no. 1, pp. 53-56, 2007.

[155] J. W. Goodman, *Introduction to Fourier optics*. Roberts and Company publishers, 2005.

[156] K. Zhang, D. Li, K. Chang, K. Zhang, and D. Li, *Electromagnetic theory for microwaves and optoelectronics*. Springer, 1998.

[157] P. Török, P. R. Munro, and E. E. Kriezis, "Rigorous near-to far-field transformation for vectorial diffraction calculations and its numerical implementation," *JOSA A,* vol. 23, no. 3, pp. 713-722, 2006.

[158] J. Braat and P. Török, *Imaging optics*. Cambridge university press, 2019.

[159] K. Shimoda, "Vectorial analysis of the Gaussian beams of light," *Journal of the Physical Society of Japan,* vol. 60, no. 1, pp. 141-145, 1991.

[160] L. Pálfalvi, Z. T. Godana, and J. Hebling, "Electromagnetic Field Distribution and Divergence-Dependence of a Radially Polarized Gaussian Vector Beam Focused by a Parabolic Mirror," *arXiv preprint arXiv:2406.00795,* 2024.

[161] T. Phan *et al.*, "High-efficiency, large-area, topology-optimized metasurfaces," *Light: Science & Applications,* vol. 8, no. 1, p. 48, 2019.

[162] J. Grand and E. C. Le Ru, "Practical implementation of accurate finite-element calculations for electromagnetic scattering by nanoparticles," *Plasmonics,* vol. 15, no. 1, pp. 109-121, 2020.

[163] H. Guerboukha *et al.*, "Efficient leaky-wave antennas at terahertz frequencies generating highly directional beams," *Applied Physics Letters,* vol. 117, no. 26, 2020.

[164] E. A. Nanni *et al.*, "Terahertz-driven linear electron acceleration," *Nature communications,* vol. 6, no. 1, p. 8486, 2015.

[165] S. W. Jolly, "Modeling the focusing of a radially polarized laser beam with an initially flat-top intensity profile," *J. Opt. Soc. Am. A,* vol. 41, no. 7, pp. 1390-1396, 2024/07/01 2024, doi: 10.1364/JOSAA.528336.

[166] B. E. A. Saleh and M. C. Teich, *Fundamentals of Photonics*. Wiley, 2019.

[167] B. D. Guenther, *Modern Optics*. Oxford University Press, 2015.

[168] L. Pálfalvi, Z. T. Godana, G. Tóth, and J. Hebling, "Generation of extremely strong accelerating electric field by focusing radially polarized THz pulses with a paraboloid ring," *Optics & Laser Technology,* vol. 180, p. 111554, 2025.

[169] I. M. Bassett, "Limit to concentration by focusing," *Optica Acta: International Journal of Optics,* vol. 33, no. 3, pp. 279-286, 1986.

[170] C. Lombosi, G. Polónyi, M. Mechler, Z. Ollmann, J. Hebling, and J. A. Fülöp, "Nonlinear distortion of intense THz beams," *New Journal of Physics,* vol. 17, no. 8, p. 083041, 2015.

[171] M. Couture and M. Piche, "Focusing properties of an axicon pair," *Canadian journal of physics,* vol. 71, no. 1-2, pp. 70-78, 1993.

[172] S. R. Mishra, S. K. Tiwari, S. P. Ram, and S. C. Mehendale, "Generation of hollow conic beams using a metal axicon mirror," *Optical Engineering,* vol. 46, no. 8, pp. 084002-084002-5, 2007.

[173] A. I. Hernandez-Serrano and E. Pickwell-MacPherson, "Low cost and long-focal-depth metallic axicon for terahertz frequencies based on parallel-plate-waveguides," *Scientific reports,* vol. 11, no. 1, p. 3005, 2021.

[174] M. Bashirpour, W. Cui, A. Gamouras, and J.-M. Ménard, "Scalable fabrication of nanogratings on GaP for efficient diffraction of near-infrared pulses and enhanced terahertz generation by optical rectification," *Crystals,* vol. 12, no. 5, p. 684, 2022.

[175] K. Wynne and J. J. Carey, "An integrated description of terahertz generation through optical rectification, charge transfer, and current surge," *Optics Communications,* vol. 256, no. 4-6, pp. 400-413, 2005.

[176] A. Kaplan, "Diffraction-induced transformation of near-cycle and subcycle pulses," *JOSA B,* vol. 15, no. 3, pp. 951-956, 1998.